Ligand Influence on Nanoparticle Agglomeration in Flow

Dissertation
zur Erlangung des Grades
des Doktors der Naturwissenschaften
der Naturwissenschaftlich-Technischen Fakultät III
Chemie, Pharmazie, Bio- und Werkstoffwissenschaften
der Universität des Saarlandes

Dominik Gerstner
INM – Leibniz-Institut für Neue Materialien gGmbH
Universität des Saarlandes

Saarbrücken, April 2016

Tag des Kolloquiums:	6. September 2016
Dekan:	Prof. Dr.-Ing. Dirk Bähre
Berichterstatter:	Prof. Dr. Eduard Arzt
	Prof. Dr. Guido Kickelbick
Vorsitz:	Prof. Dr. David Scheschkewitz
Akad. Mitarbeiter:	Dr. Tobias Kraus

Acknowledgements

I would like to express my gratitude to Prof. Eduard Arzt for supervising me during my time as PhD student at the INM and reviewing my dissertation and for giving me the opportunity to work at his renowned institute. Further gratitude belongs to Prof. Guido Kickelbick for reviewing my dissertation and becoming the second referee.

I would like to thank Dr. Tobias Kraus, head of the “Structure Formation” group, for his excellent guidance during my time as a PhD student at the INM. He succeeded in creating a fruitful and friendly working atmosphere. Especially his open door for all questions and problems appearing during a research project were a great help. Without his honest guidance, this research would not have been finalised.

All people who contributed to this work deserve an acknowledgement here. Thank you to Anika Kleemann for countless syntheses and the help in searching for the proper method. All colleagues who burned the candle at both ends during the synchrotron visits, Dr. Johann Lacava, Jonas Becker, Aljosha-Rakim Jochem, Thomas Kister, Dr. Tobias Kraus, Johannes Maurer and Sebastian Beck share my deep appreciation. The rest of the NanoSpekt team, Beate Reiser, Dr. Lola González-García and Dr. Ioannis Kanelidis, deserves my gratitude for all help, especially with the nanowire chapter. I wish to thank Dr. Bernd Morgenstern and again Aljosha-Rakim Jochem for the help with titration.

I would like to thank the remaining people from the structure formation group, Philip Born, Daniel Brodoceanu, Jona Engel, Thilo Grammes, Jonas Hubertus, Indra Backes, Lars-Arne Meyer, Genesis Ngwa Ankah, Peng Zhang and last but not least Andreas Hegetschweiler for the great time. All other colleagues from the INM who helped during my time share my appreciation.

Parts of this research were carried out at the light source PETRA III at DESY, a member of the Helmholtz Association (HGF). I would like to thank S.V. Roth and S. Yu for assistance in using beamline MiNaXS. The synchrotron SOLEIL is acknowledged for supplying the SAXS beam time. I wish to thank Dr. Javier Pérez and his team from the SWING beamline for their support.

Naturally, it was only the continuing support of my friends and family that made this work possible, you share my appreciation. Special thanks go to my dear friend Christian Schedler for proofreading the text. Words can not describe the gratitude I owe to my wife Nina Gerstner, for offering open arms at all times and organising our life during the busier parts, thank you.

Statement on Contributions

The ideas for the project were largely developed in a collaboration between his supervisor Dr. Tobias Kraus and the author. The experimental data presented here was largely acquired in a collaborative effort. The particular contributions are clarified in the following.

Syntheses

The particles employed for the experiments in chapter 2 were synthesised by colleagues. Anika Kleemann prepared batches 1 to 7, Aljosha-Rakim Jochem provided batch 8 to 10 and dynamic light scattering measurements for quality control.

The “Zheng” particles used in chapter 3 were prepared by Anika Weber. Thomas Kister synthesised the “Wu” particles, mainly employed in chapter 3.

The syntheses of the nanowires used in chapter 4 were performed by Dr. Ioannis Kanelidis assisted by Dr. Lola González-García, Beate Reiser and Johannes Maurer.

Experiments

The experiments in chapter 2 were performed at the MiNaXS beamline of the synchrotron PETRA III. The beamline staff, especially Dr. Shun Yu, helped in establishing the proper beamline settings. The experiments were devised by the author. Dr. Tobias Kraus, Aljosha-Rakim Jochem and Thomas Kister helped to perform the experiments during the 72 h of continuous operation.

The data presented in chapter 3 was acquired during a beamtime at the SWING beamline of the synchrotron SOLEIL. Dr. Javier Pérez, the principal beamline scientist, helped to set up the beamline for the experiments. The experimental schedule was devised by the author. Dr. Tobias Kraus, Johannes Maurer and Sebastian Beck helped to continuously operate the experiments for 72 h.

The experiments in chapter 4 were solely performed by the author. The ideas for the project were developed mainly in discussions with Dr. Lola González-García and Beate Reiser.

Authorship

The author analysed the raw data and drew the figures presented in this research using only the cited references. The dissertation itself was conceived and written by the author. Publications on the results presented in chapter 3 and chapter 4 are in preparation at the time of writing. Above that, the dissertation contains no material previously published elsewhere unless stated otherwise.

Abstract

Having emerged from basic science, nanoparticles are now applied in many fields of science and technology. Agglomeration is ubiquitous and occurs, often inadvertently, in the formulation of particle-polymer mixtures, during the chemical functionalisation of nanoparticles and even during storage.

This dissertation outlines recent studies on the agglomeration behaviour of different gold nanoparticle types. A modular fluidic system was specifically designed to perform the experiments. It enables the preparation of a steady flow of stable or unstable nanoparticle samples. This allows to observe different steps of a time-dependant process in steady state over practically arbitrary times in flow.

These capabilities are used in this research to investigate the agglomeration of destabilised aqueous gold nanoparticles, reassess the solvent induced self-assembly of unpolar gold nanoparticles and examine the shear-assisted orientation of gold nanowires. The performance of the system is demonstrated and new insights on the influence of solvent conditions, temperature and the flow field are presented. The relevant process parameters as well as the microscopic interactions responsible for the structure formation mechanisms are discussed.

Zusammenfassung

Nanopartikel sind ihren Kinderschuhen in der Grundlagenforschung entwachsen und haben mittlerweile vielfältige Einsatzmöglichkeiten von der Forschung bis zur industriellen Anwendung. Agglomeration spielt in der Regel eine Rolle und tritt (gewollt oder ungewollt) bei der Herstellung von Partikel-Polymerkompositen, der Oberflächenmodifizierung von Partikeln und selbst der Lagerung auf.

In dieser Dissertation werden neue Studien zur Agglomeration verschiedener Klassen von Gold-Nanopartikeln vorgestellt. Ein modulares Fluidiksystem wurde speziell für die hier präsentierten Versuche entworfen. Damit kann ein kontinuierlicher Fluss aus stabilen und speziell auch destabilisierten Nanopartikelproben erzeugt werden. Dadurch wird es möglich, verschiedene Stufen einer zeitlich veränderlichen Reaktion im Fließgleichgewicht zu analysieren. Dabei ist die Integrationszeit grundsätzlich nicht beschränkt.

Mittels dieser Möglichkeiten wurde in dieser Forschungsarbeit die Agglomeration von destabilisierten, wässrigen Gold-Nanopartikeln untersucht, die Selbstorganisation unpolarer Partikel in geordnete Überstrukturen neu beleuchtet und die Ausrichtung von Gold-Nanodrähten in einer Scherströmung analysiert. Die dazugehörigen Prozessparameter sowie die zugrunde liegenden mikroskopischen Wechselwirkung sollen in dieser Arbeit erörtert werden.

Contents

Acknowledgements i

Abstract iii

Zusammenfassung v

1. Preliminary 1
- 1.1. Introduction 1
  - 1.1.1. Definitions 4
- 1.2. Nanoparticle Agglomeration 6
  - 1.2.1. Nanoparticles 6
  - 1.2.2. Interactions 8
    - 1.2.2.1. Van der Waals Interactions 8
    - 1.2.2.2. Electrostatic Interactions 9
    - 1.2.2.3. Steric Interactions 10
    - 1.2.2.4. Generic Shape of the Interaction Potential 12
  - 1.2.3. Nanoparticle Agglomeration: State of the Art 13
    - 1.2.3.1. Charge-Stabilised Systems 13
    - 1.2.3.2. Sterically Stabilised Systems 16
    - 1.2.3.3. Directly Related Studies 17
    - 1.2.3.4. Flow-Based Studies 19
- 1.3. Measurement Techniques 20
  - 1.3.1. UV/Vis Spectroscopy 20
  - 1.3.2. Small-Angle X-ray Scattering 24
    - 1.3.2.1. Sample Preparation and Data Collection 27
    - 1.3.2.2. Data Corrections 28
    - 1.3.2.3. Data Analysis 29
  - 1.3.3. Agglomeration Studies in a Flow System 31
    - 1.3.3.1. Static Micromixer 33
    - 1.3.3.2. Different Distributions 37
    - 1.3.3.3. Fouling 39

2. Agglomeration of Aqueous Gold Nanoparticles 41
- 2.1. Introduction 41

- 2.2. Methods 42
  - 2.2.1. Particles 43
  - 2.2.2. SAXS 44
    - 2.2.2.1. Instrumentation 44
    - 2.2.2.2. Data Evaluation 44
  - 2.2.3. UV/Vis 45
  - 2.2.4. Gradient Measurements 48
  - 2.2.5. Agglomerate Age 51
  - 2.2.6. Cleaning Procedure 52
- 2.3. Single Particles 53
  - 2.3.1. Results 53
  - 2.3.2. Discussion 55
- 2.4. Agglomeration Experiments 55
  - 2.4.1. Results 55
    - 2.4.1.1. Fouling Issues 57
  - 2.4.2. Discussion 59
- 2.5. Solvent Variation 61
  - 2.5.1. Results 61
  - 2.5.2. Discussion 63
- 2.6. Velocity Variation 64
  - 2.6.1. Results 65
  - 2.6.2. Discussion 66
- 2.7. Particle Variation 67
  - 2.7.1. Results 67
  - 2.7.2. Discussion 69
- 2.8. Summary and Conclusions 70

3. Agglomeration of Unpolar Gold Nanoparticles 73
- 3.1. Introduction 73
- 3.2. Methods 74
  - 3.2.1. Particles 75
  - 3.2.2. Experimental Setup 76
  - 3.2.3. Agglomeration Experiments 77
  - 3.2.4. SAXS 78
    - 3.2.4.1. Instrumentation 78
    - 3.2.4.2. Data Evaluation 78
- 3.3. Primary Particles 81
  - 3.3.1. Results 82
    - 3.3.1.1. Wall Fouling 82
    - 3.3.1.2. Comparison 83
  - 3.3.2. Discussion 86

3.4. Solvent Variation . . . 87
  3.4.1. Results . . . 87
  3.4.2. Discussion . . . 93
3.5. Temperature Variation . . . 98
  3.5.1. Results . . . 98
    3.5.1.1. Dodecanethiol . . . 98
    3.5.1.2. Hexadecanethiol . . . 100
    3.5.1.3. Octadecanethiol . . . 103
  3.5.2. Discussion . . . 104
3.6. Early Stages of Agglomeration . . . 108
  3.6.1. Results . . . 109
  3.6.2. Discussion . . . 111
3.7. Summary and Conclusions . . . 112

4. Agglomeration and Alignment of Unpolar Gold Nanowires 115
4.1. Introduction . . . 115
4.2. Methods . . . 116
  4.2.1. SAXS . . . 116
  4.2.2. Gold Nanowires . . . 118
4.3. Nanowire Bundling . . . 119
  4.3.1. Results . . . 119
    4.3.1.1. Primary Nanowires . . . 119
    4.3.1.2. Bundled Nanowires . . . 121
  4.3.2. Discussion . . . 123
4.4. Flow Influence . . . 127
  4.4.1. Results . . . 127
  4.4.2. Discussion . . . 129
4.5. Conclusions . . . 131

5. Conclusion 133
5.1. Conclusion . . . 133
5.2. Outlook . . . 135

Bibliography 137

A. Determination of Particle Size I

B. Additional Results for Unpolar Agglomeration III
B.1. Agglomeration Induced by Ethanol . . . III
B.2. Agglomeration of Wu 2 Particles . . . IV

List of Abbreviations

1D One-Dimensional.

2D Two-Dimensional.

3D Three-Dimensional.

a.u. Arbitrary Units.

AuNP Gold Nanoparticle.

AuNW Gold Nanowire.

C12 1-Dodecanethiol.

C16 1-Hexadecanethiol.

C18 1-Octadecanethiol.

ccc Critical Coagulation Concentration.

CCD Charge-Coupled Device.

cps Counts per Second.

DESY Deutsches Elektronen-Synchrotron.

DLA Diffusion-Limited Agglomeration.

ESRF European Synchrotron Radiation Facility.

fcc Face Centred Cubic.

FEP Fluorinated Ethylene Propylene.

FWHM Full Width at Half Maximum.

HPLC High Performance Liquid Chromatography.

HWHM Half Width at Half Maximum. 2·HWHM=FWHM.

LSPR Localized Surface Plasmon Resonance.

LURE Laboratoire pour l'Utilisation du Rayonnement Électromagnétique.

MUTEG (1-Mercaptoundec-11-yl)tetra(ethylene glycol) ($C_{19}H_{40}O_5S$).

NP Nanoparticle.

NPs Nanoparticles.

OAm Oleylamine.

PEG Polyethylene glycol (here: $C_{44}H_{89}N\ O_{21}S$).

PIN-diode Positive Intrinsic Negative-Diode.

RLA Reaction-Limited Agglomeration.

SAXS Small-Angle X-ray Scattering.

SOLEIL Source Optimisée de Lumière d'Énergie Intermédiaire du LURE.

TBAB Borane *tert*-Butylamine Complex, $(CH_3)_3CNH_2{\cdot}BH_3$.

TEM Transmission Electron Microscopy.

TEM Transmission Electron Microscope.

UV/Vis Ultraviolet-Visible.

List of Symbols

(hk) 2D Miller Indices.

(hkl) 3D Miller Indices.

2Θ Scattering Angle.

$A(\boldsymbol{q})$ Scattering Amplitude.

$A\,(\lambda)$ Absorbance.

D_{r} Rotational Diffusion Constant.

D_{t} Translational Diffusion Constant.

$I(\boldsymbol{q})$ Scattering Intensity.

L Size of Ordered Domains.

L_{P} Persistence Length.

P Flocculation Parameter.

P_{n} Normalised Flocculation Parameter.

R_{g} Radius of Gyration.

S Nematic Order Parameter.

T Absolute Temperature.

T_{A} Agglomeration Temperature.

χ Flory Parameter.

δ_{i} Hildebrand Solubility Parameter.

η Dynamic Viscosity.

λ Wavelength.

ν Kinematic Viscosity.

ϕ Volume Fraction.

ρ Density.

$\boldsymbol{q}$ Scattering Vector.

a Cubic Lattice Constant.

c_n Ratio of (111) and (311) Peaks, Normalised with Calculated Values.

d_ctc Centre-to-Centre Distance.

d_f Fractal Dimension.

d_s Surface Gap of Particles in Closest Approach.

d_{hkl} Lattice Plane Distance.

$f(\vartheta)$ Orientational Distribution Function.

k_B Boltzmann Constant.

$p(r)$ Pair Distance Distribution Function (PDDF).

w Mass Fraction.

Pe Péclet Number.

Pe$_\mathrm{r}$ Rotational Péclet Number.

Re Reynolds Number.

1. Preliminary

1.1. Introduction

In the public perception, the term nanotechnology is still related to popular visions of utopian solutions to the challenges of our time. While artificial, nanoscopic universal machines [1] are still far from reality, the world is experiencing an increasing integration of products based on nanotechnology in everyday life[1]. In times where integrated circuits with nanoscale dimensions are widely used, standard sunscreen is based on titania nanoparticles and marketing is already overusing the term “nano”, nanotechnology might have lost its appeal as a buzz word and has arrived as a serious field of technology.

The multitude of available production processes for nanomaterials generally separate in two design paradigms: *Top-down* approaches start off with a bulk material that is subsequently refined to create a nanostructured material. The manufacturing of modern integrated circuits on silicon wafers is a typical example. *Bottom-up* methods rely on the use of smaller building blocks to create nanostructured materials. A classic example is the synthesis of gold nanoparticles from dissolved gold compounds, one of the earliest examples of practically applied nanotechnology (see section 1.2.1).

This dissertation contributes to the field of material design through bottom-up arrangement of colloidal building blocks. This strategy is particularly promising, because it allows control over the material properties by changing the particle type on the one hand and tuning the superstructure on the other hand. Due to the large number of constituent building blocks, it is generally not feasible to separately assemble the blocks into the structure, as it would be done in classical constructive engineering. The design strategies of usable amounts of nanomaterials so far all rely on the physiochemical interactions between the constituents to direct the assembly (self-assembly). Therefore it is crucial to understand the structure directing process parameters to actually design materials built from colloidal building blocks. This research seeks to not only find the *structure directing process parameters*, but also aims to illuminate the *relevant microscopic mechanisms.*

---

[1] Among nanoscientists, this is a common perception. Quantifying the actual production volume of products incorporating nanotechnology is surprisingly difficult [2].

A common way to classify compact superstructures of colloids is to differentiate between ordered superstructures and disordered superstructures. Ordered superstructures can be described as a periodically recurring unit cell, assembling a large scale structure. Disordered superstructure are distinguished by the absence of repeating structures on a length scale much larger than the individual colloid size[2]. It is commonly expected that an ordered superstructure will display enhanced collective effects and anisotropy in the physical properties, whereas a disordered superstructure exhibits less interparticle coupling effects (due to the reduced density) and has isotropic physical properties.

A typical use case for defined superstructures of gold nanoparticles is the design of optical metamaterials [3, 4]. A larger catalogue of nanoparticle superstructure-based devices opens up for other particle materials. Semiconductor nanoparticle superlattices constitute novel electronic devices [5], ordered [6] and disordered [7] superstructures of titania and silver particles serve different, structure-related purposes in thin film solar cells. This research is not aimed at finding specific procedures for the production of devices. The research goal is to gain insights on the structure formation mechanisms that can be beneficial for the design of many different assembly processes.

Colloids used as a starting material to build superstructures are easily synthesised in wet chemical syntheses. While this approach allows cost-efficient processes with surpassing quality control, the final material, e.g. a particle-based surface coating, often does not incorporate any solvent. Agglomeration is the process of phase separation of initially well-dispersed colloids into a solvent-rich and a colloid-rich phase.

Understanding the agglomeration process, deliberately induced or unwanted, is important for the design of materials. Ageing-related agglomeration effects have to be understood to account for possible pitfalls during storage or processing of the colloidal base material. Given the properties of the colloids as building blocks, the function of the material can be further tuned by changing the arrangement of the building blocks.

In a recent project directly preceding this study, it was established that the nanoparticle ligands, usually regarded as a stabiliser that prevents agglomeration, can play a crucial part to determine the structure of agglomerates that form upon addition of an agglomerating agent (see section 1.2.3.3 for further discussion). The objective of the present study is to extend these findings by

1. determining the structure directing process parameters and
2. deducing the underlying microscopic mechanisms.

---

[2] Due to their finite size and solid state, the distribution of the position of the colloids usually contains some structure at close distances.

The agglomeration process of three separate classes of gold colloids is investigated in this dissertation: Spherical particles with gold core radii from approximately 5.2 nm to 7.2 nm dispersed in water, with core radii from approximately 2.8 nm to 3.6 nm dispersed in unpolar solvents and ultrathin anisotropic nanowires with a thickness smaller than 2 nm and an aspect ratio well above 1 : 100. Given a particular particle type, the expected key process parameters are temperature and concentration of the involved substances (particles and agglomeration agent). The microscopic mechanisms are modelled with a focus on the role of the stabilising ligands.

The traditional experimental approach, *ex situ* preparation of agglomerating samples and subsequent characterisation with different methods, does not sustain large numbers of experiments (necessary to explore the process parameter space) and is inherently limited in time resolution (due to the finite integration time of the respective detectors).

These limitations entail a third objective of this research, the

3. development of a flow based system for *in situ* preparation and analysis of steady states of agglomeration of otherwise stable particle dispersions[3].

Using a flow based system to prepare an agglomerating particle sample and characterise the steady state arising at the fixed detector position is a novel approach. It can overcome the limitations on integration time and allows fast scanning of experimental parameters. A more detailed description is given in section 1.3.3.

The remainder of this work is briefly summarised in the following. After introducing several terms used throughout the present work, the state of the art concerning nanoparticle agglomeration experiments is briefly reviewed. The most relevant experimental techniques employed in this study are established in the remaining section of this chapter.

The agglomeration process of charge-stabilised, aqueous gold nanoparticles (AuNPs) upon addition of dilute hydrochloric acid is discussed in chapter 2. The measurements presented there were acquired at the MiNaXS beamline of the PETRA III synchrotron, employing a purpose-built flow setup. The feasibility of the flow-based approach on agglomeration experiments is demonstrated and the stabilisation mechanism of different surface modifications is assessed.

The formation of ordered superstructures directly from unpolar dispersion of sterically stabilised gold nanoparticles, induced by increasing the solvent polarity, is examined in chapter 3. For these measurements, the flow system was deployed at the SWING beamline of the source optimisée de lumière d'énergie intermédiaire

---

[3] There would be good reasons to label this objective as 1, because it had to be completed before the others.

du LURE (SOLEIL) synchrotron. *In situ* measurements establish the presence of superlattices during early stages of agglomeration and the importance of ligands and their solubility.

In chapter 4 the formation of ordered superstructures from gold nanowires is observed. All measurements were performed at the XEUSS 2.0 laboratory scale machine located at the INM. It is demonstrated that the wires can be preferentially aligned by exploiting the inherent flow field of the measurement system. These findings could help in the design of future coating setups, e.g. for transparent conductive coatings.

1.1.1. Definitions

A number of terms used ubiquitously in nanoscience are used ambiguously in different contexts. The sense in which these terms are used in this dissertation is explained here.

Nanoparticles (NPs) are often defined based on size limits in one or more dimensions [8]. In this research, nanoparticle will be used as a term for artificial three-dimensional (3D) objects with sizes in the range from 1 nm to 100 nm in all three dimensions. A typical gold nanoparticle (AuNP) employed in this research can be approximated reasonably well as a sphere, whose radius is smaller than 10 nm (see fig. 1.1). Most NPs can be envisioned as a particle surrounded by a stabilising shell. Gold cores with varying stabilising shells are used throughout this work.

Colloids are small ($< 1\,\mu$m at least in one dimension) insoluble particles suspended in a solvent due to Brownian forces. Alternatively they could be described as a heterogeneous mixture of liquid and solid, where the solid phase is finely divided. When the particles are stable over time and do not form clusters, they are called well-**dispersed**. The colloids used here are aforementioned AuNPs and so-called gold nanowires (AuNWs), anisotropic colloids in (approximately) cylindrical shape with aspect ratios > 500.

Polydispersity in size describes the phenomenon that the dimensions of the different particles constituting a colloidal dispersion are not identical (perfectly monodisperse), but usually distributed around an average size. When given as a number, it refers to the standard deviation of the size distribution of the corresponding colloid. For NPs it was generally determined by fitting small-angle X-ray scattering (SAXS) patterns and is given in units of length or relative to the mean radius. Often, particles with polydispersities $< 10\,\%$ are designated as monodisperse. While the IUPAC has deprecated the terms polydisperse and monodisperse in favour of the terms non-uniform and uniform respectively [9], they are used here due to their prevalence in the relevant literature.

Agglomeration is the formation of superstructures that consist of colloidal particles as building blocks. Destabilising a colloidal dispersion, e.g. by adding a destabilising agent, can induce agglomeration (see section 1.2.3). The particles attach to each other and form an agglomerate. Depending on the precise conditions, agglomerates with different morphologies can form, a principal topic of this dissertation. The term aggregation/aggregate is often used deviant from agglomeration/agglomerate. Here they will be used interchangeably.

Aggregation temperature (T_A) is used as a term for the ligand-dependant temperature below which the particles dispersed in pure heptane spontaneously agglomerate (see also section 1.2.3.3). The experiments in chapters 2 and 3 were performed at temperatures above T_A, to exclude temperature-induced agglomeration and constrain the study to solvent-induced effects.

Superlattice is a term used for ordered entities on the mesoscale in different dimensionalities. Here it is used for ordered arrangements of the respective colloids. Ordered means in this context that the large scale structure is comprised of a periodic repetition of a unit cell, which extends only on the (relatively small) scale of single particles. Under the right conditions, NPs agglomerate in ordered superlattices, similar to atomic crystallites (see fig. 1.5 and chapter 3). AuNWs can form superlattices too. They align in parallel and organise in two-dimensional (2D) lattices with a periodic superstructure, similar to smectic liquid crystals (see chapter 4).

Disordered agglomerate as a term includes all static colloid superstructures without long range translational order. Spatial correlations on small length scales are explicitly no exclusion criterion. Usually the constituents need to be in contact to experience an attractive force strong enough to build a static superstructure. Therefore, spatial correlations on the length scales of the single colloid dimension are usually found. Only for length scales on the order of several colloid sizes these correlations disappear. It is the decay of the spatial ordering that distinguishes disordered superstructures, also termed amorphous or glass-like, from ordered superlattices.

Batch experiments are the classical approach on laboratory investigations, where the sample is prepared in a laboratory, transferred to the proper measurement cell and left resting for the data acquisition. In the case of agglomeration experiments this means that the particle dispersion and agglomeration agent are mixed in a third container. As soon as the liquids are in touch, the agglomeration starts and progresses usually until all primary particles are depleted. The sample changes during the agglomeration process. To achieve a stable reference, often only the end product (a fully agglomerated sample) is investigated.

Steady-state experiments, also termed flow-based or online methods, are the main experimental approach chosen in this research. The sample is processed and analysed in a continuous solvent flow inside a sealed system. This leads to controllable conditions and largely enhances the capabilities for measurements, leading to faster and more reproducible experimentation. In this work, the flow processing approach allows observation of steady states of agglomeration over long periods of time, not achievable in batch processing (see also section 1.3.3).

Agglomerate age is an important quantity in the online experiments presented in this research. Usually, experiments were performed under constant flow conditions. In this case, the persistence time in the system does not change and a reaction initiated at one point along the flow path has progressed for a constant reaction time at a subsequent part of the flow path (see section 1.3.3). If this initiated reaction is an agglomeration process, the corresponding reaction time is denoted agglomerate age.

1.2. Nanoparticle Agglomeration

In this section, the groundwork for the research presented here is introduced. A short overview on nanoparticles and their interactions is given, before the current state of the art concerning nanoparticle agglomeration is reviewed.

1.2.1. Nanoparticles

Even when excluding the plethora of natural colloids found in biology from discussion, nanoparticles (NPs) have a long-standing history. The brief review given here is focused on AuNPs, mainly because in this research exclusively gold colloids were used, but also because they continuously drove innovation over the history of nanotechnology.

Predating modern nanotechnology by more than a millennium, Romans in the 4th century used a mixture of gold and silver NPs as pigments to colour glassware [10]. The particles dispersed in glass create a unique dichroic colour effect. The seminal study of Michael Faraday [11], in which he documented the synthesis and optical properties of AuNPs, dispersed in water, is often seen as the advent of modern colloid science. The synthesis of modern aqueous AuNPs was founded by the citrate reduction method of Turkevich [12, 13] and later improved by Frens [14, 15] (whose method was also used to synthesise particles for this research). Their synthesis protocols reliably yield monodisperse, approximately spherical AuNPs, charge-stabilised with citrate ions. Reliable synthesis of sterically stabilised particles dispersed in unpolar, organic solvents was pioneered by Brust [16]. The “Brust” method involves a laborious phase transfer step, modern methods yield comparable results from a single phase synthesis, e.g. the methods used for this research by Zheng [17] or Wu [18].

High resolution transmission electron micrographs of typical gold particles used in this research (fig. 1.1) image the gold cores, because the electron absorption of the ligand layer is negligible compared to the core.

The particle depicted in fig. 1.1 (a) is an example from an aqueous dispersion prepared after the “Frens” method [15], as described in section 2.2.1. The particle radius can be tuned by changing synthesis parameters. A typical value for the particles employed in this research is $r = 7.2 \pm 0.6\,\mathrm{nm}$ (determined by SAXS, see section 2.3).

The particles in fig. 1.1 (b) were prepared according to the so-called “Zheng” method (see section 3.2.1). The average radius, determined by averaging the projected areas in the TEM images of more than 500 particles, yielded typical values of $r = 2.8 \pm 0.3\,\mathrm{nm}$.

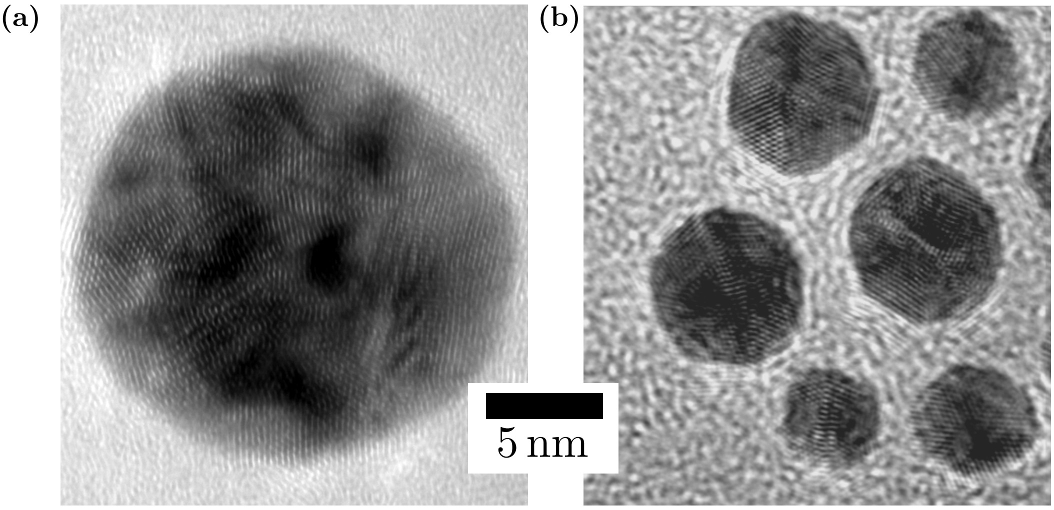

Figure 1.1.: Transmission electron micrographs of (a) aqueous gold nanoparticles, prepared with the “Frens” method [15] and (b) unpolar gold nanoparticles, synthesised with the “Zheng” method [17].

The particles are rarely applied directly after synthesis in the form of their dilute, stable dispersions. Most modern technological applications involve further processing of the as-synthesised dispersions. Understanding the colloidal interactions that determine the ubiquitous agglomeration phenomenon is important for successful processing.

1.2.2. Interactions

It is important to understand the microscopic interactions acting on the colloids to understand the concepts of colloidal stability and destabilisation. The interactions directly influence crucial properties such as the ageing behaviour and the structure resulting from drying, agglomeration and any other form of self-assembly. In the following, the most important interaction types, especially with a view to agglomeration, are discussed.

The DLVO theory [19, 20] provides a common framework to discuss colloidal interactions. Even though some of the underlying assumptions are known to be incorrect at close inspection, the theory was successful in explaining a number of colloidal phenomena [21]. The idea of the theory is to summarise certain expressions for the interaction energy resulting from van der Waals and electrostatic forces. A common approach to account for additional interaction types is to add the corresponding interaction potential to the DLVO potential.

1.2.2.1. Van der Waals Interactions

The van der Waals interaction is an ubiquitous interaction in the microscopic regime. These forces act between all atoms and molecules, from noble gas atoms to gold nanoparticles. They originate from the dipolar interactions between the constituents. Even for unpolarised interacting entities there are induced dipolar interactions.

The principle can be explained by considering that while the electrons of an unpolar particle are distributed evenly, at a certain point in time they possess asymmetry (due to quantum mechanical fluctuations) that entails a finite dipole moment. This dipole generates an electric field that can polarise the surrounding particles. The resulting interaction between the dipole resulting from fluctuations and the induced dipole constitute the van der Waals interaction [22, p. 107]. For similar particles the resulting interaction is attractive[4].

---

[4] Under the right circumstances the van der Waals interaction between two different materials in a third medium can become repulsive. This case is not relevant for this research.

In the context of this research, the interaction of spherical gold particles dispersed in a solvent is particularly relevant. The interaction energy U_{vdW} of two spheres with radius R, separated by a distance $r << R$ can be written as [22, p. 326]

$$U_{\mathrm{vdW}} = A_{\mathrm{Au}} \cdot \frac{R}{12r}. \tag{1.1}$$

At large separations the interaction potential decays as $U_{\mathrm{vdW}} \propto -r^{-6}$. A_{Au} is the Hamaker constant [22, p. 253]. It measures the interaction strength of the particles and is a material constant ($A_{\mathrm{Au}} \sim 5 \times 10^{-19}\,\mathrm{J}$ for gold interacting in vacuum). Usually the particles interact through a medium, the solvent, the effect of the solvent can be accounted for by using the effective Hamaker constant

$$A_{\mathrm{eff}} = \left(\sqrt{A_{\mathrm{Au}}} - \sqrt{A_{\mathrm{S}}}\right)^2. \tag{1.2}$$

A_{S} denotes the Hamaker constant of the medium between the interacting spheres. Approximations for the interaction energies of other geometries than in eq. (1.1) are available in the literature (e.g. [22, p. 254]).

In summary, the Hamaker constant determines the magnitude of the van der Waals attraction for a given geometry.

1.2.2.2. Electrostatic Interactions

In contrast to van der Waals interactions, electrostatic interactions can only occur when charged interaction partners exist. Since surfaces in aqueous environment are generally charged [22, p. 291] and the electrostatic interaction is more long-ranged than the van der Waals interactions, it is critically important for aqueous colloids. Systems where exclusively charges are used as stabilisation are often termed “charge-stabilised”.

Dissolved ions are a general feature of aqueous media. A charged surface attracts oppositely charged ions and an ion concentration gradient is formed at the surface, the diffuse electric double-layer. The so-called double-layer is comprised of three parts: The charged surface, a surface-bound layer of counterions and a more loosely attached, diffuse layer with increased counterion concentration compared to the bulk.

The ion layers screen the effective electrostatic interactions with the charged surface, since the surface charge is locally balanced by the ions. The strength of the effect is characterised by the so-called Debye length $\frac{1}{\kappa}$, a measure for the thickness of the counterion layer. The thickness for a constant temperature solely depends on the electrolyte type and concentration. For increasing concentrations/ionic strengths, the Debye length decreases and the range of the electrostatic interaction is reduced likewise due to extended screening.

The effective interaction at close approach between equally charged spheres in an electrolyte can be understood as a repulsion between their respective double-layers[5]. The interaction energy U_E for the case in eq. (1.1) can be written as [22, p. 317]

$$U_\mathrm{E} = \frac{1}{2} R Z e^{-\kappa r}. \tag{1.3}$$

Here, Z is the so-called interaction constant that depends only on the surface properties (except the valency of the electrolyte) [22, p. 316]. Z increases with increasing surface potential, which in turn increases with the surface charge. At large separations, the potential decays as $U_\mathrm{E} \propto e^{-\kappa r}/r$. Approximations for other geometries are found in literature [22, p. 317].

In summary, the strength of the surface charge and the ionic strength of the solvent determine the magnitude of the electrostatic interaction for a given geometry.

1.2.2.3. Steric Interactions

Steric interactions between spherical nanoparticles dispersed in a solvent involve a third component, often a polymer either bound to the particles or dissolved, which introduces complex entropic effects. Depending on the details, the resulting forces can be attractive or repulsive.

Chain molecules that are highly soluble in the solvent and adsorbed on the nanoparticle surface can act as sterical stabilisation [22, p. 387]. Without loss of generality, the following discussion is limited to AuNPs with alkylthiols covalently bound on the surface. It is further assumed that the alkyl chain is long enough to be regarded as a polymer, to ensure that classical polymer theories are applicable[6]. On the one hand, they impede irreversible agglomeration by preventing direct contact of the gold surface. On the other hand, the loss of configurational entropy of molecules for overlapping monolayers results in a repulsive force that acts to reduce the overlap and enhances the stabilisation effect.

Conversely, the same molecules can mediate an attractive interaction if they are poorly soluble in the solvent [22, p. 394]. This can be intuitively understood when considering that identical chains are mutually highly soluble. If the continuous phase is a bad solvent for the ligand chains, they will preferentially dissolve in

---

[5] The minimum intersurface distance for particles in stable dispersion is given by the position of the energy barrier peak (see fig. 1.2). It can be estimated as $h_0 \gtrsim \frac{1}{\kappa}$, the screening length.

[6] The phenomena observed in this research can be explained in this framework, although the small length of the alkyl chains employed in chapter 3 challenges many assumptions of classical polymer physics. It is common practice to apply polymer theories also for short alkyl chains as nanoparticle ligands due to the lack of more refined analytic pair potentials for such systems [23].

neighbouring ligand layers, effectively generating an attractive force. Depending on the mobility of the ligand chains, they might support or impede lateral displacement of the particles.

The interaction energy for overlapping ligand layers (with separations larger than a single ligand length ℓ) can be written as

$$U_{\mathrm{Overlap}} = k_{\mathrm{B}}T\frac{\pi R}{V_{\mathrm{s}}}\phi_{\mathrm{av}}^{2}\left(\frac{1}{2}-\chi\right)\cdot(r-2\ell)^{2}\,, \tag{1.4}$$

where V_{s} is the volume of a solvent molecule, ϕ_{av} the volume fraction of the ligands in the shell surrounding the particles and

$$\chi = \frac{V_{\mathrm{s}}}{k_{\mathrm{B}}T}\left(\delta_{\mathrm{s}}-\delta_{\mathrm{m}}\right)^{2}+0.34 \tag{1.5}$$

the Flory parameter [23]. δ_{s} and δ_{m} are the Hildebrand solubility parameters of solvent and ligand respectively. For chemically similar solvent and ligand molecules, the solubility parameters are similar. The resulting interaction energy is positive, leading to a repulsive interaction. If the solvent and ligand molecules are not similar, e.g. polar ethanol as solvent and unpolar dodecanethiol as ligand, their solubility parameters are different ($\delta_{\mathrm{EtOH}} = 2.62\times10^{4}\,\sqrt{\mathrm{Pa}}$ and $\delta_{\mathrm{C12}} = 1.65\times10^{4}\,\sqrt{\mathrm{Pa}}$ [24, 25]). This leads to a Flory parameter larger than $\frac{1}{2}$ and therefore negative interaction energies and results in an attractive interaction mediated by the ligands.

The depletion force results from a third entropy-related interaction mechanism. It requires a separate dissolved or dispersed macromolecule among the particles with somewhat smaller dimensions, such as a short polymer or smaller particles [26–28]. The origin of the depletion force is best explained with a thought experiment. When two parallel plates immersed in a solution of macromolecules are approached and the gap size reaches the size regime of the macromolecules, the macromolecules between the plates become confined and are therefore restricted in their movement and conformations. This creates an entropic penalty in the free energy that leads to a force driving the macromolecules out of the gap, below a certain gap size the clearance will additionally be just too small to accommodate the macromolecules. For both cases the concentration of macromolecules between the plates is smaller than in the bulk solution. This creates osmotic pressure, pushing the plates further together and hence effectively creates an attractive force [22, p. 398]. Increasing the concentration of the dissolved macromolecules, often also termed depletants, increases the osmotic pressure and likewise the attractive force.

For spherical colloids that approach close enough to create an excluded volume V_{ov} for the depletants with number concentration n_{d}, the interaction energy is [29, p. 62]

$$U_{\mathrm{Depletion}} = -k_{\mathrm{B}}Tn_{\mathrm{d}}V_{\mathrm{ov}}, \tag{1.6}$$

so the energy and the resulting force are directly proportional to the concentration of the depletants.

In summary, the strength of the ligand-mediated steric interactions depends on the solubility of adsorbed molecules in the continuous phase. The magnitude of the depletion force can be tuned by changing the concentration of dissolved depletants.

1.2.2.4. Generic Shape of the Interaction Potential

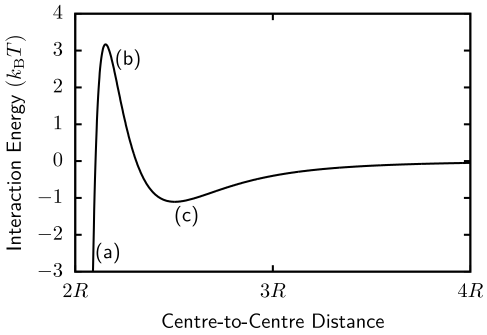

Figure 1.2.: Generic shape of the interaction potential between two nanoparticles.

Depending on the relative magnitude of aforementioned interaction potential, the resulting energy landscape can have different shapes. The general shape of the real interaction energy between two particles in stable dispersion often resembles the sketch in fig. 1.2, regardless the actual nature of the attractive and repulsive contribution.

The generic profile has three distinct features (fig. 1.2 (a)–(c)).

(a) At centre-to-centre distances close to the particle diameter, the van der Waals attraction dominates and leads to a deep, attractive well, the “primary minimum”[7].

(b) The stabilising interaction energy (electrostatic or steric) overcomes the van der Waals attraction and causes a repulsive peak in the profile. This energy barrier (height $U_{\max}$) prevents particles from agglomeration. If the barrier is too small, it can be overcome by Brownian motion and agglomeration is initiated.

(c) For repulsive energies that are small enough, a secondary minimum in the energy landscape forms. Particles either remain in the secondary minimum for low repulsion or stay dispersed for shallow secondary minima.

---

[7] When the surfaces contact each other, the Pauli repulsion overcomes the van der Waals potential and impedes further approach.

The interactions described above determine the agglomeration process of many particle systems. Relevant studies on nanoparticle agglomeration are reviewed in the next part.

1.2.3. Nanoparticle Agglomeration: State of the Art

Studies on nanoparticle agglomeration can be categorised based on their approach to induce agglomeration. Amongst others, confinement addition of an agglomeration agent are common approaches to assemble particles.

Solvent evaporation is a widespread method to confine nanoparticles and create superlattices [30, 31]. Colloidal crystallisation in supercrystalline structures of monolayer protected AuNPs was first achieved by slow evaporation [32, 33]. The structure-directing mechanism for superlattice formation during solvent evaporation is generally assumed to be the entropy gain for structures where all particles maximise their individual freedom of motion. The interparticle interactions have to be small for the entropic mechanism to prevail. Particles with strong interaction forces require alternative methods for superlattice formation.

Another option to create superlattices is the deliberate destabilisation of the dispersion by changing the composition of the continuous phase [34]. Depending on the type of stabilisation, the method offers a distinct phenomenology.

1.2.3.1. Charge-Stabilised Systems

Purely charge-stabilised particles can be destabilised by changing the ion composition of the electrolyte. The surface potential is determined by specific ions. Usually, the H_3O^+/OH^- ions in aqueous dispersion and therefore the pH changes surface potential. If the potential is sufficiently small, the van der Waals attraction can overcome the electrostatic repulsion and the particles agglomerate. By increasing the total ion concentration, i.e. the ionic strength, the surface potential is increasingly screened and at some point the attractive dispersion interaction overcomes repulsion. Agglomerates grown by destabilisation of purely charge-stabilised systems containing a single particle type, however, have not been demonstrated to form ordered superlattices to the best of the author's knowledge[8]. Conversely, the agglomerates grow in a fractal shape. The agglomeration kinetics determine the fractal dimension of the agglomerate [36].

The Smoluchokwski coagulation equation [37] balances the different populations of single particles and differently sized agglomerates during the (irreversible) growth

---

[8] This restriction does not apply for binary dispersions with oppositely charged particles, which are intrinsically unstable and can grow in superlattices [35].

process. If n_l denotes the number density of agglomerates consisting of l particles (l-mers) and $l = i + j$, the change in the population is

$$\frac{\partial n_l}{\partial t} = \frac{1}{2} \sum_{i=1}^{l-1} k_{ij} n_i n_j - n_l \sum_{k=1}^{\infty} k_{il} n_i. \tag{1.7}$$

The first term accounts for the creation of agglomerates by collisions of other agglomerates, the second term accounts for the loss of agglomerates with k particles by collisions with other agglomerates. The k_{ij} determine the rate at which i-mers attach to j-mers [38, p. 159].

Generally, agglomerate growth kinetics can be described by different kernels k_{ij}, which describe the relative attachment rates during agglomeration.

Depending on the shape of the growth curve, agglomeration processes are usually categorised as reaction-limited agglomeration (RLA) or diffusion-limited agglomeration (DLA).

The agglomeration process can be considered as a two-step process. First, the constituents are transported diffusively to the binding site before they actually attach in the second step. The DLA and RLA regimes are discriminated based on the effective bottleneck of the growth process.

The rate-limiting process for *diffusion-limited agglomeration* is the diffusive approach of the constituents. These processes occur for sufficiently small energy barriers for the attachment of constituents, where the diffusion of the constituents is significantly slower than the attachment process. The agglomerate size L grows like a power law,

$$L \propto t^{\frac{1}{d_\mathrm{f}}}, \tag{1.8}$$

and d_f is the fractal dimension of the agglomerate [39].

The fractal dimension d_f allows conclusions on the topology of an agglomerate. It measures the coupling between the size, e.g. evaluated by the radius of gyration R_g, and the number of constituent particles N for an agglomerate [40, p. 281],

$$N \propto R_\mathrm{g}^{d_\mathrm{f}}. \tag{1.9}$$

The limiting cases are linear particle chains ($d_\mathrm{f} = 1.0$) and close packed, isotropic structures ($d_\mathrm{f} = 3.0$).

Agglomerates grown in the DLA regime have a fibrillar, open structure [41]. In its early stages, the growth process is mainly determined by doublet formation. The kernel or rate constant for the formation of dimers from monomers

$$k_{11} = \frac{8 k_\mathrm{B} T}{3 \eta} \tag{1.10}$$

only depends on the solvent viscosity η and temperature T [38, p. 161]. It describes the decrease of the primary particle number density n_1 via

$$\left(\frac{\partial n_1}{\partial t}\right)_{t\to 0} = -k_{11} n_1^2. \tag{1.11}$$

The growth rate for *reaction-limited agglomeration* is determined by the close range interaction energies. When the potential includes a repulsive barrier, the attachment of the constituents can be slowed down sufficiently to dominate the growth rate. If the height of the repulsive barrier is U_{max}, the reduction in growth rate from eq. (1.10) is often approximated by

$$k_{11}^{\mathrm{effective}} = 2\kappa R \exp\left(-\frac{U_{\mathrm{max}}}{k_{\mathrm{B}}T}\right) k_{11} = \frac{1}{W} k_{11}, \tag{1.12}$$

where κ is the inverse Debye length and R the particle radius. W is the so-called stability ratio. $k_{11}^{\mathrm{effective}}$ can then be used in eq. (1.11) instead of k_{11} to describe the reduction in monomer concentration in a reaction-limited process. The size of agglomerates L grows exponentially,

$$L \propto e^{\frac{t}{\tau}}, \tag{1.13}$$

where τ determines the time scale and depends on the experimental details [42]. The resulting agglomerates are compact [39]. Typical reaction limited processes are strongly temperature-dependant.

When a charge-stabilised colloid is destabilised through reducing the screening length by increasing the electrolyte ionic strength, the energy barrier is continuously lowered. At small ionic strength the reaction limited growth is strongly influenced by the ion concentration. After a certain threshold, the critical coagulation concentration (ccc), is crossed, the barrier is negligible compared to thermal energy and further screening of the charges by and increase in ionic strength does not accelerate the process further. The typical behaviour of the stability ratio upon changes in agglomeration agent concentration [38, p. 173] is sketched in fig. 1.3.

The late stages of an initially reaction-limited agglomeration process are usually diffusion-limited. After all single particles are depleted and agglomerates grow solely by coalescence with other agglomerates, the small diffusion constants of large agglomerates dominate the kinetics.

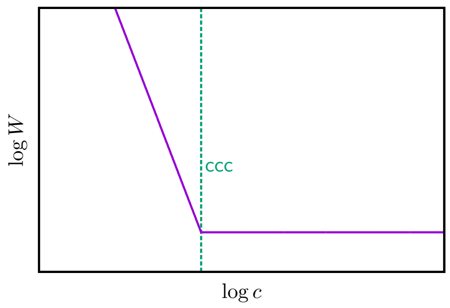

Figure 1.3.: Below the critical coagulation concentration (ccc) the reaction limited dynamics depend strongly on the agglomeration agent concentration, the stability ratio drops. Above the ccc the barrier has vanished and the stability ratio remains constant, the kinetics are diffusion-limited.

1.2.3.2. Sterically Stabilised Systems

Many modern nanoparticles employed in functional materials (e.g. semiconducting quantum dots, high refractive index zirconia, conductive indium tin oxide) are sterically stabilised and dispersed in unpolar media. Their interactions are more tunable due to the additional degrees of freedom evoked by the ligand molecules. Under the right conditions, destabilised suspensions can form ordered superlattices.

The most common approach to create ordered superlattices by destabilisation in current literature is to add poor solvent at a minuscule rate [34, 43, 44]. Typically a barrier, e.g. an insoluble solvent or a phase boundary, is placed between the incompatible solvent and the dispersion. The poor solvent molecules then slowly diffuse into the dispersion. The gentle solubility decrease induces gradual agglomeration that can take place on time scales up to months.

The underlying mechanisms governing the superlattice formation process are still debated, amongst other reasons because all interaction effects discussed above are similar in magnitude and small shifts in their balance can have pivotal effects. The close packing of an ordered superlattice represents a free energy minimum in most cases. Generally, kinetic arrest by close ranged attraction is assumed to potentially be able to freeze agglomerates in metastable states. Therefore it is important to control the magnitude and discrete nature of the attractive interaction to achieve reliable superlattice growth. Classically, the van der Waals interaction is considered the attractive component for agglomerating particles [45]. The attraction caused by ligands with limited solubility recently came into focus too [46]. Additionally, some more subtle effects have been found, e.g. an influence of residual charges on the particles [47]. Another subtle effect, related to the phase state of the ligand monolayer, has been highlighted in a recent research project [48, 49]. The study directly precedes this research project, especially chapter 3, and the key findings are illustrated in the following section.

1.2.3.3. Directly Related Studies

Earlier studies on the agglomeration of sterically stabilised AuNPs dispersed in heptane found a surprising interplay between ligand phase behaviour and agglomerate structure. A new method to create ordered superlattices by rapid destabilisation was established.

In the first part of that study, the temperature influence on the colloidal stability was examined [49]. It was found that the dispersions were destabilised below a certain ligand dependant aggregation temperature T_{A}, values are plotted in fig. 1.4. The aggregation temperature corresponds to the melting temperature of the pure ligands. The origin of the aggregation was reduced solubility of the ligands in the dispersion medium below the aggregation temperature (see section 1.2.2.3). The method yielded only disordered agglomerates without a long range ordered superstructure.

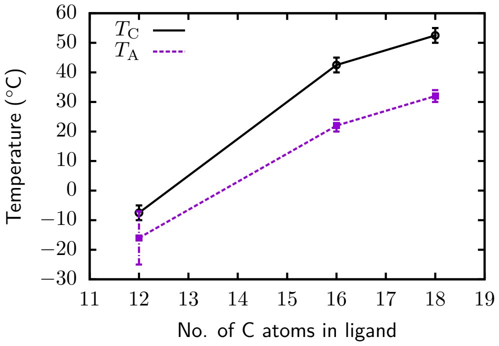

Figure 1.4.: Shorter ligands and higher temperatures promote ordered agglomeration. The dispersions are unstable below the Aggregation Temperature.

Kinetic arrest due to the strong, short-ranged, ligand-mediated attraction was hypothesised as the reason for the exclusive formation of glassy agglomerates. The experimental protocol was modified to increase the particle mobility and therefore prevent arrest. To achieve more mobility, experiments were performed at higher temperatures in a second study [48]. To induce agglomeration at temperatures where the dispersion itself is stable (above T_{A}), the ligand solubility in the solvent was reduced by increasing the polarity of the solvent. An equal volume of 1-propanol was rapidly mixed with the dispersion. After 2 h waiting time, most of the particles were agglomerated and precipitated. The agglomerate structure was then determined mainly *ex situ* by transmission electron microscopy (TEM) and additional SAXS experiments.

The morphology of the agglomerates was found to depend on the processing temperature that was set during the agglomeration: Above a ligand dependant crystallisation temperature T_C (see fig. 1.4), agglomerates with a periodic superstructure of the particles can be found. Below T_C the particles are arranged randomly inside the agglomerates.

The results of the aforementioned studies were replicated in preparation of this research. After the synthesis protocol ("Zheng" method in section 3.2.1) was improved to reduce batch to batch variations, the principal results were confirmed. A TEM tilt series (fig. 1.5) of an agglomerate prepared by precipitation of hexadecanethiol-stabilised AuNPs at 50 °C ($> T_\mathrm{C}$), following the protocol from [48], illustrates the supercrystalline structure of the agglomerates.

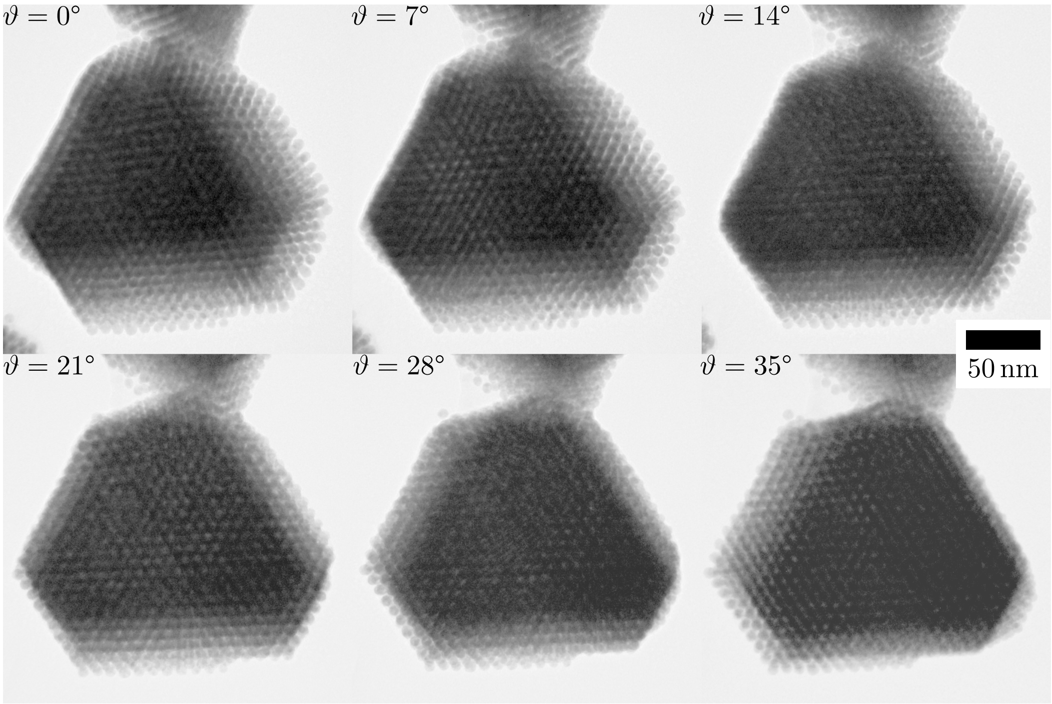

Figure 1.5.: TEM images of an ordered agglomerate taken at different rotations around the vertical axis ϑ.

The minimum temperature for the occurrence of ordered agglomerates, T_C, was found to coincide with the melting temperature of the ligand monolayer. At high temperatures the stabilising layer is molten [50]. The ligand chains act as a lubricating layer between the particles in an agglomerate and the particles can find the minimum energy positions of an ordered lattice. Below T_C, the ligand monolayers form rigid crystallized domains that impede the interparticle movement inside an agglomerate. The particles can not explore the complete phase space and are arrested in an energetically less favourable glass-like structure.

The solvent induced agglomeration experiments stand out from similar studies found in literature, because the polar solvent is added by rapid mixing instead of slow addition. The method is therefore preferable for actual applications, where a more defined mixing process is desirable and processing times are usually kept as short as possible.

While it could demonstrate the presence of supercrystalline order under the right conditions, some points were not addressed:

- The internal structure of agglomerates could not be resolved,
- the influence of solvent composition was not examined,
- the samples were prepared manually, which lead to poor control of the critical mixing step,
- measurements were performed *ex situ* and relied mostly on transmission electron microscope (TEM) images that could suffer drying artefacts, and
- the agglomerates were only examined after the agglomeration process was terminated.

In the next section, the approach of this study to address these open questions for the system described above is introduced.

1.2.3.4. Flow-Based Studies

The core idea of this dissertation is to use a flow-based system to prepare and analyse steady states of agglomeration *in situ*. While it is the first study that allows to examine a continuous flow of a destabilised suspension, related results have been published before.

In the last two decades, syntheses of colloidal particles in flow reactors have emerged from research laboratories to commercial application. Nanoparticle synthesis in continuous microfluidic reactors has first been reported in 2002 [51]. Many applications benefit from compartmentalisation of the reaction volumes in liquid plugs or droplets [52]. Modern continuous flow syntheses include online characterisation of the particles [53] that allows in principle real time process optimisation. Compared to the classical batch reactions, the flow syntheses offer superior control on the reaction conditions (e.g. temperature, mixing and timing) and hence yield improved products.

Studies on nanoparticle agglomeration would benefit from the same advantages. To the best of the author's knowledge, there are no published studies where the agglomeration process of metal nanoparticles was initiated and analysed in a continuous flow setup. An existing approach to observe agglomeration processes is the so-called stopped flow method [45]. While it also allows to detect early stages of fast kinetics, the observed sample is not in a steady state and the achievable integration times are small. This often necessitates many repetitions before a meaningful result is obtained, making the method prone to errors resulting from fouling and other batch-to-batch variations.

Continuous flow studies on the reaction kinetics of soft colloids are known in literature, often they employ purpose-built microfluidic channels [54, 55]. In this research, the idea to translate the spatial position along the flow path to the associated point in time is adopted from these studies.

1.3. Measurement Techniques

All three research areas discussed in this dissertation revolve around the idea of using a millifluidic flow system[9], where agglomeration of a continuous sample flow is triggered at a mixing element and the resulting steady states of agglomeration at fixed downstream positions are analysed with coupled detectors. A millifluidic system was favoured over a microfluidic design to avoid clogging of the channels by large agglomerates, while retaining the inherent superior control of process parameters and the possibility to observe early stages of the structure formation process (a process with short time scales) with arbitrary integration times. A more detailed description of the approach follows in section 1.3.3.

As a start, the main measurement techniques successively coupled are outlined in the following. While ultraviolet-visible (UV/Vis) spectroscopy is a quick standard method to characterise the optical properties of gold nanoparticles and their agglomerates, SAXS provides deeper insight into the interparticle interaction and agglomerate structure.

1.3.1. UV/Vis Spectroscopy

The optical absorption of metal nanoparticles is dominated by the localized surface plasmon resonance (LSPR) peak (a typical example is shown in fig. 1.7). Stringent theories on the origin of the phenomenon are found in literature, either in a classical electrodynamic model ("Mie Theory"[56–58]) or in a fully quantum dynamic treatment [59]. Here it will be explained in the framework of a more accessible semiclassical model.

---

[9] Millifluidic refers to the fact, that the internal dimensions are in the millimeter range.

The electrons in a metal nanoparticle form an electron gas[10], as sketched in fig. 1.6 (a). The particle does not possess a dipole moment. When the electron cloud is excited by an external electric field, e.g. by a single pulse of light with finite width, it is shifted against the more inert, positively charged nuclei and the accumulated charge at the surface forms a dipole (fig. 1.6 (b)). When the external field drops, the system relaxes (fig. 1.6 (c)). During relaxation, the excited electron cloud performs a damped oscillation with a certain resonance frequency[11] ω_M and decaying amplitude (fig. 1.6 (c)). If the particle is continuously irradiated with white light, the resonance frequency couples stronger to the electron oscillation than all other frequencies. Light at the resonance frequency is therefore absorbed most and the aforementioned LSPR peak in the absorption spectrum is induced.

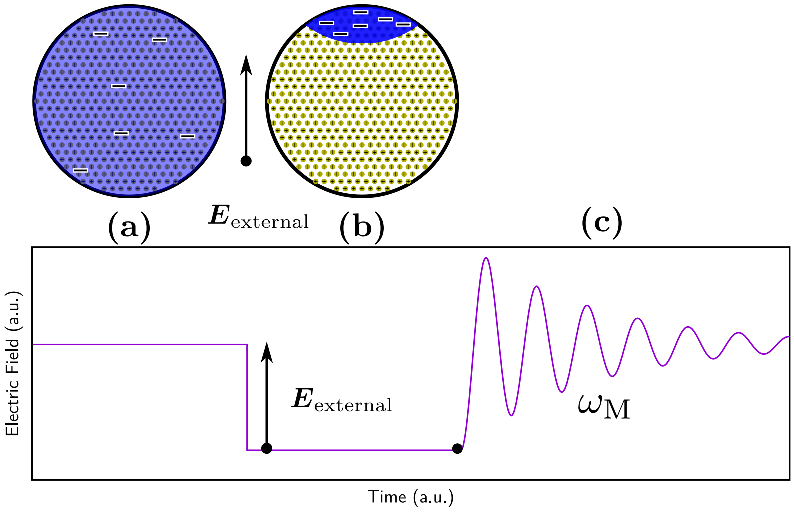

Figure 1.6.: Localised surface plasmon resonance.

The shape and position of the absorption peak for well-dispersed, dilute particles is influenced by the particle shape [62], size [63–65][12], the adsorbed surface molecules [67], and the dielectric constants of the surrounding medium and the particle [57, 58].

The displacement of the electron cloud creates charge accumulation at opposing sides of the particle which is accompanied by a dipole moment. If two or more

---

[10] This is a quantum mechanical effect known from the Drude-Sommerfeld model [60, pp. 131 ff.].

[11] The resonance frequency depends on the geometric and dielectric details of the particle [61]. A resonance wavelength around $\frac{2\pi c}{\omega_\mathrm{M}} = 520\,\mathrm{nm}$ is typical for the gold particles employed here.

[12] In the radius range used in this work ($2\,\mathrm{nm} < R < 50\,\mathrm{nm}$), the size dependency is introduced by a size dependant dielectric function, because the mean free path of electrons has the magnitude of the particle size [66].

particles are in close proximity, their dipole fields will influence each other. Interparticle coupling usually induces a redshift in the LSPR peak position, with decreasing distance the redshift increases [64, 68]. For ordered lattices in 2D, an influence of the lattice type on the spectra has been reported in a theoretical study [69]. This allows the assessment of the agglomeration state of a AuNP sample based on the absorption spectrum.

The method of choice to characterise the absorption of metal nanoparticle dispersions is solution based UV/Vis spectroscopy. UV/Vis spectroscopy is a spectroscopic technique in the visible spectrum and the neighbouring ultraviolet and infrared parts[13]. The relatively simple experimental setup makes UV/Vis absorbance spectroscopy, measured in transmission, one of the most widespread analysis techniques. The optical properties of metal nanoparticles and their agglomerates make them an ideal sample for UV/Vis absorbance measurements.

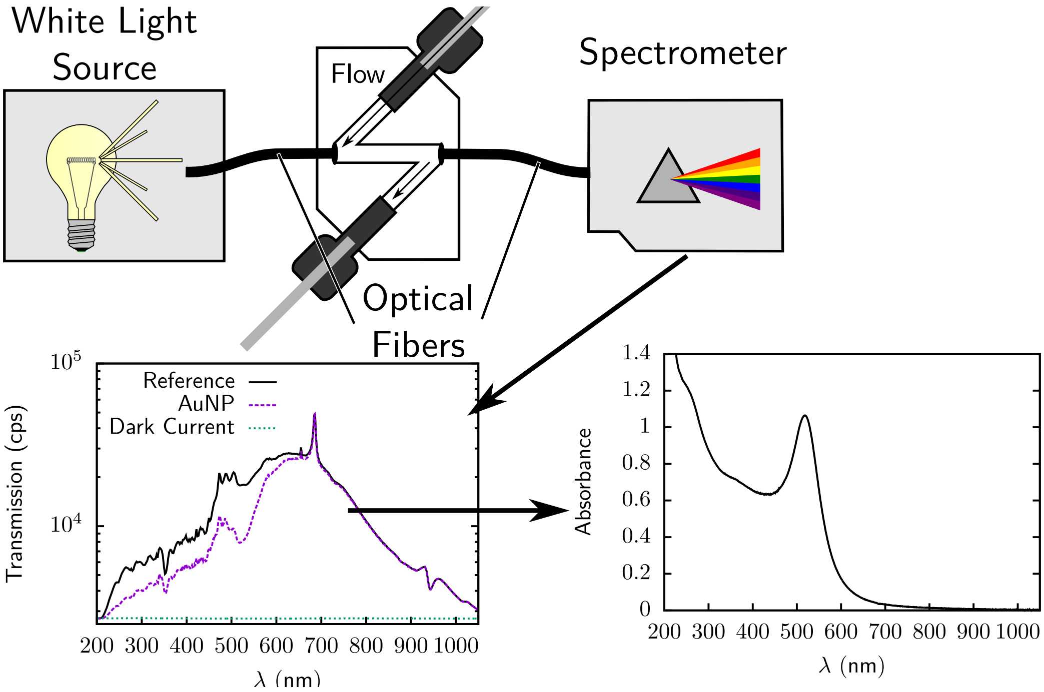

Figure 1.7.: UV/Vis Spectrometer Scheme.

The single beam, flow cell based setup that was mainly used for the UV/Vis measurements is sketched in fig. 1.7. A combined deuterium and halogen based lamp (Micropack “DH-2000-BAL”) is an intense white light source. The white light is transmitted through the fused silica windows of a polymer sample flow cell with

---

[13] The spectrometer used in most of this research works in the range of 215 nm–1110 nm.

a z-shaped cavity to increase the optical path through the sample flow. The Ocean Optics “USB2000+” spectrometer detects the transmitted spectra with a grating and a linear charge-coupled device (CCD) detector. The optical components are connected with standard glass fibres. The inlet and outlet of the sample cell are connected with standard high performance liquid chromatography (HPLC) tubing, which can be fed by hand with a syringe or with a pump. The modular setup allows fast modifications and flexible integration into different experimental environments.

The absorption of radiation by a homogeneous, dilute dispersion can be described by the Lambert-Beer law [70]. It states that the transmitted intensity $I_\mathrm{s}(\lambda)$ decays exponentially with the beam path through the sample d, the sample concentration c and a material dependant (also relating to the choice of concentration units) extinction coefficient ε_λ:

$$I_\mathrm{s}(\lambda) = I_\mathrm{ref}(\lambda)\, e^{-\varepsilon_\lambda \cdot c \cdot d}. \tag{1.14}$$

Here I_ref is the transmitted intensity of the continuous phase without the dispersed phase.

To calculate the absorbance $A(\lambda)$ of a dispersed or dissolved sample, the transmission spectra of the pure continuous phase $I_\mathrm{ref}(\lambda)$ and the dispersion $I_\mathrm{s}(\lambda)$ have to be recorded. Typical transmission measurements are plotted in the left graph of fig. 1.7. Taking into account the dark count rate of the CCD $I_\mathrm{dark}(\lambda)$, the absorbance $A(\lambda)$ [71] is calculated as

$$A(\lambda) = \log_{10}\left(\frac{I_\mathrm{ref}(\lambda) - I_\mathrm{dark}(\lambda)}{I_\mathrm{s}(\lambda) - I_\mathrm{dark}(\lambda)}\right). \tag{1.15}$$

The absorbance of citrate-stabilised AuNPs, calculated from the measurements displayed in the left graph in fig. 1.7, is shown in the right graph. The absorbance is the largest, where the difference between sample transmission and solvent transmission is the largest. The most significant feature of the AuNP absorbance is the LSPR peak at 518 nm. It is a well known feature of AuNPs in the size range from 2 nm–100 nm and corresponds to the red colour of nano sized gold particles.

For all UV/Vis measurements presented in this dissertation, a reference measurement of the solvent without the absorbing sample and a dark current measurement were performed before the measurement of the sample. The absorbance for selected measurements was then calculated with a specifically developed Python[14] tool. In the following, only the absorbance curves $A(\lambda)$ are presented.

It should be noted here that technically the term absorbance is incorrect for the measured quantity. The actual value determined in a typical UV/Vis spectrometer

---

[14] Python is a scripting language. Due to many available numeric and scientific libraries, Python was most suitable for the calculations in this research.

setup is the decrease of transmission due to the dispersed substance, usually referred to as extinction. Absorption is one contribution to the extinction of light, but light scattering will also reduce the transmitted intensity. The scattered intensity in the UV/Vis portion of the spectrum is orders of magnitude smaller than the absorbed intensity for gold nanoparticles in the size range studied here, hence absorption is used synonymously with extinction.

1.3.2. Small-Angle X-ray Scattering

Small-angle X-ray scattering (SAXS) is a versatile technique to determine sample structures on a nanoscale [72, 73]. While it is based on the phenomenon of Thomson scattering, the technique can be introduced in different ways, e.g. starting from the interaction of a plane wave with a point scatter (in this case a monochromatic X-ray beam and an electron). In the framework of classical crystallography it could be understood as peak broadening of the (000) reflection, while from a more mathematical point of view the scattering pattern is the magnitude of a slice through the 3D Fourier transform of the electron density contrast of the sample [74].

It is employed on diverse areas as biology, materials science or physics since the earliest studies [75]. Typically the equilibrium structure of two phase materials is determined. For samples out of equilibrium the necessary integration time is critical. In this research, steady state flow experiments as an approach to alleviate this issue are a principal theme (see section 1.3.3)[15].

X-rays are elastically scattered at electron density gradients. The scattering angle contains information on distances inside the sample. It becomes clear in eq. (1.18) that small structures scatter photons to large angles and larger structures scatter to smaller angles. In the angular range typically probed in SAXS (scattering angle $2\Theta \lesssim 10°$), the structure of nano- and mesoscale objects can be analysed.

In this research three different SAXS instruments were used. This was feasible because of the modular design of the system (section 1.3.3). The same flow-capillary design only had to be adapted to different sample holders of the different facilities, which was possible with only slight modifications. The measurements on the agglomeration of aqueous AuNPs, presented in chapter 2, were performed at the High Brilliance Beamline ID02 at the European synchrotron radiation facility (ESRF) and the Micro- and Nanofocus X-ray Scattering Beamline P03 at the PETRA III synchrotron at the Deutsches Elektronen-Synchrotron (DESY) facility. The data for the agglomeration of alkylthiol-stabilized particles, discussed in chapter 3, was recorded at the SWING beamline of the synchrotron SOLEIL and with a laboratory

---

[15] For many samples, the integration time can be minimised by increasing the incoming intensity. This and the rising interest in weakly scattering samples helped the advent of synchrotron SAXS experiments in the last 40 years.

scale SAXS-machine, the XEUSS 2.0 from XENOCS. The orientation of AuNWs was examined at the latter, laboratory scale machine.

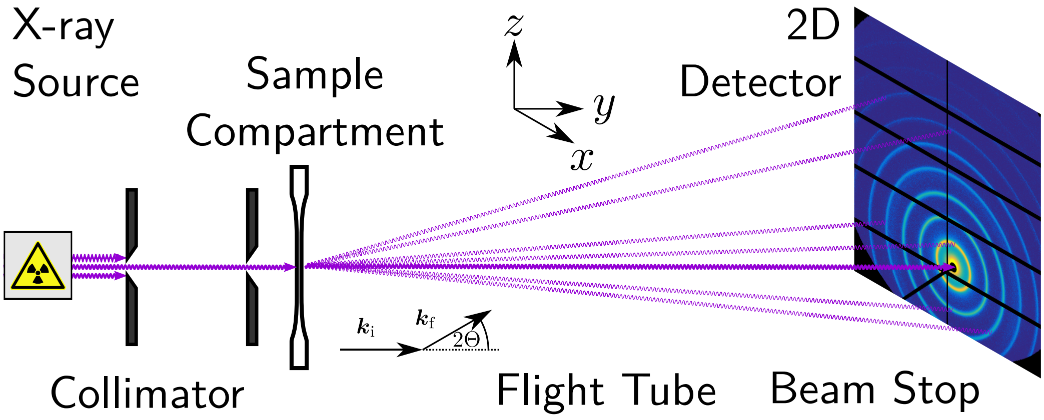

Figure 1.8.: Sketch of a typical SAXS setup: After collimation by at least two apertures, the X-ray beam hits the sample. The scattered radiation pattern is detected on a 2D detector. The collimation system and flight tube are in a vacuum. Windows shield the vacuum from the air at the sample compartment and the detector position. The transmitted beam is blocked by a beam stop, which contains a counting PIN-diode.

Despite the diversity of SAXS-instruments used in this research, the fundamental setup can be sketched as in fig. 1.8. The X-ray source generates monochromatic X-ray radiation, often with minuscule divergence. The actual radiation source, i.e. for a synchrotron the insertion device and for the XEUSS 2.0 the copper anode, usually produces a broad spectrum of wavelengths. The source therefore includes a monochromator to select a single wavelength, for synchrotrons the wavelength can be tuned over a broad spectrum. In the “GeniX 3D Cu Ultra Low Divergence” source used in the XEUSS 2.0 laboratory system, a bent multilayer mirror selects the Cu-K_α line at $\lambda = 0.154\,\mathrm{nm}$ and collimates the radiation.

The monochromatic beam is defined and parallelised in the collimation system. It consists of at least two apertures to define a parallel beam with controlled size. In the systems employed here, the apertures were rectangles defined by movable slits. Their motility allows fine tuning of the beam cross section tailored for the specific application.

The beam path is evacuated as far as possible to reduce X-ray absorption and scattering by air. For this research, the collimation system and the flight path after the sample were evacuated. A short sample compartment was separated by thin X-ray windows to allow easier access. The additional scattering due to the windows and the air gap was sufficiently small for all purposes. Often, SAXS samples are contained in thin-walled glass capillaries. A feature of the research presented here is the use of a flow-through capillary. In addition to the ability to examine flowing samples, this further allows to exchange the sample without changing or moving the sample container, which facilitates quantitative comparisons between samples.

The transmitted and scattered radiation passes through a flight tube before it is recorded at the detector. Longer flight paths enable access to smaller angles, while larger scattering angles diverge far from the centre at long distances. Detectors usually have a finite accessible area. To be able to tune the observed angular range, the distance between sample and detector can be changed in most setups. For the systems at ESRF and SOLEIL, the CCD detector is placed on a motorized stage inside the vacuum of the flight tube. The systems at PETRA III and the XEUSS 2.0 use a variable length flight tube, with a PILATUS 1M hybrid pixel detector placed behind a vacuum window.

Modern SAXS instruments employ position-sensitive area X-ray detectors to capture a large portion of the scattering pattern in a single measurement, simplifying studies of time-dependant phenomena or anisotropic samples. To prevent parasitic scattering from the window in front of the detector and overflowing detector counters or even detector damage by radiation overdose, the direct beam is blocked by a beam stop. In the studies presented here, the beam stop incorporates a PIN-diode[16] to measure the intensity of the transmitted beam.

The wave vector of the incident beam $\boldsymbol{k}_\mathrm{i}$ points in y-direction and has a magnitude of $|\boldsymbol{k}_\mathrm{i}| = \frac{2\pi}{\lambda}$ (see fig. 1.8). For a elastically scattered photon, only the direction changes and its wavevector $\boldsymbol{k}_\mathrm{f}$ has the same magnitude. The scattering vector $\boldsymbol{q} = \boldsymbol{k}_\mathrm{f} - \boldsymbol{k}_\mathrm{i}$ has the magnitude

$$q = \frac{4\pi}{\lambda} \sin\Theta \tag{1.16}$$

and is a measure for the momentum transfer on the scattering electrons. In SAXS intensity profiles it is typically used as the x-axis to factor out the dependency of the intensity on geometrical factors and wavelength. The intensity pattern from the same sample on different instruments is ideally the same when measured at the q-scale.

The scattering amplitude pattern $A(\boldsymbol{q})$ of a coherently illuminated sample corresponds to the Fourier transform of the scattering structure[17] [76, p. 516]. In a microscope the objective lens performs an inverse Fourier transform of the scattered radiation field and projects a real space image of the object [77, p. 385]. In a scat-

---

[16] A positive intrinsic negative-diode (PIN-diode) is a fast, low-noise 0D X-ray detector.

[17] Strictly this is only a first order estimate, the so-called Born approximation. If the sample scatters only weak, as in the case of SAXS, only single scattering events and no multiple scattering events occur and the Born approximation is sufficient.

tering experiment the scattered pattern is recorded directly without a lens[18]. The X-rays are scattered on electron density fluctuations of the sample (a sample with homogeneous electron density does not produce scattering beyond the zero angle), with the position dependant electron density $\rho\left(\boldsymbol{r}\right)$ the scattering amplitude pattern $A(\boldsymbol{q})$ can be written as

$$A(\boldsymbol{q}) = \int_V \rho\left(\boldsymbol{r}\right) e^{-i\boldsymbol{qr}} \cdot dV. \tag{1.17}$$

Most detectors only measure the intensity $I(\boldsymbol{q})$, which corresponds to the absolute square of the amplitude, while the Fourier transform phase is lost. Utilizing the electron density autocorrelation function $\tilde{\rho}^2\left(\boldsymbol{r}\right)$ it can be written as

$$I(\boldsymbol{q}) = \int_V \tilde{\rho}^2\left(\boldsymbol{r}\right) e^{-i\boldsymbol{qr}} \cdot dV. \tag{1.18}$$

Since the magnitude of the Fourier components depends on $\boldsymbol{qr}$, this also explains why smaller structures scatter to larger scattering angles. The loss of phase information inhibits a direct inverse numerical Fourier transform to obtain the real space structure and makes detailed data interpretation challenging. Analysing a sample by SAXS can be divided in three major steps, described in the following.

1.3.2.1. Sample Preparation and Data Collection

The requirements on sample preparation are small compared to techniques like electron microscopy. Colloids can be measured in dispersion or dried and many reactors can be adapted to enable in-situ studies with SAXS. Typical samples used in this research can be measured without any pretreatment. The beam also covers a large volume compared to the dimensions of colloids, which means that many particles are probed at once and the results are statistically a good representation. To collect SAXS data, the sample-to-detector-distance should be selected based on an estimation on the involved length scales in the sample. For the conversion of the real space detector signal to the q-scale intensity signal, the sample-to-detector-distance and beam centre coordinates should be measured by using a calibration sample with a well known scattering pattern. Silver behenate, which has regular rings in the typical SAXS regime [78] (shown in fig. 1.8), was used here. The integration time is selected based on signal-to-noise ratio considerations. For colloids dispersed in liquids, a background measurement with the solvent should be performed to account for all other scattering sources except the colloidal sample. The flow-cell

---

[18] In most materials, the absorption of X-rays outweighs refractive effects. Constructing an X-ray lens to build an X-ray microscope is therefore not straightforward.

based approach chosen here allows to measure background and sample patterns at exactly the same position, which is important for correct background subtraction, not disturbed by thickness variations. In this study, the transmitted intensity was recorded on the fly with a PIN-diode in the beam stop.

1.3.2.2. Data Corrections

Data correction has to be performed to obtain data suitable for interpretation. The steps are sketched in fig. 1.9. Isotropic samples produce isotropic scattering patterns around the origin. The 2D detector images are usually integrated and converted to q-scale. Detector inhomogeneities and non-linearities should be corrected during this step[19]. Shadowed and non-sensitive detector regions are masked prior to integration with a tailor-made mask. In this research, the Python based tool "pyFAI"[79] was used for calibration and image integration[20]. For a background measurement and a sample measurement, this results in the profiles $I_{\mathrm{BG}}(q)$ and $I_{\mathrm{S+BG}}(q)$, with the respective transmitted intensities T_{BG} and $T_{\mathrm{S+BG}}$ measured at the beam stop.

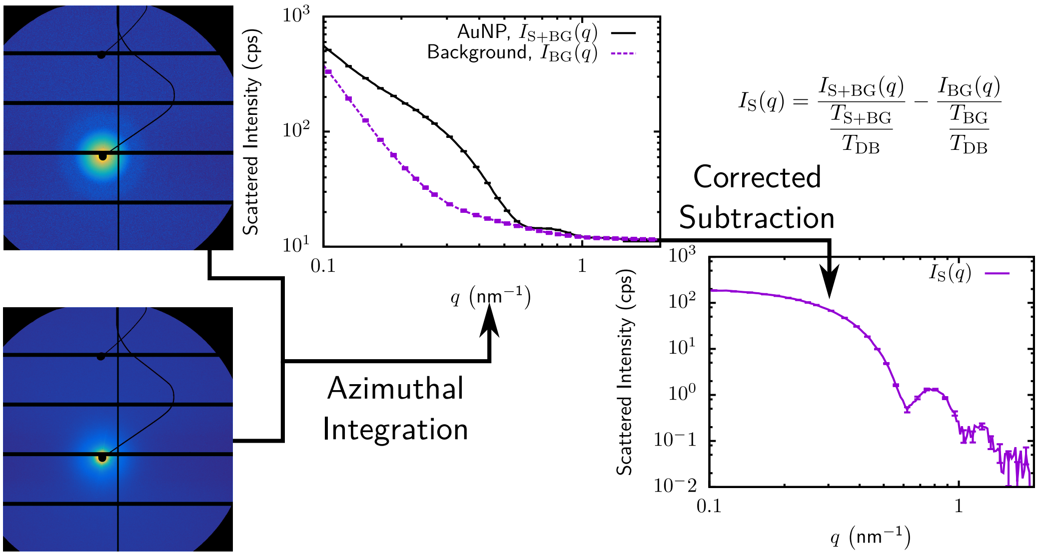

Figure 1.9.: Sketch of the data correction work flow.

To account for potentially different integration times, all count rates are converted to counts per seconds (cps) in the following. These intensity values were not

---

[19] Modern data collection software corrects for most detector related errors before saving the image.

[20] Large number of raw data files (> 10000) from different sources had to be processed. The scripting capabilities and flexible input of "pyFAI" allowed this.

converted to an absolute intensity scale, because in this study only relative changes are considered. If the signal magnitude is compared between different datasets, the normalisation was chosen to allow direct comparison.

X-ray detectors generally produce a signal even when the beam is off. For all data presented here, this dark count rate was found to be negligible compared to the actual signal. No dark count rate correction was performed. The polarisation of the incident beam influences the scattering pattern. For SAXS the effects are typically small [80], so they are not corrected here.

The solvent around the sample scatters less than the pure solvent used during the background measurement because the dispersed sample absorbs a certain amount of radiation. To correctly subtract the background and exclusively obtain the scattering signal of the sample $I_\mathrm{S}(q)$, the different transmissions weighted with the transmitted "direct beam" intensity measured without any capillary T_DB have to be considered:

$$I_\mathrm{S}(q) = \frac{I_\mathrm{S+BG}(q)}{\frac{T_\mathrm{S+BG}}{T_\mathrm{DB}}} - \frac{I_\mathrm{BG}(q)}{\frac{T_\mathrm{BG}}{T_\mathrm{DB}}}. \tag{1.19}$$

The resulting $I_\mathrm{S}(q)$ shown in fig. 1.9 originates from an aqueous AuNP dispersion and was taken at PETRA III.

1.3.2.3. Data Analysis

Collecting data with the right parameters and doing the proper correction steps can be standardized and is usually tractable. The interpretation of SAXS data is probably the main challenge of the technique due to the inherent loss of phase information (eq. (1.18))[21]. The so-called integral parameters can be deduced from the scattering curve without assuming any model for the scatterers. For monodisperse and dilute non-agglomerated particles, the radius of gyration R_g can be estimated by the Guinier approximation [81].

This study is focussed on aggregation of particles, thus the Guinier approximation can only be used in limited cases. Another model-independent method to estimate particle size is the pair distance distribution function $p(r)$. It is determined from the scattering pattern by an indirect Fourier transform and allows calculation of a mean radius of gyration [82, 83].

Due to the close relation between scattering and electron density, the integral of the intensity in reciprocal space

$$Q = \int I(q) q^2 \mathrm{d}q \tag{1.20}$$

---

[21] A well known consequence is that for dispersed samples, size polydispersity can not be distinguished from shape polydispersity [73, p. 35].

is proportional to the mean square of electron density fluctuations [72, p. 22]. Therefore the so-called scattering invariant Q does not change under structural rearrangements of the sample, as long as the composition does not change. The limits of the integral should be chosen to cover the complete SAXS regime. In the context of this work, Q should remain unchanged between dispersed and agglomerated NPs, as long as the volume fraction remains unchanged.

To further analyse SAXS patterns, it is necessary to use models based on certain assumptions about the sample. It is useful to define a form factor $P\left(q\right)$, which describes the scattered intensity of a single particle[22]. The scattering signal of a dilute particle dispersion is then proportional to the single particle form factor, which becomes accessible by measurement in this way. Analytical form factors for many particle shapes are available [84]. Here possible modelling approaches for spherical particles will be discussed. The form factor for a single spherical particle with radius R was already calculated by Lord Rayleigh [85] and can be expressed as

$$P\left(q\right) = \left(\Delta\rho\frac{4}{3}\pi R^3\frac{3}{\left(qR\right)^3}\left(\sin\left(qR\right) - qR\cos\left(qR\right)\right)\right)^2. \tag{1.21}$$

$\Delta\rho$ is the scattering length density contrast, which is proportional to the difference between the scattering particle and the surrounding solvent. To convert the measured detector count rate to the absolute intensity scale of the angular dependant differential scattering cross section, this value has to be known and the measurement system has to be calibrated with a known standard, usually ultrapure water. This leads to a calibration constant.

In this research, only relative comparisons between the intensity values will be made, i.e. the magnitude of the intensity is not modelled quantitatively. Across different measurements, the magnitude is not necessarily comparable. When the measurements are explicitly compared, they have been normalised to a common scale beforehand.

The values are not necessarily comparable between the different measurements, when the intensities are compared in the related discussion, they were previously normalised on a common intensity scale.

To determine the size of monodisperse particles without interparticle interactions, it is sufficient to measure the scattering signal of a dilute dispersion and perform a least square fit on the appropriate form factor.

Often the sample can not be described as monodisperse and/or by isolated single scatterers. Interparticle effects can be described by a structure factor $S\left(q\right)$, which can describe interaction in dispersed samples and spatial correlations due to a fixed

---

[22] More precisely the $P\left(q\right) = \langle\left|F\left(\boldsymbol{q}\right)\right|^2\rangle$ that is measured is the orientational average of the square of the form factor amplitude. For simplicity it will be termed form factor in the following.

superstructure. The intensity scattered by monodisperse particles with isotropic interaction potentials can be written as

$$I(q) = P(q) \cdot S(q). \tag{1.22}$$

Polydisperse samples can be described by a size distribution $N(R)$, the scattered intensity for non-interacting particles is then

$$I(q) = \frac{1}{\int N(R)\mathrm{d}R} \int N(R)P(q,R)\mathrm{d}R. \tag{1.23}$$

Assuming a suitable size distribution, the particle size and polydispersity of a dilute dispersion can be determined by performing a least squares fit on this integral. For spherical particles with a Schulz-Zimm distribution [86, 87], an analytical solution of the integral exists [88]. Usually the Schulz-Zimm distribution is sufficient to calculate the mean and standard deviation of a monomodal size distribution. It was implemented in a self-made Python program to obtain the size distribution of spherical nanoparticles from their scattering patterns automatically. The program was used in chapters 2 and 3 to determine particle sizes and polydispersities. The algorithm is described in appendix A.

While eq. (1.22) is an approximation for symmetric interactions independent of particle size, the scattering signal can generally not be factorized accordingly. Several approximations to the problem exist, tailored to specific assumptions [88–90].

Detailed information on the sample structure can be acquired by fitting the right model to the scattering data of a sample. The drawback of model fitting compared to the integral parameters is that certain assumptions on the sample have to be made to choose the right form and structure factors and the matching term for combining them. Arbitrarily complex models can be constructed by combining models, and by fitting enough parameters every scattering curve can be fit with high precision. This does not guarantee high accuracy, i.e. the model may be no accurate representation of the sample, even when the scattering data is modelled with high precision. Ideally, a SAXS model is chosen based on independent knowledge about the sample. The number of free parameters during fitting should be kept as low as possible.

1.3.3. Agglomeration Studies in a Flow System

The central idea of this dissertation was to use a millifluidic flow system to prepare and observe nanoparticle agglomerate samples. It permitted the observation of a steady state of agglomeration during the transient formation of nanoparticle agglomeration using different analytical methods with arbitrary integration times

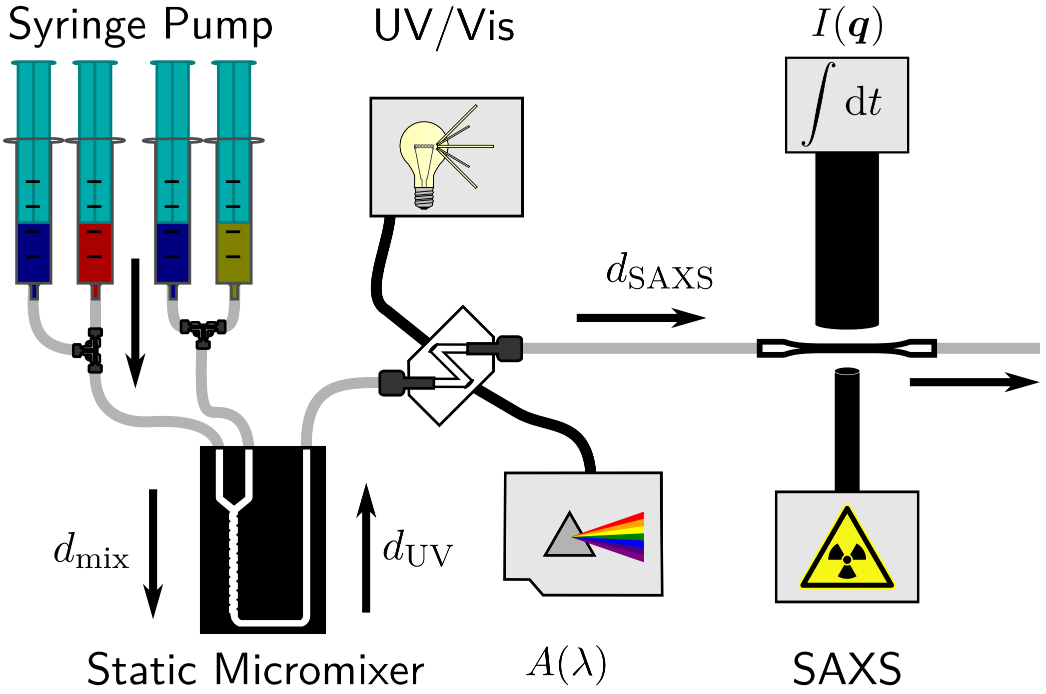

Figure 1.10.: Principle schematic of the flow system.

and under precisely controlled reaction conditions. The principle is sketched in fig. 1.10.

The system was designed as a modular setup, all components were connected with standard HPLC tubing (∼ 0.8 mm diameter, fluorinated ethylene propylene (FEP) for extensive solvent compatibility) and can partially be replaced by alternative units. A cetoni “NEMESYS” syringe pump created flows of up to four independent substances. The flow of a single channel was pulsation free in the range of $10\,\mathrm{nL\,min^{-1}}$ to $300\,\mathrm{\mu L\,s^{-1}}$, the individual flow rates were controlled by a software. The different channels were merged in a static micromixer, different modules were used for this (see section 1.3.3.1). Typically a colloidal dispersion was mixed with another solvent. The mixture was transported downstream by a continuous flow of fresh material and passed consecutively through the UV/Vis and SAXS flow cells.

The relative concentrations of the influent substances were precisely controlled by tuning their relative flow rates (the concentration errors due to the flow system alone are usually well below 1 %). After passing the mixing stage with length d_{mix}, the sample was ideally homogeneous with a uniform concentration. If mixing the substances triggered a reaction in the sample, which means in this research often that colloidal agglomeration was induced by addition of a destabilising agent, the reaction began during or after the mixing stage.

It progressed while the reacting sample (e.g. the growing agglomerates) was advected in the flow field. After flowing across a certain distance d (and the associated reaction time), the sample flowed through the detector. For constant flow velocity during a measurement, the sample at the detector position had the same persistence time (or age) during the whole measurement. For increased flow velocities, the observed sample underwent shorter reaction times. By this method, the age of the observed agglomerates could be tuned.

In this way, the problem of temporal resolution of the reaction kinetic is transformed to the problem of spatial resolution inside the channel. Finite channel dimensions and detection volumes have to be considered when interpreting the spatially resolved data in terms of reaction times (see also section 1.3.3.2). In principle, though, the flow processing method decouples the reaction time scale from the integration time scale.

Therefore the integration times are only limited by the available sample volume at the pump, in contrast to a batch experiment where the reaction time scale generally limits the possible integration time to short intervals. With the flow processing method, the study of the kinetics of fast reaction becomes possible even for slow detection methods, e.g. laboratory scale SAXS.

Furthermore, even a synchrotron SAXS experiment can benefit from the flow processing method. While the intensity is often sufficient to study fast kinetics even in a batch experiment, the high energy density in a synchrotron X-ray beam can damage the sample. This effect is alleviated in the flow system, because the sample is continuously replaced.

Compared to stopped flow systems, the necessary amount of sample is larger. Vice versa, the continuous production of agglomerates would allow to integrate the system devised here into further processing steps, necessary for applications, e.g. surface deposition of agglomerates, in a straightforward way.

1.3.3.1. Static Micromixer

The mixing of two miscible fluids entering a channel depends strongly on the relative importance of inertia and viscous forces. The ratio between inertial and viscous forces is the Reynolds number Re. If a fluid with kinematic viscosity ν and area averaged flow velocity v flows in a cylindrical channel with inner radius R, the Reynolds number is [91, p. 174]

$$\mathrm{Re} = \frac{2v \cdot R}{\nu}. \tag{1.24}$$

If a fluid flow is dominated by viscous forces and inertial effects can be neglected (small Re), a stable steady flow field without turbulence, often termed laminar flow, forms [92, p. 214]. A typical value in this research was Re ~ 10, which is well below the critical $\mathrm{Re}_{\mathrm{crit}} \sim 2300$ for the onset of turbulence in a pipe flow [92, p. 186]. In this regime, the velocity profile for a pressure driven flow of a viscous fluid in a channel with circular cross section with radius R (Poiseuille profile), is rotationally symmetric around the centre and has a parabolic dependence on the radial position:

$$v(r) = 2\overline{v}\left(1 - \left(\frac{r}{R}\right)^2\right). \tag{1.25}$$

The mean flow velocity for a given channel radius R can be calculated from the volume flow rate $\dot{V}$ via

$$\overline{v} = \frac{\dot{V}}{\pi R^2}. \tag{1.26}$$

The volume flow rate $\dot{V}$ in the case discussed here is imposed on the system by the syringe pump. The velocity field results in an associated shear rate field,

$$|\dot{\gamma}| = |\frac{\partial v}{\partial r}| = 4\overline{v}\frac{r}{R^2}. \tag{1.27}$$

The shear in the system as a parameter is most important in section 4.4.2. Since the shear depends on the radial position, it is useful to define the area average of the shear,

$$\bar{\dot{\gamma}} = \frac{\int_A \dot{\gamma}(r)\mathrm{d}A}{A} = \frac{8\overline{v}}{3R} = \frac{8\dot{V}}{3\pi R^3}, \tag{1.28}$$

to allow comparisons of shear effects.

In a laminar flow field through a straight channel, the stream lines do not cross and stay parallel. In this case the only mixing mechanism is diffusion perpendicular to the flow direction. The ratio between advective and diffusive transport rates is termed Péclet number Pe. For particles with translational diffusion constant D_{t} that diffuse in a pipe flow with velocity v and pipe radius R, the Péclet number is [93, p. 376]

$$\mathrm{Pe} = \frac{2v \cdot R}{D_{\mathrm{t}}}. \tag{1.29}$$

For the slowly diffusing particles used in this research the Péclet number is Pe $\gtrsim 10^4$. In the large Pe and low Re regime of the colloidal samples in the small channels relevant to this study, convection dominates diffusion, but there is negligible convection perpendicular to the flow direction. Homogeneous mixing of two substances by merging the two incoming flows is thus a challenge [94], especially for relatively slowly diffusing nanoparticles [95].

Proper mixing of the reagents is crucial for all reactions with two reagents including nanoparticle (NP) agglomeration experiments. In a typical experiment, an AuNP dispersion was mixed with an agglomeration agent, e.g. AuNPs dispersed in heptane are destabilized by mixing with equal volumes of polar 1-propanol. Inhomogeneities connote local concentration differences that influence the agglomerate growth and distort the results. Furthermore, most measurement and analysis methods rely on homogeneous samples.

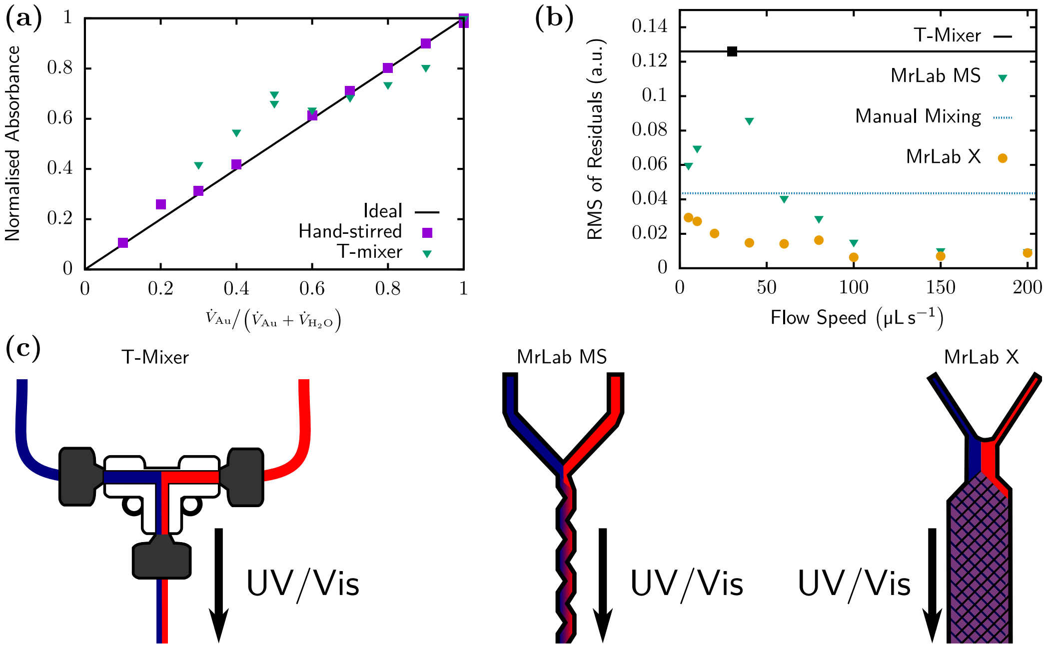

Figure 1.11.: Experiments to characterise mixing efficiency of different mixing modules. (a) Dependence of maximum absorbance on concentration set point for a simple T-mixer, compared to the ideal behaviour and a hand-mixed reference measurement. (b) RMS of the difference between absorbance values for different mixers at different flow velocities and the ideal curve as a measure for inhomogeneities. (c) Sketches of the different mixing modules.

Special care was taken to guarantee sufficiently homogeneous mixing. To characterise the mixing capabilities of different mixing modules, UV/Vis spectroscopy on aqueous AuNP concentration series (by diluting the original solution with ultrapure water in the flow system) were performed. The concentration axis in fig. 1.11 (a) is normalised to the concentration of the pure dispersion. The UV/Vis flow cell was connected directly after the mixing element, with a minimised delay length in between ($< 10\,\mathrm{cm}$).

The absorbance $A(\lambda)$ of a homogeneous, dilute dispersion depends linearly on the concentration of the dispersed species c (see eq. (1.14)). This is not true for inhomogeneous distributions of the dispersed phase in the continuous phase, especially since the illumination is often not covering the complete sample homogeneously. This was exploited to judge the mixing capabilities of different mixing modules: If nonlinear concentration dependence of the absorbance was found, it was attributed to incomplete mixing.

The dependency of the absorbance at the localized surface plasmon resonance at $529.6\,\mathrm{nm}$ on the concentration set point is compared to the ideal straight line in fig. 1.11 (a). The set point is determined by the flow velocity fraction of the influent AuNP dispersion. While the total flow velocity was kept unchanged, the water content was varied. The resulting concentration set point is accurate, the maximum deviation for the flow velocities considered here is below $1\,\%$. The straight line represents the expected linear curve, the purple squares are reference measurements, were hand-stirred solutions were injected in the flow cell. The absorbance values were normalised with the value for the pure dispersion ($c = \dot{V}_{\mathrm{Au}} / \left(\dot{V}_{\mathrm{Au}} + \dot{V}_{\mathrm{H_2O}}\right) = 1$) to eliminate batch-to-batch variations of the initial concentration.

Figure 1.11 (a) illustrates that the in-situ mixed solutions did not show linear dependence of absorbance on the set concentration. The premixed samples are noticeably closer to the ideal curve than the samples mixed in-situ. It was concluded that the mixing efficiency of the T-mixer is insufficient for the needs of this research. This result is consistent with a rough estimation of the transport behaviour. The Reynolds numbers are well below the critical number for the onset of turbulence, $\mathrm{Re} \sim 50 < 2300$. This means that diffusion perpendicular to the stream lines is the main mixing mechanism. The comparatively large Péclet number, $\mathrm{Pe} \gtrsim 10^4$, implies that a long flow path is required for homogeneous mixing to take place and inhomogeneities are expected directly after the mixer element.

To simplify comparisons the root mean square of the difference between the N measured absorbance values A_i at the concentration c_i from the corresponding value of the ideal curve $R(c_i)$

$$\mathrm{RMS} = \sqrt{\frac{1}{N} \sum_{i=1}^{N} \left(A_i - R\left(c_i\right)\right)^2} \tag{1.30}$$

is defined as a measure for nonlinearity. A smaller value corresponds to more homogeneous mixing. The values for the T-mixer and the premixed samples are represented as lines in fig. 1.11 (b).

A number of different specialized static micromixers is available [96]. Borosilicate glass static mixing elements, “MR-Lab MS” and “MR-Lab MX” from “Little Things

Factory GmbH", were chosen here to accelerate mixing while offering good chemical compatibility[23] (see fig. 1.11 (c) for sketches of the structures). The RMS values in fig. 1.11 (b) indicate that while the mixing efficiency is on par at higher flow velocities, the MR-Lab MX shows superior mixing at lower flow velocities.

Applying shear to a destabilised dispersion is known to enhance agglomeration, because it enhances the diffusive transport [40, p. 289]. The biggest influence of shear is expected during the relatively short residence time in the mixing module, where it is needed to provide homogeneous mixing. To assess the influence of shear on the agglomeration taking place during the laminar flow in the delay lines (d_{UV} and d_{SAXS} in fig. 1.10), it useful to compare the Smoluchokwski rate constants (see section 1.2.3.1) for diffusion- (k_{diff}) and shear-induced transport (k_{shear})[24]. Their ratio can be expressed as

$$\frac{k_{\mathrm{shear}}}{k_{\mathrm{diff}}} = \frac{4\gamma\eta R^3}{k_{\mathrm{B}}T}, \tag{1.31}$$

to assess the relative importance of effects [38, p. 167]. With a typical shear of $\gamma = 1500\,\mathrm{s}^{-1}$ (section 4.4.2), dynamic viscosity of $\eta = 1\,\mathrm{mPa\,s}$, minimum size of $R = 3\,\mathrm{nm}$ and minimum temperature of $T = 293.15\,\mathrm{K}$, the resulting ratio is $< 10^{-4}$. For the agglomerate radii achieved in chapters 2 and 3 it never exceeds unity. *A significant influence of shear on the progressing agglomeration in the delay lines is therefore not expected.*

1.3.3.2. Different Distributions

A hydrodynamic effect prevents straightforward calculation of the relevant agglomerate age, even when the flow velocity and delay line length are precisely known. "Taylor Dispersion" is usually used to denominate the band broadening of a sample plug transported in a flow field [97], as sketched in fig. 1.12 (a). Additionally, the case of miscible solvent displacement (fig. 1.12 (b)) in a cylindrical tube is considered in the seminal paper of Taylor [98]. The result is that for cases where the diffusion of the replacing substance can be neglected relative to the advective transport in the flow field, the front of the replacing liquid is broadened due to the shear field (eq. (1.25)), analogue to the widening of a plug in the same flow field.

On the one hand, this implies that it takes a certain equilibration time until the major portion of the displacing liquid arrives at a downstream position, on the other hand it further implicates that fluid volume elements at different radial positions

---

[23] The first module was chosen with large inner diameter to prevent clogging with a simple geometry to limit dead volume (MR-Lab MS). The additional mixer (MR-Lab MX) was later retrofitted for better performance at lower flow velocities.

[24] Purely diffusive transport is often termed perikinetic, shear-induced transport is called orthokinetic.

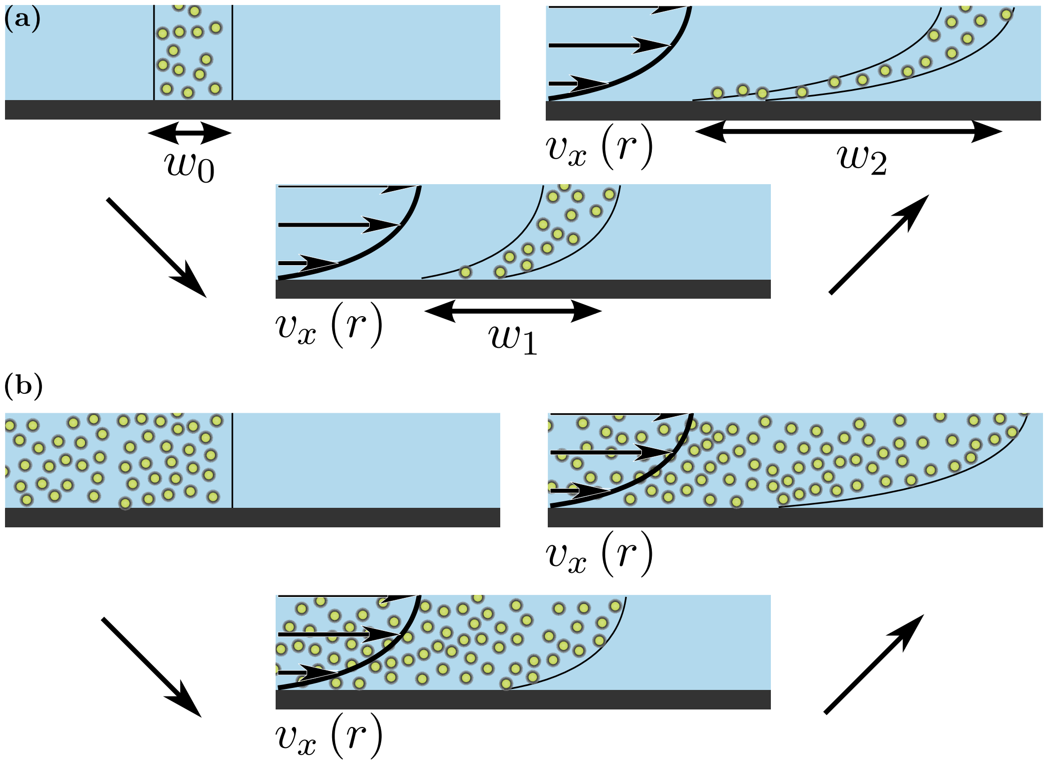

Figure 1.12.: Hydrodynamic dispersion in a cylindrical channel. Because of the cylindrical symmetry, only radial profiles are shown. (a) Sketch of Taylor dispersion: When a sample plug is transported in a pressure driven flow, the shear profile induces a broadening of the width of the plug. The w_i represent the width at the time step i. (b) Hydrodynamic dispersion also play a role when filling an originally solvent-filled tube with a colloidal dispersion. The particle concentration front is broadened while propagating through the channel.

are advected at different velocities. For a sample in a transient state this means that the sample age at a certain distance from the reaction initiation point depends on the radial position.

The measurements presented here always result from data collected from a finite volume inside the channel and represent therefore inevitably a certain average over a distribution of the time of reaction. Together with the nanoparticle size distribution and statistical fluctuations of the number of particles in a single agglomerate, *the sample actually measured at the detector positions a convolution of several distributions.*

1.3.3.3. Fouling

Wall fouling was already a major concern during planning of this research. It is foreseeable that when destabilising a particle dispersion, the particles will not only adhere to each other, but also to the inner walls of the system. This influenced several design decisions.

Compared to microfluidic chips, the dead volume of the mixing elements used in this research is comparatively large. While this introduces unfavourable delays, it helps to avoid clogging of the channels with accumulating particles or large agglomerates.

It is common practice to rinse glassware used for AuNP synthesis or processing with aqua regia [99]. The materials of the system were chosen to be able to withstand flushing with aqua regia. This way, as soon as contamination inside the system became obvious, it could be flushed with aqua regia to ensure that AuNP residues were removed.

Aqua regia is highly corrosive and releases toxic gases during dissolution of metals and should therefore be handled in a fume hood. To be able to remove gold contaminations without disassembling the setup, an aqueous solution of potassium iodide and iodine was used as an alternative, less dangerous gold etchant [100] (see also section 2.2.6).

Despite thorough cleaning, the results presented in the following chapters revealed that fouling remained a major issue.

2. Agglomeration of Aqueous Gold Nanoparticles

2.1. Introduction

The agglomeration process of aqueous gold nanoparticles is not only interesting from a fundamental point of view, but it is also exploited in colorimetric assays for the detection of small substance concentrations, ideally directly by eye [101–104]. For these applications, the facile synthesis and modification of the particles is beneficial.

While we discuss the interplay between optical and structural properties with the surface modification and solution properties in this chapter, the focus is not on improving colorimetric detection schemes. The main purpose of the studies performed in this chapter is to demonstrate the suitability of the flow-based approach for agglomeration studies.

The advantage of using aqueous AuNPs as a model system to show the capabilities of the flow setup is that they are easy to produce and water as a solvent is easy to handle.

Classical methods to induce agglomeration of charge-stabilised aqueous colloidal particles include agents that change the surface charge directly, by changing the pH or replacing the charged surface groups, or reduce the repulsive forces by reducing the screening length by increasing the ionic strength. In both cases, the van der Waals attraction of the gold cores can overcome the electrostatic repulsion above a certain threshold concentration of the agglomeration agent. Typical examples include pyridine, which displaces charged surface groups, or sodium chloride, which screens the surface charges [39]. A dispersion of citrate-stabilised gold colloids can be destabilised by hydrochloric acid [105].

HCl was used to induce AuNP agglomeration in this research. It both reduces the negative surface charge (by lowering the pH and therefore protonating the charged citrate groups) and screens the remaining charges due to the ionic strength. Both effects individually have sufficient magnitude to destabilise the dispersions in the concentration range probed here.

It was found that the substance concentrations can be reliably tuned, while the resulting steady states of agglomeration at an adjustable agglomerate age can be observed with virtually unlimited integration times. The shapes of the SAXS patterns and UV/Vis spectra were analysed with semi-automatic, purpose-built Python programs to determine relevant structural parameters, like agglomerate size and density. The size after a certain growth time could be increased by increasing the hydrochloric acid concentration. The effectiveness of different stabilising molecules is assessed.

The experiments exposed some issues of the flow approach:

- Particle adsorption on the system walls interfered with the measurements.
- Only mean values over a certain range of agglomerate ages could be analysed due to the hydrodynamic dispersion.

The main results of the measurements were:

- HCl-induced agglomeration was faster for higher acid concentrations.
- The kinetics during the early stage of agglomeration were found to deviate from the classical limiting cases of DLA/RLA.
- Particle surface modification with MUTEG prevented agglomeration in high acid concentrations.

2.2. Methods

A flow system with syringe pumps, mixing elements, UV/Vis module and a flow-through capillary for SAXS (see also fig. 1.10) was set up at the MiNaXS beamline of the PETRA III synchrotron [106]. A photo of the arrangement is shown in fig. 2.1. The principle setup is sketched in fig. 1.10.

Seven aliquots of the AuNPs were successively filtered and used without dilution. Due to the uncontrollable adsorption on the filtering membrane, the concentration between the seven particle batches slightly varied.

For the agglomeration experiments, the AuNP dispersion was mixed with dilute HCl dispersions of different concentrations. The "MR-Lab MS" (see section 1.3.3.1) was used for all measurements presented in this chapter. The resulting HCl mass fraction was in the range of $w \in [0.025\,\%, 0.1825\,\%]$ ($c \in \left[7\,\mathrm{mmol\,L^{-1}}, 50\,\mathrm{mmol\,L^{-1}}\right]$, corresponding to pH values from 1.3 to 2.2)[1].

---

[1] Empirical data [107] was fit with a cubic function, $c \cdot \mathrm{L\,mmol^{-1}} = -2.3 \cdot 10^{-5} + 0.27382 \cdot w + 1.3 \cdot 10^{-3} \cdot w^2 + 1.3 \cdot 10^{-5} \cdot w^3$, to extrapolate the reported values towards smaller mass fractions. The concentration of the stock solution was determined by titration with KOH.

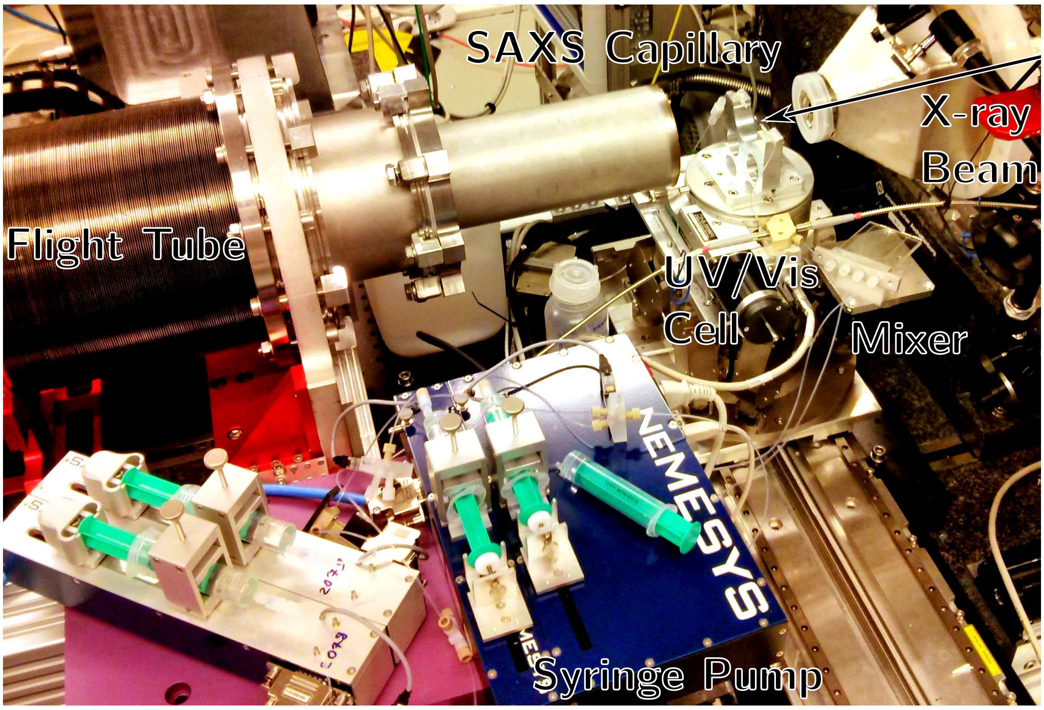

Figure 2.1.: Photo of the setup at the MiNaXS beamline of the PETRA III synchrotron.

2.2.1. Particles

The particles used for this study were synthesised following a protocol adapted from Frens [15]. In the first synthesis 72 mg of $HAuCl_4$ were dissolved in 800 mL of water. The solution was constantly heated and stirred to boiling. 280 mg of sodium citrate, dissolved in 28 mL of water, were added to the boiling solution. While the solution boiled for 30 min, the gold was reduced and dispersed particles formed, indicated by the red colour of the dispersion. The synthesis yields gold particles, charge-stabilised by citrate ions adsorbed on the surface, with gold concentrations around $50\,\mathrm{mg\,L^{-1}}$.

Prior to the experiments, seven aliquots of a single synthesis batch were filtered with a 0.2 µm regenerated cellulose syringe filter. In the following they are labelled "batch 1–7".

In a separate synthesis, the ratio of $HAuCl_4$ and sodium citrate was changed to obtain a different core size. The new amount of $HAuCl_4$ was adjusted to 81 mg and 316 mg of sodium citrate were used.

For additional experiments, the citrate ligands of a part of this second synthesis were exchanged to (11-mercaptoundecyl)tetra(ethylene glycol) (termed “MUTEG” in the following) and poly(ethylene glycol) methyl ether thiol with a number average molar mass $M_n = 800\,\mathrm{Da}$ (termed PEG in the following) similar to the method described in [108].

349 µL of a $10\,\mathrm{g\,L^{-1}}$ aqueous solution of MUTEG and 733 µL of a $10\,\mathrm{g\,L^{-1}}$ aqueous solution of PEG were added to 150 mL of the as-synthesised particle dispersion[2]. After stirring $\sim 1\,\mathrm{h}$ the covalent bond between the ligands' thiol group and the gold surface was expected to be completed and the excess ligand was removed by fivefold centrifugal filtration and successive redispersion in ultrapure water.

The measurements are labelled “batch 8” for the as-synthesised particles, “batch 9” for the MUTEG- and “batch 10” for the PEG-modified particles.

2.2.2. SAXS

The main method to characterise agglomerate and particle sizes in this study is small-angle X-ray scattering (SAXS).

2.2.2.1. Instrumentation

The X-rays were generated by an undulator source in the PETRA III storage ring, an energy of 11.4 keV ($\lambda = 0.109\,\mathrm{nm}$) was selected with a large-offset Si(111) double crystal monochromator. Beryllium compound refractive lenses were used to focus the beam. The sample to detector distance was set to 2.09 m, as determined by calibration measurements with silver behenate. A photon counting PILATUS3 1M hybrid pixel detector (pixel size $172\,\mathrm{\mu m} \times 172\,\mathrm{\mu m}$) was used to record SAXS patterns with an integration time of 2 s, chosen as a compromise between time resolution and good counting statistics. The transmitted intensity was recorded with a PIN-diode in the 5.5 mm diameter beam stop.

2.2.2.2. Data Evaluation

The azimuthally integrated SAXS patterns (see fig. 1.9) were assigned to the corresponding set of preset concentration and velocity values and averaged accordingly. Data correction was performed according to section 1.3.2.2, i.e. transmission corrected background transmission was performed for all measurements.

The size of the primary particles was evaluated by fitting a form factor for polydisperse spheres to the data of the stable particle dispersions, following the algorithm described in appendix A.

---

[2] The quantities correspond approximately to a twentyfold excess of ligand over the available surface sites.

The radius of gyration R_g describes the mass distribution of an object around its centre of gravity, conceptually directly related to the mass moment of inertia known from the dynamics of rotating masses. When the scatterer is decomposed in infinitesimally small point masses dm and x denotes the distance of the infinitesimal fragment from the scatterer's centre of mass, the radius of gyration is determined by

$$R_\mathrm{g} = \sqrt{\frac{\int x^2 \mathrm{d}m}{\int \mathrm{d}m}}. \tag{2.1}$$

In the case of SAXS, the mass density is represented by the associated electron density [72, p. 25].

The mean radius of gyration R_g was calculated with the *datgnom* tool from the *ATSAS* program package [109]. An indirect Fourier transform algorithm is used to invert the scattering pattern $I(q)$ and calculate the pair distance distribution function $p(r)$. It describes the probability $p(r)$ to find an electron pair separated by the distance r inside the scattering sample [72, p. 168]. It can therefore be used to define a size measure. An estimation of the radius of gyration can be calculated by

$$R_\mathrm{g} = \sqrt{\frac{\int_0^{D_\mathrm{max}} p(r) r^2 \mathrm{d}r}{2 \int_0^{D_\mathrm{max}} p(r) \mathrm{d}r}}, \tag{2.2}$$

where D_max denotes the maximum sample dimension [72, p. 133] and is determined by the *datgnom* algorithm.

Generally, the "real space" R_g determined by the indirect transformation is accepted to be more robust against interferences than the "Guinier" radius of gyration [81] determined from the small q slope. Since agglomeration is known to interfere with the Guinier slope, the R_g values reported in this chapter were determined by the indirect Fourier transform method.

2.2.3. UV/Vis

The most prominent feature in the UV/Vis absorbance spectra of AuNPs is their localised surface plasmon peak (see section 1.3.1). In this research, the UV/Vis spectra of steady states of agglomeration are compared to the spectra of the stable dispersions. Generally, agglomerated particles exhibit stronger absorption in the lower energy, red-shifted part of the spectrum compared to their isolated counterparts[3]. Detailed investigations of the size dependence of the UV/Vis spectra of very similar particles have been performed by analytical ultracentrifugation of stable agglomerates by Zook et al. [110] (see fig. 2.2 (a)). Agglomerates of more than two

---

[3] In the simple model explained in section 1.3.1 this can be understood as a shift of the resonance frequency to lower values, because the resonator enlarges.

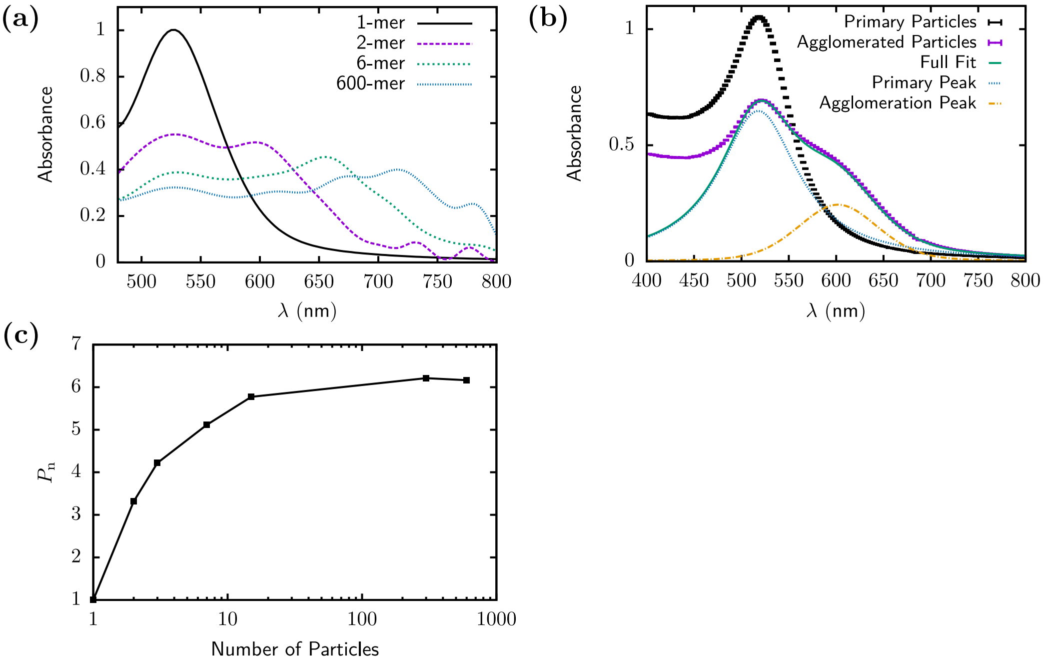

Figure 2.2.: (a) UV/Vis absorbance spectra of AuNP agglomerates with different sizes (interpolated data from [110]). For agglomerates composed of more than two particles, the redshifted part of the spectrum outweighs the original single particle peak. (b) UV/Vis absorbance spectra from this chapter from isolated particles and agglomerates. The agglomerate spectra are fit with a phenomenological double peak model. (c) Normalised flocculation parameters for agglomerates with a defined number of constituents (calculated from the data from [110]).

particles already absorb more in the red-shifted part of the spectrum than in the region of the single particle absorbance. The change in the spectra from hexamers to agglomerates composed of 600 particles is small. Thus, the observation of the red-shifted spectral region is very sensitive to the early stages of agglomeration already, because the dimer spectrum already shows large changes.

The absorbance spectra points in fig. 2.2 (b) represent typical measurements of well-dispersed and agglomerated particles respectively from this chapter. A phenomenological model was used to approximate the agglomerate spectrum and allow extraction of parameters.

The single particle spectra were fit reasonably well with a Pseudo-Voigt peak function. The upturn at lower wavelengths is caused by interband transitions in the core and possible contributions of the ligand molecules [111]. Since the relative importance of these effects is difficult to assess, the asymmetric, lower wavelength part of the spectra was excluded from analysis. A Pseudo-Voigt function $pv(\lambda)$ is a linear combination of a Gaussian and Lorentzian peak function, with identical full width at half maximum (FWHM) w and centre $\lambda_{\max}$, where the amplitude A is weighted with a factor $0 \leq \eta \leq 1$:

$$pv(\lambda) = A\left[(1-\eta)\cdot\exp\left(-\log 2\cdot\left(\frac{\lambda-\lambda_{\max}}{w}\right)^2\right)+\eta\cdot\frac{1}{1+\left(\frac{\lambda-\lambda_{\max}}{w}\right)^2}\right]. \tag{2.3}$$

The function is used in many fields, since it allows good approximation of peaks with various shapes.

The UV/Vis-spectra of the steady states of agglomeration were fit with a phenomenological model: The linear combination of two Pseudo-Voigt peak functions allows to approximate the shape in many cases. This choice is justified by the appearance of the spectra in fig. 2.2 (a). The spectra up to the hexamer mainly appear like two overlapping peaks. Larger agglomerates display a slowly growing redshifted spectral contribution.

The samples observed in this research always represent a superposition of different agglomerate sizes. The poor separation between spectra at different sizes prohibits a separation of measured spectra in the constituent contributions. A simplified model for the full spectrum as drawn in fig. 2.2 (b) was used to allow conclusions on the agglomeration state in the sample: One peak representing the contribution of remaining primary particles and the lower wavelength portion of the dimer spectrum (“Primary Peak”) and a second, redshifted peak accounting for the additional absorbance due to agglomeration (“Agglomeration Peak”) were added to model the measured spectra of agglomerates.

During fitting, the position of the primary peak was constrained to the fitted position from the measurement of the primary particles. The amplitude and the width as well as all parameters describing the agglomeration peak were varied during fitting. The areal fraction of the agglomeration peak on the total area of the peaks is a measure for the progress of the agglomeration process: Larger agglomerates or larger numbers of agglomerates increase the contribution of the agglomeration peak.

An alternative method to describe agglomeration in a UV/Vis spectrum is the flocculation parameter [112]

$$P = \int_{600\,\mathrm{nm}}^{800\,\mathrm{nm}} A(\lambda)\mathrm{d}\lambda. \tag{2.4}$$

The calculation utilises the observation that the single particle absorbance is mainly localised around 520 nm, whereas the agglomerating samples exhibit increased absorbance above 600 nm. Since the particle concentration could change between different experiments, the normalised flocculation parameter

$$P_\mathrm{n} = \frac{P_\mathrm{Agglo}}{P_\mathrm{Part}} \tag{2.5}$$

is used in this work. P_Agglo denotes the flocculation parameter of each agglomerating sample and P_Part the flocculation parameter of the corresponding stable particle dispersion at equal dilution. The increase of the normalised flocculation parameter with the number of particles in an agglomerate, calculated from measurements on agglomerates with defined particle numbers from [110], is plotted in fig. 2.2 (c).

2.2.4. Gradient Measurements

For most experiments, different conditions were scanned during a single measurement run. Either the total flow velocity (corresponding to agglomerate ages) or the fraction of the HCl velocity (corresponding to the concentration of the agglomeration agent) were varied with a programmed syringe pump flow profile. In the first graph of fig. 2.4 (a), the shape of such a profile is illustrated. The AuNP dispersion (from batch 2, see section 2.2.1) was diluted with pure water. The velocity fraction (which is proportional to the volume fraction) of the AuNP dispersion was increased stepwise from 0.2 to 0.8.

Typical results for this gradient are plotted in fig. 2.3. Both the scattering patterns and UV/Vis spectra clearly reflect the concentration steps and a subsequent, washed out concentration increase. After the five concentration jumps, the signals display a certain equilibration time until the final value is approached. The heatmaps illustrate the issue arising from the method employed here: The proper points after the equilibration time have to be selected from a large dataset and assigned to

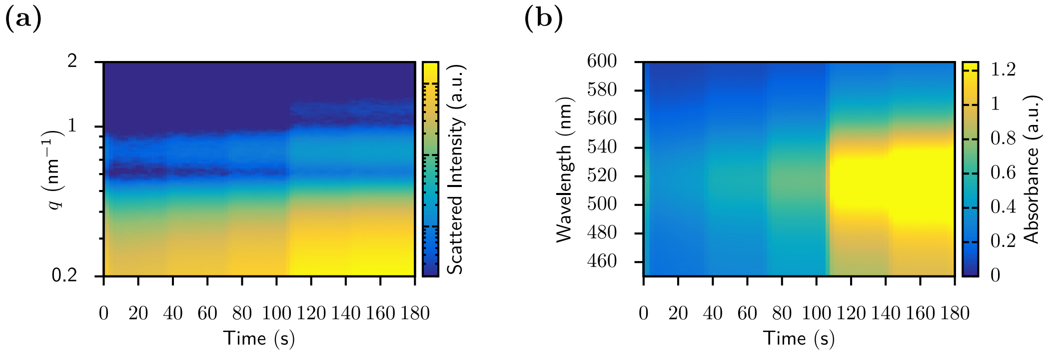

Figure 2.3.: Typical (a) SAXS patterns and (b) UV/Vis spectra acquired for the profile drawn in fig. 2.4 (a).

the respective part of the concentration profile imposed on the system. Due to the finite distance between the detectors, the sample arrives at the UV/Vis cell first, and the SAXS and UV/Vis signals do not share the same time axis.

The scattered intensity/absorbance at a fixed q-value/wavelength (a fixed value on the y-axis of fig. 2.3) is a good indicator for the particular concentration currently seen by the detector[4]. By analysing only one value, analysis is facilitated. The detector signals are aligned according to the jumps in the profiles to allow assignment of certain intervals in the measured data to the corresponding portions of the flow profile (fig. 2.4 (a)).

The blurred profile shape in the detector signals is a clear sign that a certain equilibration time is necessary at every concentration jump due to the hydrodynamic dispersion (see fig. 1.12). Typically, several data points at the end of one interval show little to no variations. These points are averaged and represent the steady state assigned to the agglomeration conditions specified by the assigned section of the flow profile. The data points used for the averages in fig. 2.4 (b) and (c) are labelled with coloured squares in (a). The error bars are not drawn for the sake of clarity. The relative errors were below 10 % for all measurements.

The major portion of the measurements presented in this chapter were made using flow profiles similar to the one presented in fig. 2.4 (a). The relevant values to be averaged and assigned to their respective agglomeration conditions had to be selected from $\sim$ 12000 measured datasets for UV/Vis spectroscopy and SAXS. A Python GUI program was developed specifically to assign valid measurements to the relevant agglomeration conditions and average the files.

---

[4] Other possible values would be fit results of the single data points, integrated intensities or any other value that can be automatically calculated from the measurements. The quantities chosen to evaluate were chosen pragmatically, depending on the type of flow profile used.

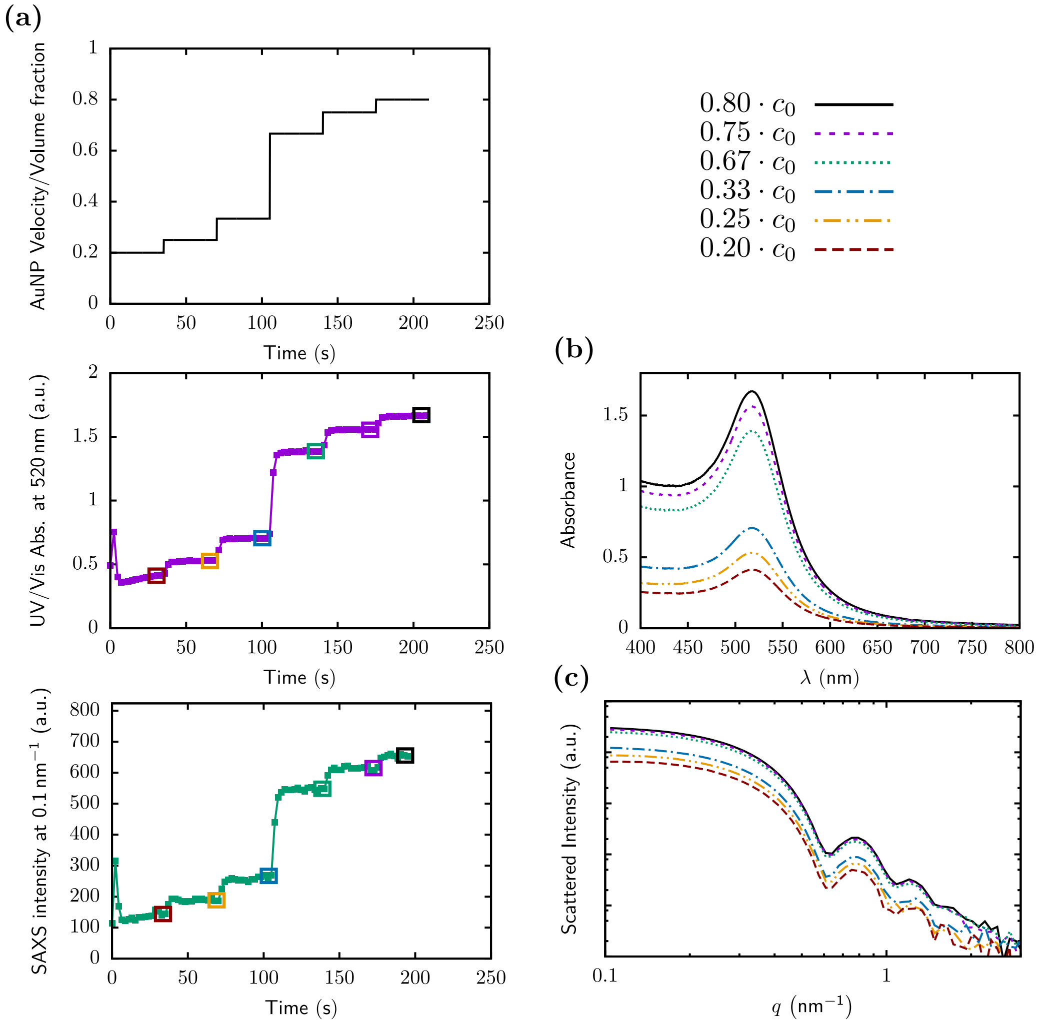

Figure 2.4.: (a) To assign the detector signals to the relevant set point of agglomeration conditions, they are aligned based on the jumps in the concentration profile. Based on the aligned profiles, measurements in steady states are averaged and assigned to the associated concentration values. (b) Averaged UV/Vis absorbance spectra (drawn without offset). (c) Averaged SAXS profiles (drawn without offset). The corresponding data points used for averaging are marked with the rectangles in (a). Error bars are not drawn for better visibility.

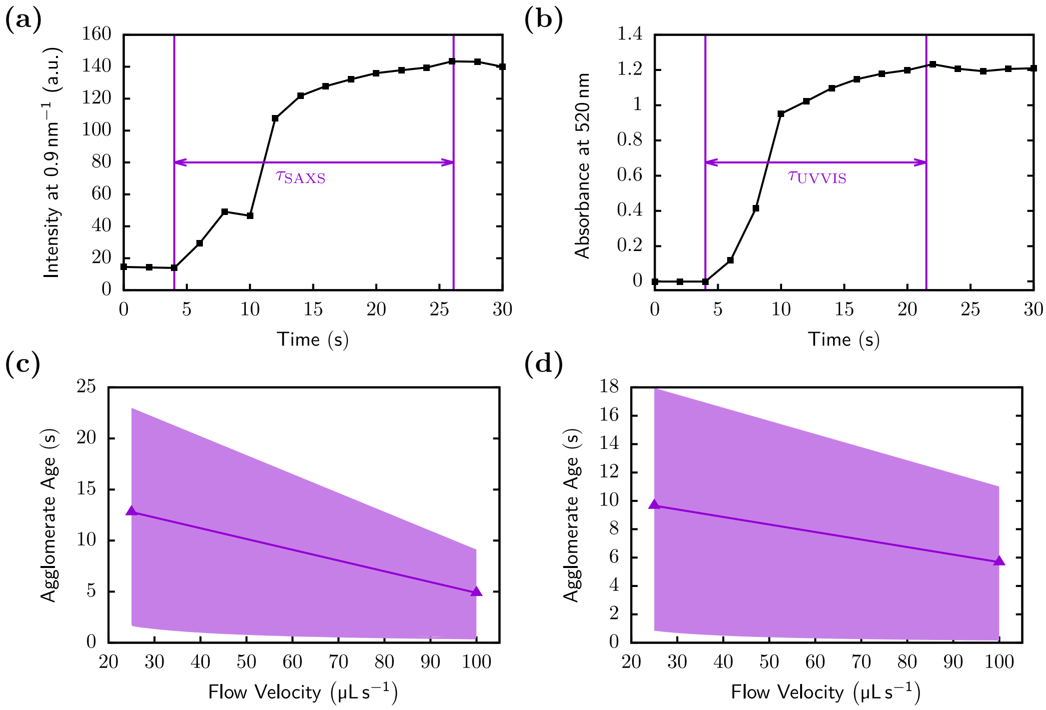

Figure 2.5.: Temporal evolution of the (a) SAXS intensity at $q = 0.9\,\mathrm{nm}^{-1}$ and (b) UV/Vis absorbance at $\lambda = 520\,\mathrm{nm}$. The boundaries for the observed agglomerate age at the (c) SAXS and (d) UV/Vis detector were calculated as discussed in the text and are drawn as translucent area.

2.2.5. Agglomerate Age

The length of the flow path from the mixing point to the UV/Vis detector was approximately 100 mm, the distance from the mixing point to the intersection with the X-ray beam was approximately 190 mm. The parabolic velocity profile prohibits a simple calculation of the reaction time the samples undergo at different speeds. A certain distribution of reaction times is always present in the detected portion of the sample. However, certain boundaries for the observed agglomerate ages can be derived.

A lower boundary for the age is determined by the maximum speed of the velocity profile. It can be calculated from the volume flow and the geometry of the flow path from the mixer to the detectors. The calculated minimum time values for the SAXS and UV/Vis detection positions are represented by the bottom edge of the translucent area in fig. 2.5 (c) and (d) respectively.

An upper boundary is given by the width of the broadened front during a concentration jump (τ in fig. 2.5 (a) and (b) for the SAXS and UV/Vis signals respectively). The concentration jump is generated by flushing the flow system with pure water and consecutively replacing the water with a particle dispersion at the corresponding flow rate. As introduced in section 1.3.3.2, a concentration edge imposed through the inlets of the system is washed out due to hydrodynamic dispersion. The resulting broadened front can be detected by the gradual rise of the scattered X-ray intensity and the absorbance. The temporal width of the front, τ as indicated in fig. 2.5 (a) for SAXS and (b) for UV/Vis signals at a flow rate of $25\,\mu\mathrm{L\,s^{-1}}$, is a measure for the spread in persistence time. The sum of the width τ and the corresponding minimum times therefore represents an upper boundary for the particular persistence time.

According to this conservative estimation, the translucent area plotted in fig. 2.5 (c) and (d) contains the agglomerate age observed at the SAXS and UV/Vis detection points respectively. The triangles represent the average between upper and lower boundary. To simplify calculations, the values for the average agglomerate age reported in this chapter are calculated from the area average of the flow velocity and the flow path length, unless stated otherwise.

2.2.6. Cleaning Procedure

Based on preliminary experiments it was expected that particle adsorption on the detector walls would disturb at least the measurement process (see fig. 2.8). To ensure identical starting points for all experiments a cleaning protocol that intends to remove gold residues adsorbed at the walls was devised.

It is common laboratory practice to remove gold residues from glassware by flushing with concentrated aqua regia. In principle, the flow system withstands filling with aqua regia by design, the potential for accidents due to the corrosiveness of the acid and the toxic fumes demands a safer solution.

An aqueous solution of potassium iodide and iodine serves as a convenient alternative [113]. The triiodide oxidises the gold and the gold ions are dissolved in water. The nanoparticles are expected to dissolve almost instantaneously due to their high surface-to-volume ratio. While it is an effective gold etchant, the potassium iodide/iodine solution is not considered hazardous.

The flushing steps were performed by introducing the solvents with a syringe by hand. To clean the system from residues the protocol was as follows:

- The complete system was flushed with 5 mL to 10 mL pure water.
- The system was flushed with 3 mL of an aqueous solution with $100\,\mathrm{g\,L^{-1}}$ of potassium iodide and $25\,\mathrm{g\,L^{-1}}$ of iodine. It was left undisturbed for approximately five minutes.

- The system was flushed consecutively with 10 mL of pure water, 10 mL ethanol and 10 mL of pure water.

As a last step before the experiment, one of the automatically controlled syringes, containing only water, was used to fill the system with 3 mL of water to ensure consistent water quality during an experimental run.

2.3. Single Particles

Prior to the agglomeration studies presented in the next sections, the original dispersions, batches 1 to 10, were characterised. This way, the change in particle concentration due to filtering and possible other variations can be accounted for in the agglomeration experiments.

2.3.1. Results

The UV/Vis spectra and SAXS patterns for all 10 particle batches were evaluated. Batches 1 to 7 originate from the same synthesis batch, the particle properties, except concentration, were not expected to change. Batches 8 to 10 originate from a separate synthesis batch with adjusted gold-to-citrate ratio, their properties, especially the size, should be different to the other batches.

By fitting the scattering patterns (fig. 2.6 (a)) with the algorithm described in appendix A, the core size of the particles was determined (error bars were smaller than the point size). The core size of the particles from the first synthesis (batch 1 to 7) was found to be 7.2 ± 0.6 nm across all batches. The core size of the second synthesis batch (batch 8 to 10) was consistently determined as 5.2 ± 0.6 nm.

Batch 8 to 10 exhibited excess scattering at small angles compared to the polydisperse sphere model, likely resulting from minor agglomeration.

The surface plasmon peaks of the UV/Vis spectra were well-approximated by a single Pseudo-Voigt peak (fig. 2.6 (b)). For the first synthesis (batch 1 to 7), the spectra looked similar and are represented by the spectrum of batch 4. The peak position was found to be almost identical and its average is $\lambda_{\text{max}} = 517.7 \pm 0.3$ nm. The FWHM of the peaks was almost identical as well, only batch 3 displayed a FWHM that deviates more than 1 % from the average value FWHM = 41 ± 1 nm. The variation in peak height, indicating the concentration changes, was smaller than 2 %. The experimental error bars were smaller than the point size.

Despite being slightly broader ($\lambda_{\text{max}} = 518$ nm, FWHM = 50 nm, smaller height), the citrate-stabilised particle spectrum of batch 8 appeared overall very similar to the the larger particles from batch 1 to 7. Conversely, the modified particles from batch 9 and 10 exhibited a clear shift of the maximum position and peak

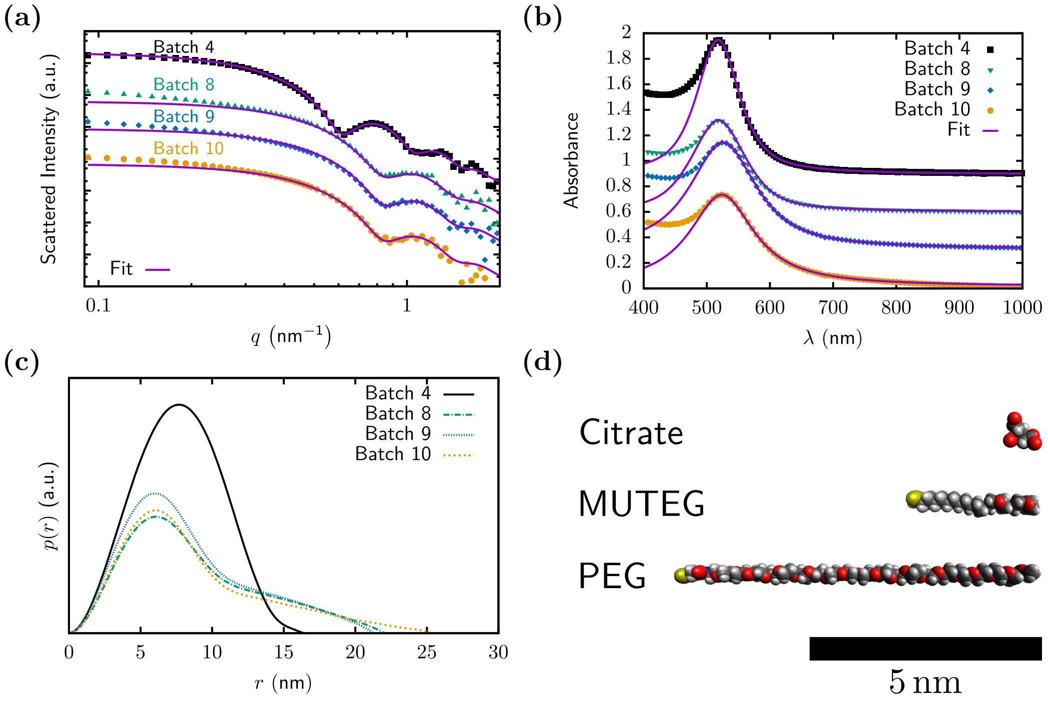

Figure 2.6.: (a) SAXS patterns (offset by a factor of 10) and (b) UV/Vis absorbance spectra (successively elevated by +0.4 beginning from the lowest curve) of the different particle types used in this chapter, including their respective fit functions. (c) Pair distance distribution functions calculated from the scattering patterns. (d) Sketch of the different stabiliser molecules employed in this chapter.

width (batch 9: $\lambda_{\text{max}} = 526\,\text{nm}$, FWHM $= 65\,\text{nm}$; batch 10: $\lambda_{\text{max}} = 524\,\text{nm}$, FWHM $= 63\,\text{nm}$).

2.3.2. Discussion

The SAXS results clearly showed that the syntheses yielded a stable dispersion of monodisperse gold nanoparticles in ultrapure water. The smaller particles from the second synthesis were slightly agglomerated already in aqueous dispersion, as it is evidenced by the low q excess scattering.

The UV/Vis spectra of batch 1–7 and batch 8 appeared similar. The height differed due to the concentration difference and a minor increase in width was found, likely a result of partial agglomeration. The modified particles from batch 9 and 10 exhibited a clear shift in the peak position and width, resulting from their chemical surface modification. Their gold core is responsible for the plasmon resonance that absorbs light. Both the PEG and MUTEG molecules are covalently bound to the surface of the core. They have two effects on the spectroscopic behaviour: On the one hand, the chemical bond introduces new electron states in the metal that can shift the resonance frequency. On the other hand, the dielectric environment of the particles changes due to the replacement of water with the ligand chains [67].

Batches 9 and 10 were modified only on the surface. The significant change in UV/Vis spectra for batches 9 and 10 (compared to the unmodified batch 8) was caused by the changes in local refractive index and the influence of the gold-sulphur bond on the electronic structure of the core. The changes prove that the particles were actually modified compared to batch 8. The SAXS patterns did not significantly change, which rules out particle agglomeration as a possible explanation of the optical changes. The large electron density contrast between the gold core and water masked the small changes in electron density due to the polymers attached to the surface.

2.4. Agglomeration Experiments

In this section, typical experimental data for the observation of steady states of agglomeration is presented. Agglomeration is induced by introducing $50\,\mathrm{mmol\,L^{-1}}$ HCl in the particle dispersion. Further findings on the influence of the HCl concentration are presented in section 2.5.

2.4.1. Results

The UV/Vis and SAXS data of an agglomeration experiment with $50\,\mathrm{mmol\,L^{-1}}$ HCl concentration and particles from batch 3 are compared with the corresponding stable particle dispersion in fig. 2.7.

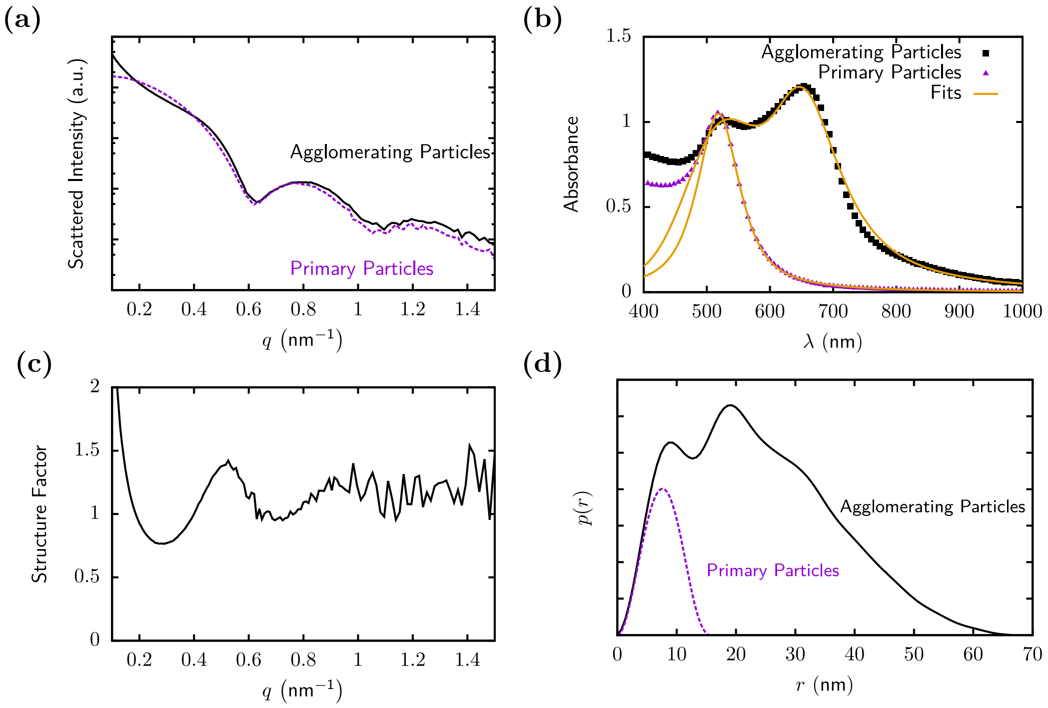

Figure 2.7.: (a) SAXS patterns (curves are not shifted) and (b) UV/Vis absorbance spectra (no offset) of stable dispersions compared to the signals of an agglomerating sample. (c) Effective structure factor from dividing the agglomerate scattering pattern by the primary particle pattern. (d) Pair distance distribution functions calculated from the scattering patterns.

The SAXS patterns differed mainly at $q < 0.6\,\mathrm{nm}^{-1}$, before the first minimum of the Porod oscillations (fig. 2.7 (a)). The statistical errors were smaller than $10\,\%$ in the plotted range. They are not shown for better visibility. While the slope towards small angles was essentially flat (compare also fig. 2.6 (a)), the scattering of the agglomerating sample exhibits a clear upturn at lower angles, eventually scattering stronger than the dispersed particles. Above the point of inflexion, the agglomerates display an additional region of excess scattering.

The UV/Vis spectra of both agglomerates and primary particles (fig. 2.6 (b)) exhibited the localised surface plasmon resonance peak around 520 nm, typical for gold nanoparticles. Only every 15th data point was plotted to increase visibility. The statistical errors were smaller than $7\,\%$ in the plotted range. They are not shown for better visibility. Compared to the primary particles, the agglomerates displayed a distinct, redshifted secondary peak that was even larger than the primary particle peak in this case. The area of the secondary peak was found to account for $\sim 70\,\%$ of the total area by fitting the agglomerate spectrum with the double peak function described in section 2.2.3 (fit plotted as yellow line in fig. 2.6 (b)). The normalised flocculation parameter $P_\mathrm{n} = 14.1$ was calculated from the spectra according to eq. (2.5).

The effective structure factor (fig. 2.6 (c)) was calculated by dividing the agglomerate scattering by the primary particle signal (see also section 1.3.2.3). It displayed a single, broad and relatively small peak centred at $q_\mathrm{max} \sim 0.5\,\mathrm{nm}$. At the right flank of the peak and higher q values, the structure factor data was disturbed by increasing noise and did not allow further conclusions.

The pair distance distribution functions (fig. 2.6 (d)) were calculated from the indirect Fourier transform of the scattering patterns. The distance distribution of the primary particles displayed a single peak. The pair distance distribution of the agglomerates featured additional contributions at larger distances. The real space radius of gyration was calculated from $p(r)$ via eq. (2.2). The value for primary particles, $R_\mathrm{g}^\mathrm{Part} \sim 5.7\,\mathrm{nm}$, was smaller than the mean radius of gyration of the agglomerated sample, $R_\mathrm{g}^\mathrm{Agglo} \sim 19.0\,\mathrm{nm}$. When comparing the magnitude of the estimations for the standard deviation calculated by the fitting tool, 0.001 nm for the primary particles and 0.1 nm for the agglomerated particles, it becomes obvious that the calculated size values for agglomerates are much more sensible to input data variations compared to the primary particles. The numerical values for the errors result from a built-in routine that evaluates a series of Monte-Carlo simulations and calculates the standard deviation of the values. It serves to compare the quality of the approximation for different measurements.

2.4.1.1. Fouling Issues

The particles from a destabilised dispersion did not only agglomerate in solution, but also adsorbed at the inner walls of the system. The adsorption could be directly observed by comparing measurements of pure water immediately before and after the experiment. The material that is adsorbed strong enough to endure gentle washing produces an additional scattering and absorbance signal compared to the original measurement.

The phenomenon could be traced by observing the temporal evolution of the detector signals for an agglomeration experiment performed at a hydrochloric acid concentration of $39.4\,\mathrm{mmol\,L^{-1}}$ and a total flow rate of $100\,\mathrm{\mu L\,s^{-1}}$ (compare fig. 2.10). The profile of the SAXS intensity at $q = 0.2\,\mathrm{nm}$ during the experiment (fig. 2.8 (a)) separated in three sections.

I The pure water measurement in the clean system showed no excess scattering compared to the background (set as lower limit of the y-axis), certainly because the background was determined under equivalent conditions.

II The mixture of AuNP dispersion and HCl gradually arrived at the detector. The signal reached an equilibrium corresponding to a steady state of agglomeration.

III During flushing with 20 mL of ultrapure water, free particles and agglomerates were removed from the system[5]. Excess scattering compared to the initial water signal remains.

The average SAXS patterns from II and III in fig. 2.8 (b) clearly illustrate the similar shape between the scattering patterns during the agglomeration experiment and after flushing. The statistical errors for the agglomeration grew from values smaller than 7 % below $q = 1\,\mathrm{nm}^{-1}$ to up to 60 % in the noisy, high-q parts for the agglomeration measurement. For the measurements after flushing, the statistical errors stayed below 30 % for $q < 0.8\,\mathrm{nm}^{-1}$. At higher q values the errors grew larger than the actual signal. Error bars are not shown for better visibility.

Similar to the scattering evolution in fig. 2.8 (a), the profile of the UV/Vis absorbance in fig. 2.8 (c) represented the three phases during the experiment. The signal was low during I, strongest during II and did not return to the baseline during flushing III. The strong overshoot at the beginning of III appeared because the tube used for flushing was initially filled with particle dispersion.

The UV/Vis spectrum fig. 2.8 (d), calculated from averaging the steady state agglomeration signal in II, clearly displayed a secondary agglomeration peak. After thorough flushing, an attenuated signal, similar in shape, remained. The statistical errors in the relevant range (400 nm to 800 nm) were below 3 %.

---

[5] The gap between the measured points resulted from delays in the detection system. The corresponding UV/Vis dataset contains the complete range.

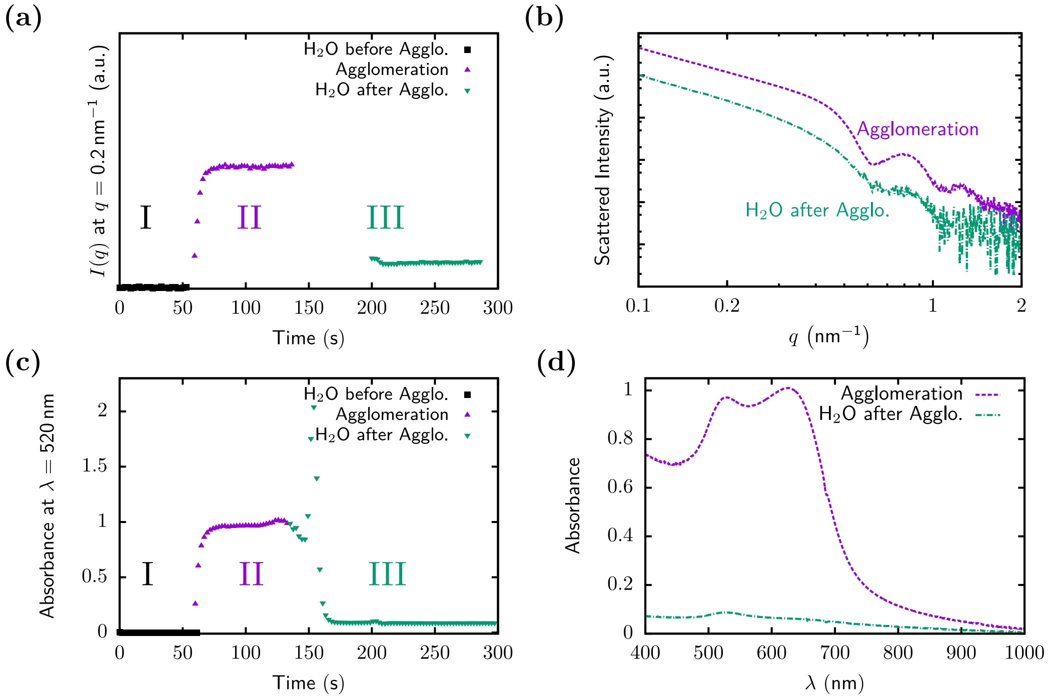

Figure 2.8.: (a) Evolution of the SAXS intensity during a typical agglomeration experiment ($c_{\mathrm{HCl}} = 39.4\,\mathrm{mg\,mol^{-1}}$). (b) Background corrected SAXS patterns, calculated from averages over the flat areas of the agglomeration and flushing sections in (a). (c) Absorbance at $\lambda = 520\,\mathrm{nm}$ measured over the course of the experiment from (a). UV/Vis absorbance spectra from II and III.

2.4.2. Discussion

Particle adsorption on the inner walls of the system is observable already after a single experiment. The clear excess scattering and absorbance, remaining after thorough flushing, prove more or less strongly adsorbed sample fractions in the beam paths. These adsorbed particles should be acknowledged in the analysis. To ensure comparable conditions between different measurement runs, the cleaning protocol from section 2.2.6 was used before all separate measurement runs presented in the remaining sections of this chapter.

The detection and characterisation of steady states of agglomeration was demonstrated with the novel experimental setup. The upturn at low q values for scattering patterns as well as the large area fraction of the second peak in the UV/Vis spectra compared to the single particle measurements are clear signatures of agglomeration. The scattered intensity/absorbance of the agglomerates was about an order of magnitude larger compared to the signal of adsorbed particles. It is therefore safe to assume that the signal is mainly generated by agglomerates.

The mean age of the agglomerates observed in SAXS was 2 s, the upper boundary is 9 s (see fig. 2.5). Their scattering pattern plotted in fig. 2.7 in contrast was averaged over 22 s. For the UV/Vis measurements the integration time (12 s) was also above the upper boundary for the observed agglomerate age (11 s). *This divergence of sample age and integration times would not be achievable in a single measurement run for any other method, highlighting the uniqueness of the approach introduced in this work.*

The peak in the effective structure factor is further proof for the formation of static agglomerates. For most measurements presented in this chapter, the changes in this peak could not be quantified reliably. For the given acquisition parameters, the agglomerated fraction was too small to produce a usable structure factor signal (see also fig. 2.9 (d)). Structure factors are therefore excluded from further considerations.

The pair distance distribution is a useful tool to describe the agglomeration process for the measurements presented in this chapter. The single peak in the distance distribution of the primary particles is a consequence of the spherical shape. For a homogeneous sphere with radius R, the radius of gyration is $R_\mathrm{g} = \sqrt{\frac{3}{5}}R$, i.e. the measured value $R_\mathrm{g}^\mathrm{Part} \sim 5.7\,\mathrm{nm}$ fits well to the expected value based on the core radius fit, $R'_\mathrm{g} = 5.6 \pm 0.1\,\mathrm{nm}$. The emergence of distances above the single particle cutoff is a clear signature of agglomeration. Due to the different distributions entering the signal, the agglomerate size distribution can not be extracted straightforwardly.

The measured signals contain signatures of well-dispersed particles and agglomerates. The presence of unagglomerated particles is indicated by the significant single particle peak in the UV/Vis patterns. The presence of a distribution of agglomerate sizes emerges from the distribution of agglomerate ages and the statistical nature of the agglomeration process. While the *deconvolution of the signal into the individual contributions from the monomer to the n-mer was not possible in this project.*

Even when considering the mean radius of gyration as a good estimation of the average agglomerate size, conclusions on the actual structure of the agglomerates are difficult. The mean radius of gyration gives a quantitative estimate for the mean size of the agglomerates. It is clear that the agglomerates do not possess large scale translational symmetry due to the absence of well-defined superstructure peaks in the effective structure factors. In absence of sharp features, the true sample structure is masked by the loss of phase information in the SAXS intensity signal.

Based on the mean radius of gyration $R_\mathrm{g} = 19\,\mathrm{nm}$, the mean number of particles in the observed agglomerates can be estimated. The radius of gyration depends not only on the particle number, but also on their arrangement, therefore the interval of possible particle numbers is large. The maximum value for a given number of constituent particles is realised by a linear particle chain. The minimum value is achieved by a close packed structure.

The boundary values for the number of particles were calculated by numerical calculation of eq. (2.2) for close packed and linear agglomerates. The number of particles in the average agglomerate lies approximately between[6] 5 and 15. The difference between the absorbance spectra in fig. 2.2 is small in this range. Furthermore, the normalised flocculation parameter values measured here are never reached for the agglomerates from the analytical ultracentrifugation study [110] introduced in section 2.2.3. The agglomerates characterised in [110] likely possess a different structure with less interparticle plasmon coupling than the agglomerates produced here. Therefore, direct assignment of the UV/Vis contributions to a certain number of particles in an agglomerate is not possible. Even when involving the absorbance spectra, the precise agglomerate structure can not be resolved.

2.5. Solvent Variation

In this section, different amounts of hydrochloric acid from $7\,\mathrm{mmol\,L^{-1}}$ to $50\,\mathrm{mmol\,L^{-1}}$ were added to the nanoparticle dispersion to induce agglomeration. Only measurements on batch 1 to 7 are discussed, the results from batch 8 to 10 (where particle core size and surface are different) are addressed in section 2.7.

2.5.1. Results

The concentration of hydrochloric acid was varied from $7\,\mathrm{mmol\,L^{-1}}$ to $50\,\mathrm{mmol\,L^{-1}}$ in various experiments, utilising different particle batches and often scanning several concentrations during a single measurement run. The total flow rate was set to $100\,\mathrm{\mu L\,s^{-1}}$ for all results presented in this section, corresponding to average agglomerate ages of approximately 1 s at the UV/Vis detector and 2 s at the intersection with the X-ray beam. Several separate experimental runs were performed on the particles from the first synthesis. Different HCl concentrations were set during

---

[6] For 4 particles, the close packed value is $R_\mathrm{g}^\mathrm{cp} = 10\,\mathrm{nm}$, the corresponding linear chain has a larger radius $R_\mathrm{g}^\mathrm{lin} = 17\,\mathrm{nm}$. For 14 particles, $R_\mathrm{g}^\mathrm{cp} = 16\,\mathrm{nm}$ and $R_\mathrm{g}^\mathrm{lin} = 58\,\mathrm{nm}$.

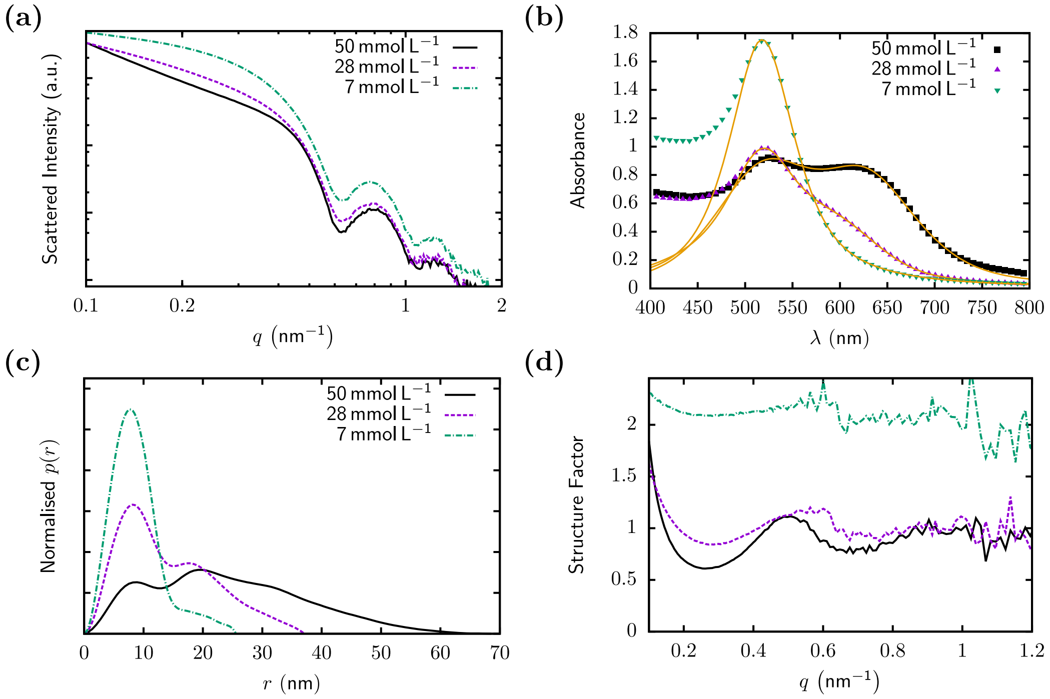

Figure 2.9.: (a) SAXS patterns (curves are not shifted) and (b) UV/Vis absorbance spectra (no offset) of agglomerating samples at different HCl concentrations in the solvent. (c) Effective structure factor from dividing the agglomerate scattering pattern by the primary particle pattern. (d) Pair distance distribution functions calculated from the scattering patterns.

every run and the resulting steady state of agglomeration was detected. Due to experimental difficulties, some measurements were rejected[7]. In the following, the results of seven experimental series are compared. Qualitatively, all results were similar to the results presented in fig. 2.7. Due to the relatively large number of processed scattering patterns and absorbance spectra, only a representative dataset is fully reported (fig. 2.9), the remaining results are reported as processed results in fig. 2.10.

The SAXS patterns displayed an increasing slope at smaller angles for increasing HCl concentrations (fig. 2.9 (a)), suggesting the formation of larger scattering struc-

---

[7] Some measurements contained errors due to difficulties with the valve or pump control or the data acquisition. Another rejection criterion were inconsistencies in the background or particle reference measurements.

tures. The UV/Vis spectra in fig. 2.9 (b) supported these findings. The redshifted part of the spectrum increased likewise with the HCl concentration.

The pair distance distribution functions, presented normalised with their respective areas in fig. 2.9 (c), allowed deeper interpretation of the SAXS results. The distributions exhibited a clearly increasing fraction of larger distance contributions upon increasing HCl concentration.

The effective structure factor peak was most pronounced at high HCl concentrations (fig. 2.9 (d)). For most lower concentrations, the peak was barely separated from the statistical noise. Therefore, analysis of the structure factors is omitted in the following.

The mean radii of gyration in fig. 2.10 (a) were calculated from fig. 2.9 (c) and the additional data not shown elaborately here using eq. (2.2). They clearly increase upon increasing the HCl concentration, a distinct sign for agglomeration of the particles. There is some fluctuation, but the trend is clear. Two different agglomeration metrics calculated from the UV/Vis data are plotted in fig. 2.10 (b). Both, the area fraction of the secondary peak from the fits (see fig. 2.2) and the normalised flocculation parameter (eq. (2.5)) increased with increasing HCl concentration.

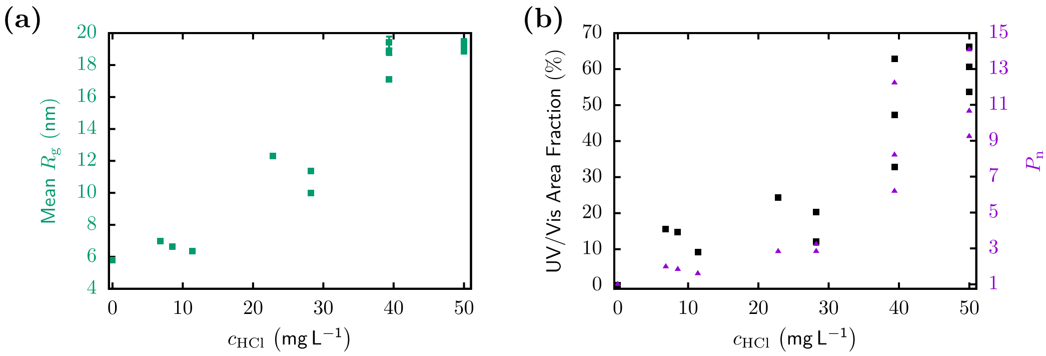

Figure 2.10.: (a) Mean radius of gyration for different HCl concentrations. (b) Fraction of the secondary UV/Vis peak and normalised flocculation parameter, determined by fitting UV/Vis spectra corresponding to the measurements presented in (a).

2.5.2. Discussion

Increasing the hydrochloric acid concentration in the continuous phase induces faster agglomeration. The increased ion concentration leads to increased screening of the electrostatic repulsion and therefore accelerates agglomeration. Furthermore, larger HCl concentrations reduce the pH of the solution, from 7 to 1.3. The isoelectric point of the particles is expected to be around pH ~ 2 [114], therefore the surface potential is likely drastically lowered over the observed concentration range.

The agglomeration characteristics (size and flocculation parameter) roughly increase linearly with the acid concentration, the mean radius of gyration approximately doubled when doubling the HCl concentration. The data presented in this section prove a clear trend of growing agglomerates for increasing acid concentration. Estimated stability ratios (from calculated DLVO potential at different ionic strengths) reach unity (the flat part of fig. 1.3) already at concentrations below $20\,\mathrm{mmol\,L^{-1}}$ for the used particle systems[8]. These estimations do not include the charge reduction of the surface due to the decreased pH, which would decrease the critical coagulation concentration further. The agglomeration rate therefore still depends on the acid concentration, although the critical coagulation concentration should be exceeded by far. This effect could be caused by kinetics faster than diffusion-limited agglomeration (DLA), as they were found for the precipitation kinetics of a similar particle system (with 10 nm radius) that was destabilised with HCl in a similar concentration range [105].

Around the intermediate HCl concentrations ($25\,\mathrm{mmol\,L^{-1}}$), dimers already dominated the results. The radius of gyration of a dimer pair is $R_\mathrm{g} \sim 9.1\,\mathrm{nm}$, and this value was crossed at $25\,\mathrm{mmol\,L^{-1}}$ HCl.

There was considerable scatter in the measured size and optical data. The measurements were very sensitive to external perturbations. The most aberrant datasets (not included in the graphs) were found for measurements that were acquired without conducting the cleaning protocol described in section 2.2.6. A likely candidate generating unsystematic errors is the uncontrolled amount of nanoparticle adsorption emerging during a measurement run. Several measurements where rejected due to errors in the automatic operation of the valves, the resulting drastic concentration errors could be identified.

2.6. Velocity Variation

The purpose of the measurements presented in this section was to examine the temporal evolution of the agglomeration process. To tune the age of the agglomerates, the total flow rate and hence the mean resident time before arrival at the detector positions were varied.

---

[8] Assuming a Zeta potential of $\sim 50\,\mathrm{mV}$ (taken from particles prepared by the same method) approaches unity around ion concentrations of $17\,\mathrm{mmol\,L^{-1}}$ (calculated with equations from [22, pp. 312 et sqq.]).

2.6.1. Results

The total flow rate was changed from 200 µL s^{-1} to 25 µL s^{-1}. The ratio between the flow rates was kept at 1:1 and the resulting HCl concentration in the sample was 17 mmol L^{-1}. The corresponding mean agglomerate ages (according to fig. 2.5) range from 0.5 s to 3.6 s at the UV/Vis detector and from 0.9 s to 6.9 s at the SAXS capillary. The SAXS patterns in fig. 2.11 (a) changed only subtly. The most obvious change is the increasing width of the first minimum. A slight increase of the low q slope was also visible.

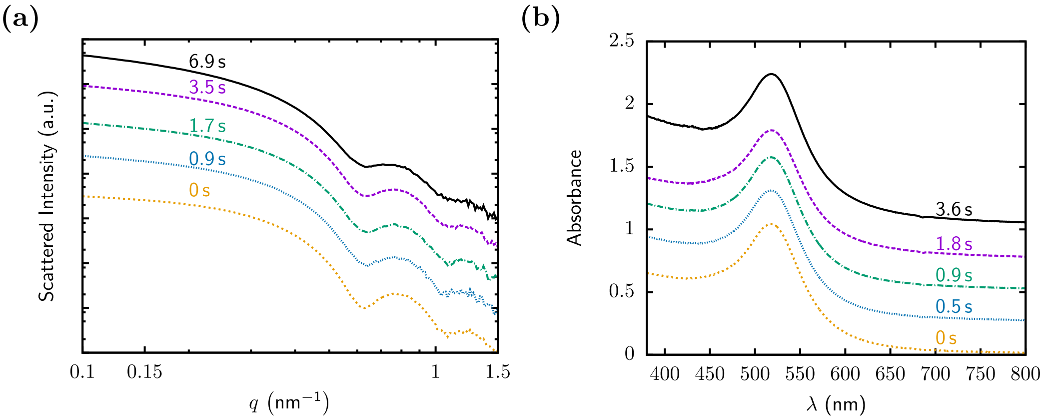

Figure 2.11.: (a) SAXS (vertically offset by a factor of 5) and (b) UV/Vis (offset by successively adding +0.25) results for different agglomerate ages as indicated in the graphs. The measurements at 0 s refer to the stable dispersion.

The UV/Vis spectra (fig. 2.11 (b)) similarly only displayed minute changes.

The differences between the different agglomerate ages are augmented by considering the results of the analysis in fig. 2.12. The different colours represent results from two independent measurements. The SAXS and UV/Vis time axes are different due to the different positions along the flow path of the detectors.

The mean radius of gyration, determined from the pair distance distribution function, clearly increased upon decreasing the flow rate (fig. 2.12 (a)). It almost doubled compared to the value for separated particles (0 s).

The trend for the flocculation parameter (fig. 2.12 (b)) was similar. For both separate measurements, the flocculation parameter increased when increasing the age of the observed steady state of agglomeration.

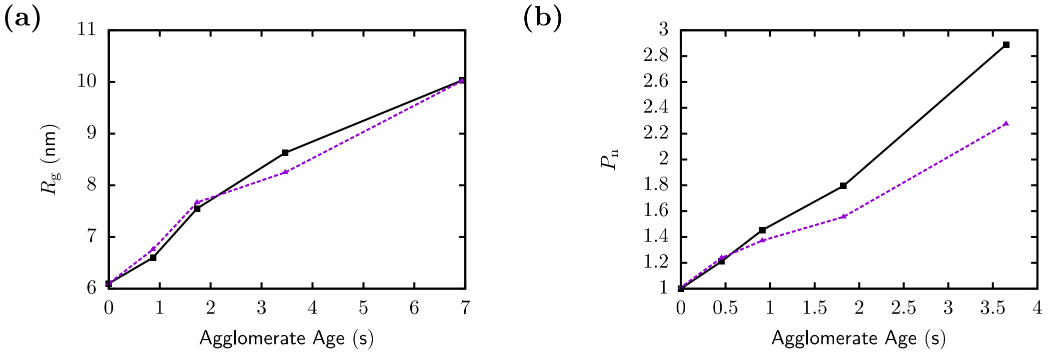

Figure 2.12.: (a) Mean radius of gyration for different flow velocities, drawn as a function of the mean agglomerate ages. (b) Normalised flocculation parameter, drawn as a function of the mean agglomerate ages.

2.6.2. Discussion

The age of the observed steady state of agglomeration could be tuned by varying the flow velocity. The growth of the mean radius of gyration during the first 7 s of agglomeration was observed and compared to the increase in absorbance at higher wavelengths. The curvature of the growth curve suggests a power law behaviour for the growth, but the observed time interval was too small to numerically confirm this. The process therefore appears to be rather diffusion-limited than reaction-limited. Considering the concentration dependence found in section 2.5, the growth likely represents a crossover between the limiting cases of DLA and RLA. The curvature of the growth curve is compatible to the kinetics expected based on literature that describes agglomeration regimes apart from DLA and RLA [105] (calculated with parameters for 17 mmol L^{-1} HCl), but the observed time scale is too small to reliably determine asymptotic behaviour. The results should be taken with a grain of salt, since the mixing efficiency is known to decrease for the older agglomerates from the mixing characterisation results (see fig. 1.11).

The HCl concentration affects the structure of the agglomerates. When comparing the measurements for later stages of agglomeration, presented here, with results from section 2.5, the SAXS measurements at 7 s and 28 mmol L^{-1} respectively displayed almost identical radii of gyration. Their normalised flocculation parameters were $P_n \sim 2.6$ for agglomeration at 17 mmol L^{-1} HCl after 3.6 s and $P_n = 3.3$ for agglomeration at 28 mmol L^{-1} HCl after 0.5 s. The larger flocculation parameter values suggest that the agglomerates produced at 28 mmol L^{-1} are overall more dense, since a closer approach of particles in an agglomerate generates stronger redshifted absorption. This is a counterintuitive result, since the higher attraction at higher acid concentrations should actually lead to less efficient packing. The difference could alternatively be related to the reduced mixing efficiency at lower flow velocities.

2.7. Particle Variation

A second synthesis batch was used to study the effect of surface modification on the agglomeration behaviour. Batch 8, 9 and 10 are particle dispersions with identical gold cores, stabilised with citrate, PEG and MUTEG respectively (see section 2.2.1).

2.7.1. Results

The steady state of agglomeration for the different particles was characterised at a flow rate of $100\,\mu\mathrm{L\,s^{-1}}$, which corresponds to average agglomerate ages of approximately 1 s at the UV/Vis detector and 2 s at the intersection with the X-ray beam. The HCl concentration was varied from $7\,\mathrm{mmol\,L^{-1}}$ to $137\,\mathrm{mmol\,L^{-1}}$.

The scattering patterns of steady states of agglomeration for the citrate-, PEG- and MUTEG-stabilised particles at selected HCl concentrations are compared in fig. 2.13 (a). Both the citrate- and PEG-stabilised particles displayed an increasing lower q range slope when increasing the HCl concentration. The scattering patterns of the MUTEG-modified particles did not exhibit noticeable changes upon increasing the HCl concentration.

The corresponding UV/Vis spectra followed similar trends. The citrate- and PEG-stabilised particles exhibited an increasing redshifted signal for increased HCl concentrations. Again, the signal for the MUTEG-stabilised particles did not change systematically in the observed range of HCl concentrations.

The visual impression on the sample behaviour is confirmed by the results of further analysis (fig. 2.14). While the mean radius of gyration for agglomerating samples from batch 8 and 9 more than doubled when the HCl concentration was increased, it did not follow a clear trend for the MUTEG-stabilised particles, the size remained low. The initial jump at $7\,\mathrm{mmol\,L^{-1}}$ likely resulted from random fluctuations, the magnitude depended strongly on the selected data range (the presented value resulted from the automatic selection by the *datgnom* program).

Compared to fig. 2.10, the results on the relative areas were not conclusive and are not shown here. The normalised flocculation parameter for the citrate- and PEG-stabilised particles clearly increased for increasing HCl concentrations. Again, the values for MUTEG-stabilised particles remained at the level for dispersed particles and did not display a clear trend.

Independent measurements of the hydrodynamic radius R_h (a measure for the size of the contour of particles) by dynamic light scattering, were performed on

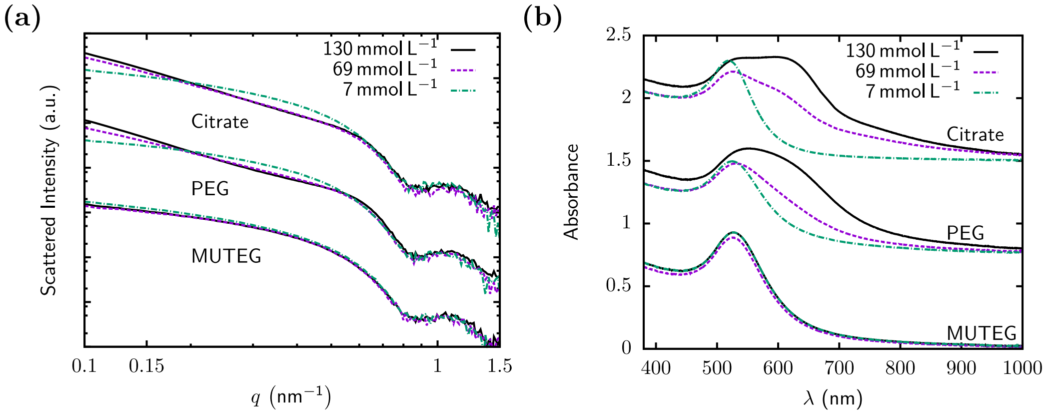

Figure 2.13.: (a) SAXS results for agglomerating particles from batch 8, 9 and 10 at different concentrations. The graphs for the different particle types are offset by successive multiplication with 32. (b) UV/Vis spectra corresponding to (a). Different particle batches are separated by adding +0.75.

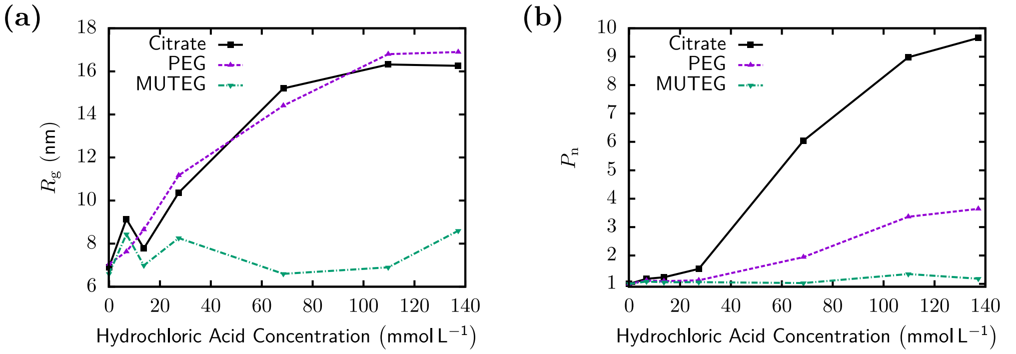

Figure 2.14.: Overview of fit results for the agglomeration of particles from the second synthesis with different surface modifications. (a) Mean radius of gyration and (b) normalised flocculation parameter at different HCl concentrations for batch 8, 9 and 10.

the stable dispersions for synthesis quality control. The size of the particles was $R_\mathrm{h} = 7.2 \pm 0.6\,\mathrm{nm}$ for citrate stabilisation, $R_\mathrm{h} = 8.4 \pm 0.3\,\mathrm{nm}$ for MUTEG modification and $R_\mathrm{h} = 7.8 \pm 0.5\,\mathrm{nm}$ for PEG modification. The size of citrate-stabilised particles is considerably larger than the core size determined by SAXS, $R_\mathrm{SAXS} = 5.2 \pm 0.6\,\mathrm{nm}$, likely due to the electrical double layer of the particles. Although the

PEG molecule is larger compared to the MUTEG molecule (see fig. 2.6 (d)), the size of the contour was smaller.

2.7.2. Discussion

Particles from batch 9, modified with PEG, are mainly stabilised by charges. The agglomerate sizes of the citrate- and PEG-stabilised particles change likewise when changing the HCl concentration. Therefore the destabilisation mechanism, the weakening of the electrostatic repulsion by pH reduction and ionic strength increase, likely concur. Consequently their stabilisation should concur too.

The charge stabilisation coexists with adsorbed PEG molecules on the surface, because the adsorption is proved by the UV/Vis data (fig. 2.6 (b)). Furthermore the agglomerate spectra display a reduced redshifted component for the PEG modified particles compared to the original citrate-stabilised dispersion. The PEG molecules increase the interparticle distance inside an agglomerate, reducing the interaction between the surface plasmons.

Surface modification by MUTEG prevents agglomeration under pH/ionic strength conditions that unambiguously destabilise identical particles stabilised with citrate or PEG. One difference is the size of the molecules: The estimated end-to-end distance in a linearly extended state is 0.5 nm for the citrate, 2.9 nm for the MUTEG and 7.8 nm for the PEG (see fig. 2.6 (d)). Although the MUTEG molecules are shorter compared to PEG, their steric stabilisation is more effective.

A possible explanation for the different agglomeration behaviour of PEG and MUTEG would be a difference in surface coverage of the different particles. If the surface coverage of the PEG was relatively small, it would explain their sensitivity to the acid concentration, since a considerable part of the repulsive interaction would be caused by the residual citrate ions. Sparse coverage with PEG molecules would not provide sufficient repulsion when the electrostatics are screened. The coverage can not be directly assessed by the data presented here, but the smaller shift and width of the UV/Vis peak of the PEG-stabilised particles compared to the MUTEG particles could be a sign for their reduced surface coverage. A low surface coverage for PEG is further supported by the dynamic light scattering measurements. The smaller hydrodynamic radius of the PEG-stabilised particles was caused by their lower surface coverage compared to the MUTEG particles.

At high concentrations the agglomerates did not grow significantly. Above HCl concentrations of 100 $\mathrm{mmol\,L^{-1}}$, the the citrate and PEG samples did not grow considerably upon a concentration increase. This suggests that the ccc has been crossed and the growth process became purely diffusion limited. Whether the actual dynamics follow the expected power law growth for DLA can not be determined from the presented data. Additional measurements for the kinetics would be required.

The agglomerate sizes at equal conditions are comparable between the separate batches. Despite their different size and surface modifications, the mean radii of gyration of agglomerates prepared from batches 4, 8 and 10 were similar, e.g. at $\sim 30\,\mathrm{mmol\,L^{-1}}$ 10.7 nm, 10.4 nm and 11.2 nm respectively. Conversely, the optical properties were different. The normalised flocculation parameter of agglomerates from batch 4 (core radius 7.2 ± 0.6 nm), $P_\mathrm{n} \sim 3$, was significantly larger compared to the agglomerates of particles with smaller cores (core radius 5.2 ± 0.6 nm), $P_\mathrm{n} \sim 1.5$ for citrate stabilisation and $P_\mathrm{n} \sim 1.1$ for PEG stabilisation. Different particle arrangements in the agglomerate and differences in plasmonic coupling due to the size likely caused the optical changes despite similar agglomerate sizes.

2.8. Summary and Conclusions

The agglomeration process of aqueous gold nanoparticles, induced by addition of dilute HCl, in a laminar flow was studied with a purpose-built setup. The destabilisation is caused by protonation of the surface bound citrate groups and the increased screening of the residual charges due to the higher concentration of dissolved ions.

Studies on steady states are feasible with the purpose-built flow system. The stable observation of transient states for observation times larger than the age of the prepared state itself was demonstrated throughout this chapter. Certain complications with adsorption and age distributions were encountered, but meaningful results could be acquired. The flexible setup even allowed to perform the experiments at a synchrotron beamline.

The kinetics of the agglomeration process could not be explained by the limiting DLA/RLA regimes. *The HCl concentration* influenced the agglomeration rate. The agglomerate size was evaluated for identical growth times. Different sizes therefore reveal different growth rates. Higher HCl concentrations induced faster agglomeration, even far above the predicted critical coagulation concentration according to the DLVO theory. When the agglomerate age was directly varied by *the flow velocity*, the growth kinetics resembled diffusion limited growth with a modified exponent.

The stabilising mechanism of three different surface modifications could be characterised. Citrate-stabilised particles were sensitive to changes in the amount of dissolved acid. The PEG coating was found to be ineffective in preventing agglomeration, likely due to low surface coverage, whereas the MUTEG stabilisation proved effective against addition of acid due to the steric stabilisation effect. The agglomerate size for different particle types (core and surface modification) was similar for identical conditions (except the MUTEG coated particles that did not agglomerate). The optical properties of the agglomerates depended strongly on the ligands and core sizes.

The specifics of the agglomeration process of sterically stabilised particles are examined in chapter 3.

3. Agglomeration of Unpolar Gold Nanoparticles

3.1. Introduction

The agglomerates produced in chapter 2 did not exhibit long range ordering between the constituting particles. Depending on the application, disordered superstructures might be favourable or not. For certain usage scenarios it is favourable to be able to tune the superstructures from disordered to ordered.

In this chapter the fundamental principles for the formation of specific, ordered or disordered, nanoparticle superstructures is discussed. The focus is not to develop specific applications, but to generally explore structure formation mechanisms of sterically stabilised, unpolar gold nanoparticles, when agglomeration is triggered by a rapid increase of solvent polarity through mixing with polar solvents. The particle system was chosen because sterically stabilised particles are used in many modern processes and gold displays exceptionally low reactivity. The resulting particles are expected to be relatively stable when left undisturbed. A deeper understanding could allow generalisation of the findings to other particle systems.

The morphology of NP aggregates, especially the contrast between order and disorder, can influence their function. In thin film solar cells, both ordered [6, 115] and disordered [7] superstructures can be employed. The disordered structures act as diffuse broadband reflectors while ordered structures reflect only certain wavelength bands, matching the distance of the particles in the superstructure, and allow for tunable transmission.

When used as pigment, ordered superstructures produce iridescent structural colours. Noniridescent structural colour can be induced by superstructures only exhibiting close range order without long range translational order [116, 117].

Typically, the particles forming superstructures that interact with visible light have radii above 100 nm, since the interparticle distance has to match the wavelength of visible light (400 nm to 800 nm). The typical application envisioned specifically for gold nanoparticle superlattices in the size range used in this chapter are optical metamaterials, based on plasmonic effects [4].

The research goal is here to find the process parameters, as well as the related microscopic mechanisms that determine the formation of ordered or disordered agglomerates. A deeper understanding could allow generalisation of the findings to other particle systems. A strong motivation for this research were the results of a preceding project (see section 1.2.3.3). They suggest that the ligand-mediated contributions to the interparticle interaction dominates the structure formation.

Many modern functional nanoparticles (e.g., semiconducting Quantum Dots, high refractive index zirconia, conductive indium tin oxide) are sterically stabilised and serve as building blocks of functional superstructures. If the structure formation is solely determined by the ligands, the findings should be applicable for all of the materials, given the ligand shells are identical.

In contrast to already published results, this research puts an emphasis on

- *in situ* studies of structure formation
- in varying solvent conditions and simultaneous
- studies of the optical properties of the agglomerates, where
- the observed agglomerates are detected after growth times as low as a few seconds.

As it was already explained in section 1.2.3.3, the agglomerate structure, resulting from the rapid destabilisation, has so far only been determined *ex situ*, mainly by performing TEM (and to a smaller extent SAXS studies) on samples taken from the precipitated sample fraction after 2 h incubation time. Optical measurements for the different agglomerate structures were previously not performed systematically.

In this study it was found that the structure of agglomerates can be tuned by varying the temperature and the solvent composition. The superstructure could be shown to alter the optical properties of otherwise identical particles. For optimised process conditions (solvent composition and temperature), ordered fcc superstructures form in suspension, already after 3 s.

3.2. Methods

Gold nanoparticles with radii $< 10\,\mathrm{nm}$ were destabilised by mixing with polar solvents of different polarities at different controlled flow velocities and temperatures in a purpose built flow system, as sketched in fig. 1.10. Coupled SAXS and UV/Vis spectroscopy were performed in situ on the flowing sample. Prior to every agglomeration experiment, the same particle batch with the same concentration was measured in a well-dispersed state to allow direct conclusions on the effects of agglomeration on the measured signal.

3.2.1. Particles

AuNPs sterically stabilised by 1-dodecanethiol, 1-hexadecanethiol or 1-octadecanethiol (denoted C12, C16 and C18) and dispersed in heptane were synthesised by two different one-phase, one-pot reactions.

The so-called "Zheng" method was adapted from [17]. For a standard synthesis 309 mg $AuClPPh_3$, the stabilising alkylthiol (311 µL C12, 338 mg C16 or 375 mg C18) and 527 mg borane *tert*-butylamine complex, $(CH_3)_3CNH_2{\cdot}BH_3$ (TBAB), were dissolved in 50 mL of benzene. The solution was slowly heated and stirred. During 2 h reaction time, the chloro(triphenylphosphine)gold(I) was reduced by the TBAB and a bright red particle dispersion formed. The AuNPs were precipitated by adding 50 mL of ethanol and centrifugation at 4000 rpm. The supernatant was removed and the precipitate was redispersed in 50 mL *n*-heptane. The synthesis yielded a stable dispersion of NPs with a gold core of approximately 3.0 ± 0.3 nm (see table 3.1 (a) for real values), gold concentrations around $3.6\,\mathrm{g\,L^{-1}}$, covered with different alkylthiols as a stabiliser.

The other particle type, herein after referred to as "Wu" particles, were synthesised following a protocol adapted from [18]. For a typical synthesis 500 mg of dry chloroauric acid were dissolved in a mixture of 45 mL *n*-heptane and 45 mL oleylamine. After stirring for 10 min with 500 rpm at room temperature, 200 mg TBAB dissolved in a mixture of 5 mL *n*-heptane and 5 mL oleylamine were added. The solution was stirred at 500 rpm for 1 h. During that time, the $HAuCl_4$ was reduced and AuNPs formed. The oleylamine capped particles were precipitated by adding 200 mL ethanol and 5 min of centrifugation at 4000 rpm. The precipitate was resuspended in 100 mL *n*-heptane.

Shortly before the experiments, several 10 mL aliquots were taken to exchange the oleylamine on the surface with different alkylthiols (C12, C16, C18) according to a procedure described in [118]. 472 mg triphenylphosphane and the corresponding thiol (364 mg C12, 465 mg C12 and 516 mg C18) were dissolved in 10 mL *n*-heptane and the solution was heated to 90 °C. The aliquots were also heated and poured in the respective thiol solutions. After shaking gently, the solution was left undisturbed until it cooled down. After cooling the ligand exchange was complete and the excess reagents were removed by washing. The dispersion was precipitated by addition of 20 mL ethanol and centrifugation at 4000 rpm. After removing the supernatant, the precipitate was redispersed in 10 mL heptane. The product was a stable dispersion of gold nanoparticles, with core sizes around 3.0 nm, stabilised with different thiols.

Prior to the experiments, the particle dispersions were heated to ensure good dispersion and filtered in a preheated 0.2 nm PTFE syringe filter to remove large agglomerates and possible foreign matter from the dispersion.

3.2.2. Experimental Setup

The results presented in this chapter were produced at the SWING beamline of the SOLEIL synchrotron. The experimental setup (fig. 3.1) was slightly modified compared to the one from chapter 2. A new SAXS capillary holder (the capillary was the same sort, 1 mm diameter borosilicate glass) with a bore hole and fittings to connect a water thermostat (PHYSICA "VT 100") for temperature control was employed. A large volume (∼ 5 L) temperature controlled water bath was applied to immerse most of the system: A delay line before the mixer (∼ 80 cm), the mixing element and the UV/Vis flow cell were immersed in the bath to precisely control temperature. A different UV/Vis cell with a drastically reduced optical path (∼ 1 mm compared to ∼ 10 mm for the aqueous particles) was used due to

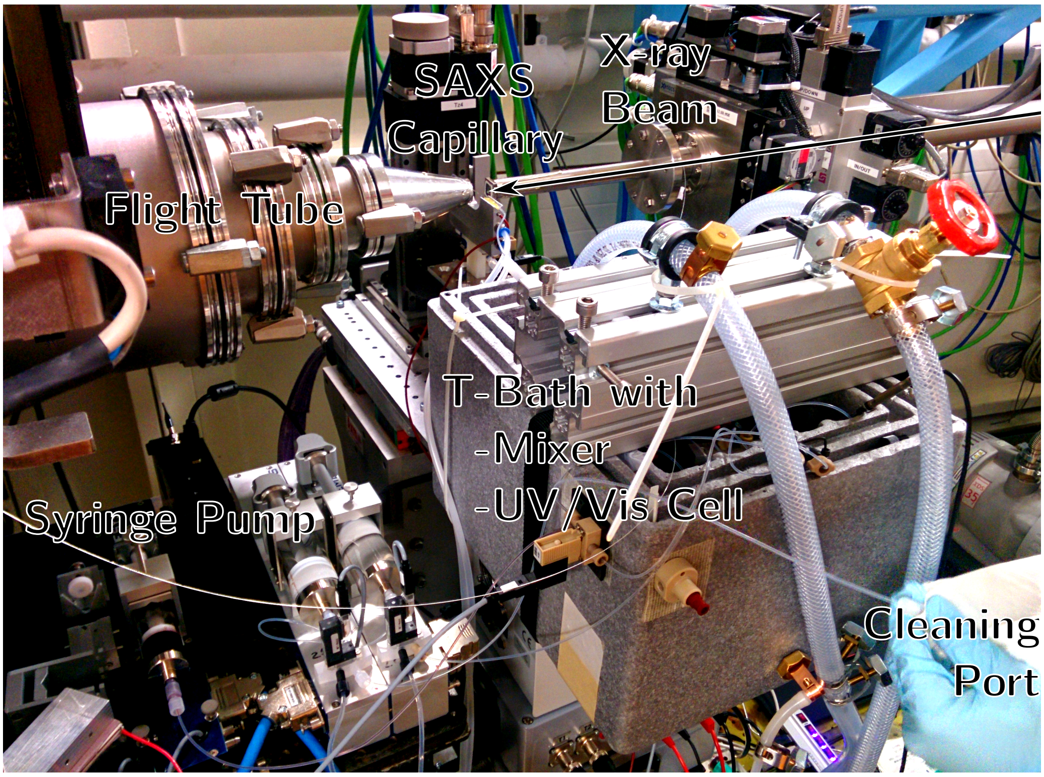

Figure 3.1.: Photo of the setup at the SWING beamline of the SOLEIL synchrotron.

the higher gold concentration of the unpolar particles (compare section 2.2.1 and section 3.2.1) and the resulting reduced transmission. The temperature stability of the sample from the mixer to the SAXS capillary is expected to be better than ±2 K.

3.2.3. Agglomeration Experiments

The aim of this study was to characterise steady states of agglomerating, sterically stabilised gold nanoparticles under different conditions and in particular to understand the prerequisites for the formation of ordered superlattices with the help of the flow setup. As already explained in section 1.2.3.3, NPs sterically stabilised with unpolar chains are well-dispersed in unpolar solvents. The solubility parameters are similar, which implicates a Flory parameter $\chi < \frac{1}{2}$ and therefore a repulsive interaction mediated by the ligands according to section 1.2.2.3. When increasing the solvent polarity, e.g. by mixing a polar solvent like 1-propanol with the dispersion, the stabilising alkyl chains of one particle become more soluble in the alkylthiol monolayers of the other particles, i.e. χ increases and turns the ligand layer interaction to an attractive interaction. This way, the short ranged steric repulsion is switched to a short ranged attraction mediated by the ligands.

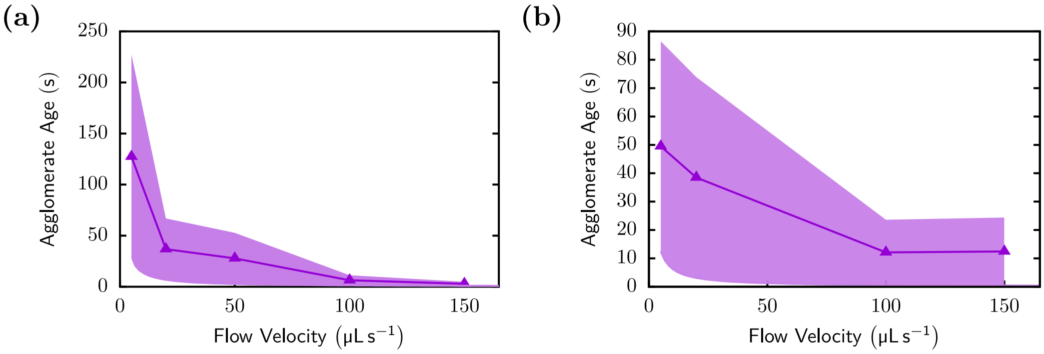

Figure 3.2.: Estimates of the observed agglomeration time at the (a) SAXS and (b) UV/Vis detector for the flow velocities employed here.

For the research presented in this chapter, different amounts of 1-propanol or ethanol were mixed with the stable dispersion inside the “MR-Lab MX” mixing module (see section 1.3.3.1). Flow rates from 2 µL s^{-1} to 150 µL s^{-1} were used, the corresponding agglomeration times observed at the particular detection points are drawn in fig. 3.2. Due to the hydrodynamic dispersion (section 1.3.3.2), the actually observed agglomerate age is an average over a certain distribution. The boundaries drawn in fig. 3.2 are conservative estimates (determined in analogy to section 2.2.5): The lower bounds were calculated by estimating how long the fastest flow line needs to reach the detector. The upper bounds were measured by applying a concentration jump at the entrance of the mixer. The setup was filled with pure heptane which was replaced by a AuNP dispersion with the respective flow rate. The dispersion continuously replaced the pure solvent, the process was traced by the scattered intensity and maximum absorbance respectively. At some point the signals reached an equilibrium; concentration changes could no longer be resolved. The width of the rising edge in the signal is added to the lower boundary to obtain an upper boundary for the observed agglomerate age.

The UV/Vis detector is placed approximately midway between the mixing point and the SAXS detector. Accordingly the agglomerates observed by UV/Vis are approximately half as old as the observed sample in SAXS.

3.2.4. SAXS

The principle setup of a SAXS measurement was already introduced in fig. 1.8. The raw data correction was performed according to the scheme in fig. 1.9. The particularities of the setup and methods used in this chapter are described in the following.

3.2.4.1. Instrumentation

The X-ray source at the SWING beamline is an undulator in the storage ring of the SOLEIL synchrotron. A beam energy of 11 keV ($\lambda = 0.113\,\mathrm{nm}$) was selected with a Si(111) double crystal monochromator. The X-ray beam was further defined with two mirrors in Kirkpatrick-Baez configuration and a number of adjustable slits. The beam size for the experiments presented here was set to 450 µm × 20 µm. The Aviex "PCCD170170" CCD detector has an active area of 171 mm × 171 mm and was set to an effective pixel size of 166.8 µm. The sample to detector distance was set to 1.8 m. The transmitted intensity was recorded with a PIN-diode in the 7.5 mm × 3 mm beamstop for transmission corrections during background subtraction.

3.2.4.2. Data Evaluation

The size and polydispersity of the nanoparticles in stable dispersion were different from synthesis to synthesis. They were determined by fitting the form factor of polydisperse spherical particles. Typically the data is fitted well, as exemplified by the scattering data from a stable dispersion of "Wu C16" particles and the respective fit in fig. 3.3. When following the algorithm described in appendix A, the fit yields a mean radius of $3.0 \pm 0.2\,\mathrm{nm}$ for this particle type. The excess intensity of the measured data at higher q values likely results from detector noise[1]. Equivalent

---

[1] An upturn of intensity is found in all measurements, even for the calibration measurements with theoretically flat intensity profile.

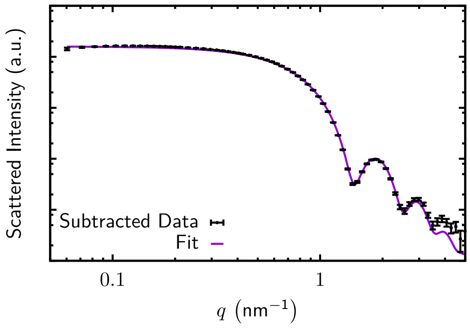

Figure 3.3.: Scattering pattern of a "Wu C16" particle dispersion at 35 °C. The fit of a polydisperse sphere form factor agrees well with the data.

measurements were performed for every batch that was filtered to compare the resulting size and get accurate results for the effective form factor associated to the different concentrations.

The structure factor $S(q)$ of an agglomerated sample was calculated from the background corrected sample scattering $I_{\mathrm{S}}(q)$ and the corresponding effective form factor $I_{\mathrm{Part}}(q)$ with the monodisperse approach (see also eq. (1.22))

$$S(q) = \frac{I_{\mathrm{S}}(q)}{I_{\mathrm{Part}}(q)}, \tag{3.1}$$

as sketched in fig. 3.4. The division corresponds to the addition of $I_{\mathrm{S}}(q)$ and the reciprocal of $I_{\mathrm{Part}}(q)$ on a logarithmic scale (see fig. 3.4 (a)). The background corrected sample scattering $I_{\mathrm{S}}(q)$ is divided by the fit result for the effective form factor to obtain the effective structure factor plotted as a solid black line in fig. 3.4 (b).

Förster *et al.* describe a flexible model function for NP superlattices [119] that is used in this chapter. The peak positions q_{max}^{hkl} are generally related to the cubic lattice constant a by

$$q_{\mathrm{max}}^{hkl} = \frac{2\pi\sqrt{h^2+k^2+l^2}}{a}. \tag{3.2}$$

For the fcc crystal structure (see fig. 3.4 (d) for a sketch of the unit cell), the next neighbour distance of the particles is in the $\langle 110 \rangle$ direction. The centre-to-centre distance of neighbouring particles d_{ctc} (see fig. 3.4 (d)) is related to the cubic lattice constant by

$$d_{\mathrm{ctc}} = \frac{a}{\sqrt{2}}. \tag{3.3}$$

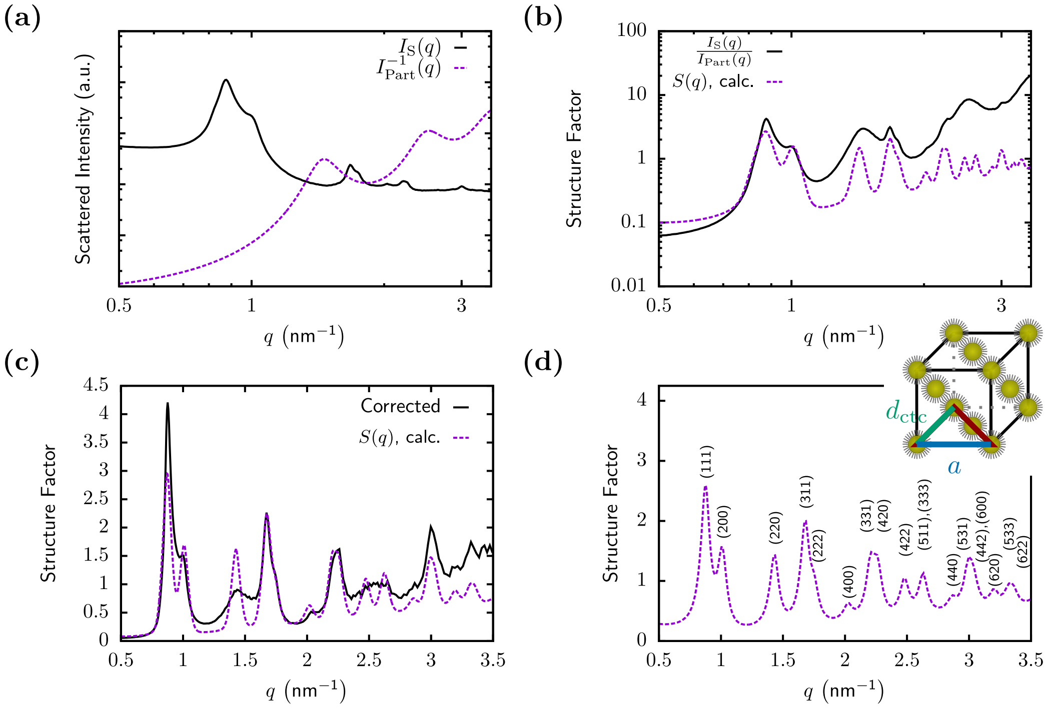

Figure 3.4.: (a) SAXS pattern of agglomerates and the reciprocal of the effective form factor of the constituent AuNPs, the ingredients for structure factor calculation. (b) Result of naive division compared to a model structure factor. (c) Structure factor calculated with background correction compared to the theoretical structure factor. (d) The corrected structure factor on a linear scale, compared to the peak positions of a fcc lattice. The inset sketches the unit cell of a fcc nanoparticle superlattice. a denotes the cubic lattice parameter, d_{ctc} is the distance between nearest neighbours (along the $\langle 110 \rangle$ direction).

The theoretical structure factor for a NP superlattice with fcc domains of $L = 105\,\mathrm{nm}$ average size and cubic lattice constant of $a = 12.44\,\mathrm{nm}$ is plotted as reference (see fig. 3.4 (d) for a clearer plot including peak indices and a sketch of the cubic unit cell of the fcc structure with particles in the centres of the faces). The calculated structure factor is built upon peaks with adjustable shape, representing a convolution of a Gaussian and a Lorentzian peak. Their relative position and height is determined by the allowed fcc reflections and the corresponding multiplicities. The width is inversely related to the domain size. Additional scattering due to size polydispersity of the particles and lattice disorder is included with terms corresponding to the Debye-Waller factor [120, 121]. The parameters were chosen to match the measured effective structure factor as close as possible.

While the peak positions are practically identical, the height is different between the curves, most notably around $q = 1.4\,\mathrm{nm}^{-1}$ and at higher q values. The differences at high q originate from the unexpectedly flat scattering curve of the agglomerates in the high q regime. This likely resulted from a combination of detector noise due to the low scattered intensity compared to the peaks and parasitical scattering of depositions on the capillary walls. This effect is accounted for by subtracting a constant background from the signal, whose magnitude is chosen to level $S(q \sim 3.5\,\mathrm{nm}^{-1}) \sim 1$. The resulting corrected structure factor is compared with the calculated curve in fig. 3.4 (c).

The Scherrer equation [122] relates the domain size L of an ordered superstructure of (almost) identical scatterers to the width of the structure factor peaks [123]. If the FWHM of a diffraction peak at the scattering angle $2\Theta_0$, $\Delta_{2\Theta_0}$, is not corrected for peak broadening due to instrumental effects[2],

$$L = \frac{K\lambda}{\Delta_{2\Theta_0} \cos \Theta_0} \tag{3.4}$$

gives a lower boundary for the domain size. K is a coefficient related to shape and usually in the range $0.9 \ldots 1$, here a value of $K = 0.9$ is used. The domain size itself represents a lower boundary for the agglomerate size.

The most significant feature of the structure factor for amorphous agglomerates is a wide structure factor peak. This single, broad peak was attributed to the structure factor of a glass-like nanoparticle superstructure lacking long-range order. Even without periodic arrangements, there is a recurring distance inside a more or less close packed particle agglomerate due to the finite, monodisperse particle size. According to the Ehrenfest relation [124, p. 72] [125], a scattering, amorphous structure induces a structure factor peak centred at

$$q_{\max} = \frac{2\pi \cdot 1.23}{d_{\mathrm{ctc}}}. \tag{3.5}$$

Here d_{ctc} represents the average distance of the particle cores of two particles in contact.

3.3. Primary Particles

Before every agglomeration experiment, the employed primary particles were characterised in the same concentration to enable better comparisons[3]. Below a certain,

---

[2] For SAXS experiments, experimental broadening is usually insignificant.

[3] The actual particle concentration in the syringe differs from experiment to experiment because the amount adsorbed in the filter is not controllable.

ligand dependant temperature, the pure particles dispersions become unstable and start to agglomerate [49] (see also section 1.2.3.3). The experiments presented here were exclusively performed at temperatures above the precipitation temperature of the respective ligand.

3.3.1. Results

The experimental results are summarised in the following. The difference between "Zheng" and "Wu" particles is introduced in section 3.2.1.

3.3.1.1. Wall Fouling

In section 2.4.1.1 it was already pointed out that adsorption of AuNPs on the walls of the detection volume influences the measurements. The scattering pattern and the UV/Vis spectrum of pure heptane were measured immediately before ("initial") and after ("final") a stable dispersion of "Wu C16" particles was filled in the capillary. It was found that even for the stable dispersions a certain amount of AuNPs is adsorbed at the walls of the SAXS capillary, as it is evidenced by the increased scattering signal of pure heptane after the dispersion was thoroughly flushed from the capillary in fig. 3.5 (a). The difference between final and initial scattering patterns (fig. 3.5 (a)) further illustrates the adsorption of gold, since it resembled the background subtracted pattern of an agglomerating gold dispersion (compare (c)). The UV/Vis absorbance of the final measurement calculated relative to the initial one (fig. 3.5 (b)) revealed a clear signal of agglomerated gold particles as well. The error bars were on the order of the line thickness.

Depending on the reference used, the corrected signals of the particles slightly differed. While the absorbance barely changed (fig. 3.5 (d)), the background subtracted SAXS patterns (fig. 3.5 (c)) displayed visible deviations at the lower and upper boundaries of the angular range. The adsorption took place during the measurement of the gold dispersion, in principle the subtraction of the final background should correct for the excess scattering due to the adsorbed particles and deliver better results. The slight downturn of the scattered intensity at smaller angles can be explained by a repulsive interparticle interaction. The steeper decay at larger angles is closer to the q^{-4} asymptote expected for smooth particle surfaces.

The fit results for radius and polydispersity were robust against the changes in background, since the width and position of the first minimum barely changed between the different backgrounds. The resulting fit parameters for both backgrounds are virtually identical. The resulting fitted mean radii and distribution widths are $r_\mathrm{i} = 3.061 \pm 0.002\,\mathrm{nm}$ and $r_\mathrm{f} = 3.049 \pm 0.002\,\mathrm{nm}$, and $\Delta r_\mathrm{i} = 0.229 \pm 0.002\,\mathrm{nm}$ and $\Delta r_\mathrm{f} = 0.224 \pm 0.002\,\mathrm{nm}$ for the initial and final backgrounds respectively. The errors are estimates for the parameter errors taken from

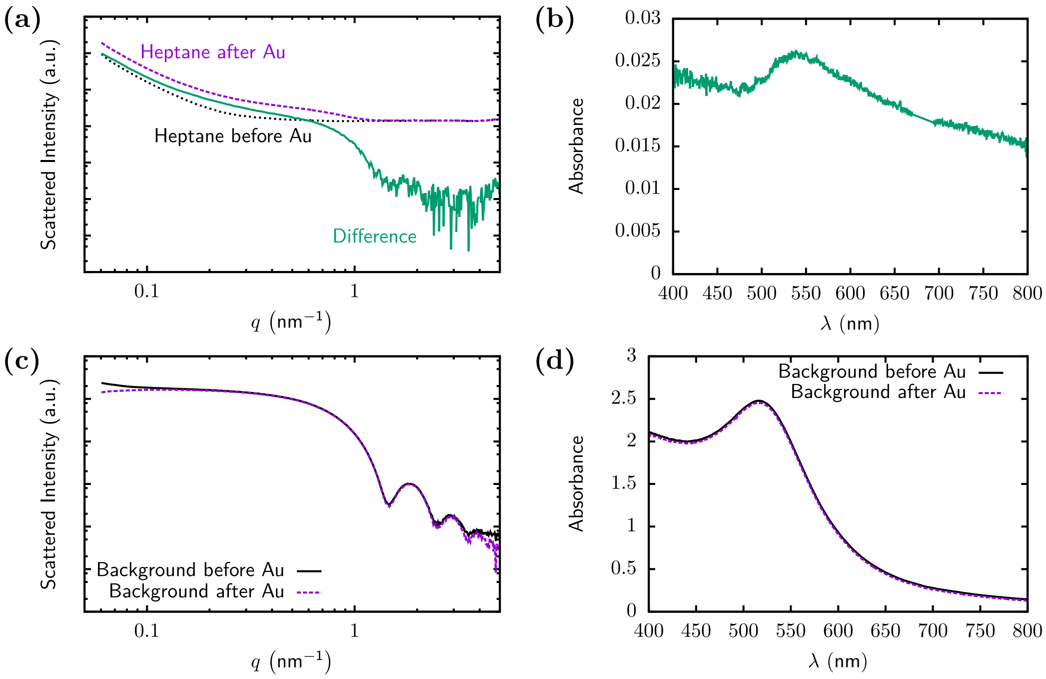

Figure 3.5.: (a) SAXS patterns of heptane-filled capillaries before and after exposing the inner wall to a gold dispersion, and the difference between signals. (b) Absorbance calculated with the final heptane measurement as signal and the initial measurement taken as reference. (c) Background subtracted SAXS patterns of “Wu C16” particles at 35 °C, with background measurements taken before and after the measurement of the dispersion. (d) Absorbance of “Wu C16” particles at 35 °C with reference measurements taken before and after the sample measurement. All data points are plotted without offset.

the covariance matrix resulting from the least squares fit. While they are unphysically small, they provide a measure to compare how tight the parameters are bounded in the respective fits. In table 3.1 the fit results for all particles are summarised.

3.3.1.2. Comparison

Three different particle types, stabilised with several linear alkylthiols were employed here: “Zheng” particles, “Wu” particles and “Wu 2” particles with increased particle radius (see section 3.2.1). The thiol is denoted by the number of carbons in the alkyl chain (C12, C16, C18). The primary particle measurements were only weakly temperature-dependant, for brevity only one measurement per particle type is shown here. The data shown here was averaged over 10 or more single measurements. The error bar size is on the order of the line thickness, therefore error bars are not shown.

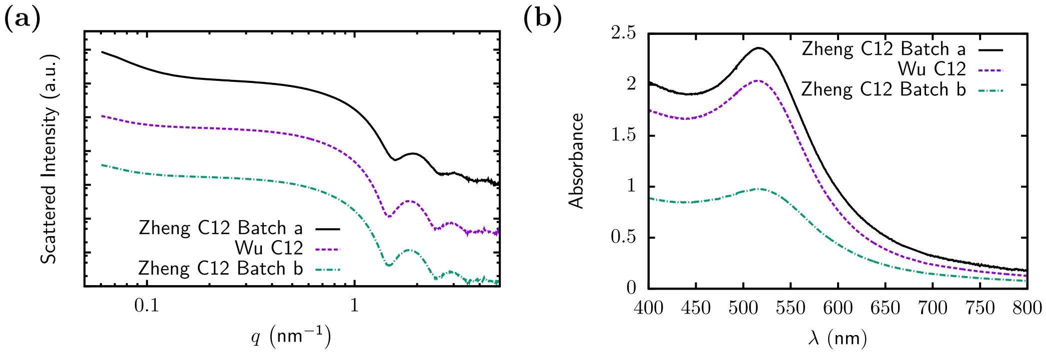

Figure 3.6.: SAXS patterns (a) and UV/Vis spectra (b) of "Zheng C12" and "Wu C12" particle dispersions at 35 °C. SAXS data are offset by a factor of $10^{1.45}$, the UV/Vis spectra are not normalised.

Two separate synthesis batches of "Zheng C12" particles were used. The core sizes and polydispersities of the "Zheng C12" particle batches and also the "Wu C12" particles were slightly different, as indicated by the different position and shape of the minima in fig. 3.6 (a) and the corresponding fit results in table 3.1 (a). Due to the logarithmic intensity scale of the SAXS patterns, the concentration difference is more obvious in the UV/Vis spectra fig. 3.6 (b). The minor differences in the peak position and width (table 3.1 (b)) are barely visible in the UV/Vis spectra.

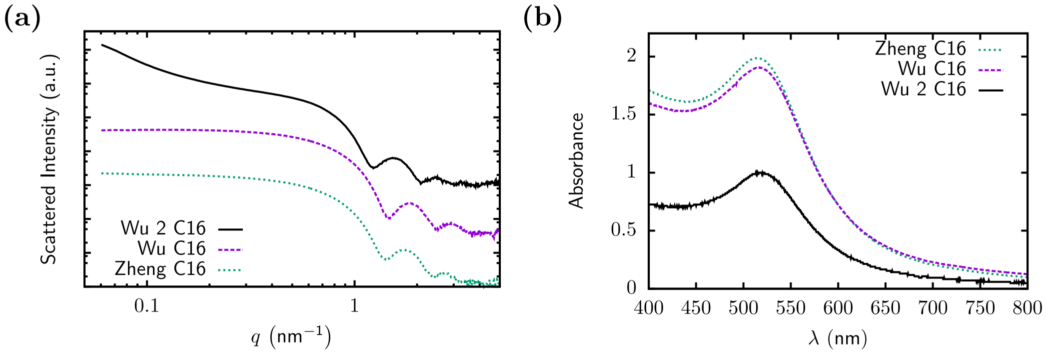

Figure 3.7.: SAXS patterns (a) and UV/Vis spectra (b) of "Zheng C16", "Wu C16" and "Wu 2 C16" particle dispersions at 45 °C. SAXS data are offset by a factor of $10^{1.45}$, the UV/Vis spectra are not normalised.

Three distinct core radii were prepared with the hexadecanethiol ligand. While the SAXS patterns (fig. 3.7 (a)) are again strongly dependant on size and polydispersity, the UV/Vis results mainly reflect the concentration difference with only minor changes in peak position and width.

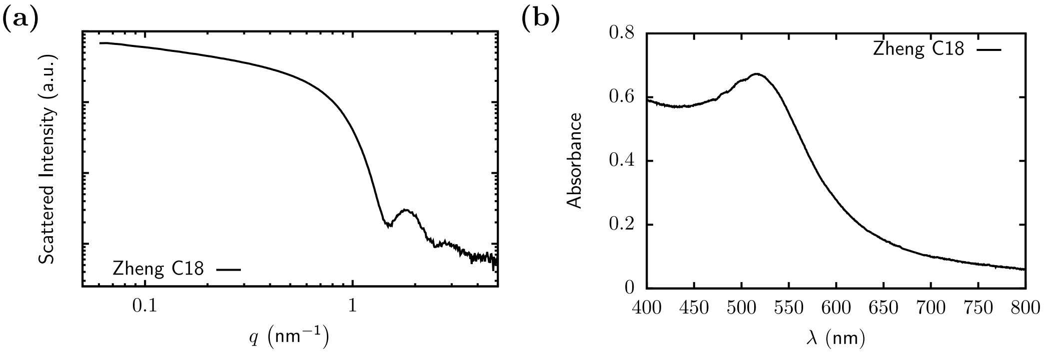

Figure 3.8.: SAXS patterns (a) and UV/Vis spectra (b) of “Zheng C18” particle dispersions at 60 °C.

In this study, only “Zheng” particles were prepared with octadecanethiol as a ligand. The SAXS and UV/Vis results largely resemble the other ligand lengths (fig. 3.8 and table 3.1).

Table 3.1.: Fit results for the primary particles employed here. (a) Core radii of the different particles, determined by fitting with a Schulz-Zimm size distribution. The numbers represent centre value and width of the distribution. (b) Position and HWHM of the LSPR peak for the primary particles.

(a)

	Radius (nm)		
	“Zheng”	“Wu”	“Wu 2”
“C12 a”	2.8 ± 0.3	3.0 ± 0.2	
“C12 b”	2.9 ± 0.3		
“C16”	3.2 ± 0.3	3.0 ± 0.2	3.6 ± 0.3
“C18”	3.0 ± 0.3		

(b)

	LSPR Peak Position ± Width(nm)		
	“Zheng”	“Wu”	“Wu 2”
“C12 a”	516 ± 33.5	515 ± 33	
“C12 b”	516 ± 36.5		
“C16”	514 ± 34	516 ± 33	517 ± 30
“C18”	516 ± 35.5		

The main fit results are summarised in table 3.1. The values are representative also for the additional measurements not plotted in the graphs above. The concentration variations do not manifest in the fitted values, because in the dilute regime the concentration only influences the signal strength, not the shape of the curves. The influence of the concentration on the scattering is captured by a single parameter, which was determined for all measurements and taken into account when comparing the different agglomeration measurements.

3.3.2. Discussion

While the optical properties and the size and polydispersity of gold nanoparticles can be reliably determined, the background measurements before and after introducing the dispersion reveal that particles are deposited on the walls of the system, already for the stable dispersion. The measured signal contains the signal of this deposited fraction besides the actual sample. This implies that also the signal of agglomerating samples contains a certain part caused by deposited sample that has to be accounted for. The main influence on the SAXS patterns is in the small and large angle parts. These regions have to be treated carefully in the following discussions, especially for the agglomeration measurements. The UV/Vis spectra change only slightly in the complete observed range. The error due to adsorption is below 10 %. At least for interpretation of the primary particle measurements, no special attention has to be paid to the adsorption phenomenon.

The measurements verify that the syntheses yielded monodisperse gold nanoparticles with different core sizes. The polydispersity of the "Zheng particles" was practically identical to the particles used for the studies described in section 1.2.3.3 and the "Wu" method was able to produce particles with a 2–3 percentage points smaller polydispersity. Polydispersity plays a role for the structure formation process: Early studies on polydisperse hard spheres above their critical volume fractions found a critical polydispersity of 8 %. Above that value, a glass transition is expected for these systems. The polydispersities of the "Wu" (7 %) and "Zheng" particles (10 %) range around this critical value. *It remains to be seen if supercrystalline structures can form for the larger polydispersities.*

Experiments not shown here revealed that T_{A} depends on the core size, larger cores spontaneously agglomerate already at larger temperatures. In the core size range studied here, little to no influence of the core size was found. The aggregation temperature is dominated by the ligands in the frame of this research.

3.4. Solvent Variation

When dispersed in pure heptane and kept at temperatures above the agglomeration temperature, the AuNPs were stable against bulk agglomeration over the course of the measurements. A side effect observed in the stable dispersions was the adsorption of nanoparticles on the inner walls of the system, especially visible in background measurements (see fig. 3.5). The resulting signal distortions at small q values are not expected to disturb the measurements of agglomerate peaks substantially.

If the solvent polarity is increased, the solubility of the stabilising ligands decreases and the particles start to agglomerate at some point. In most sections of this chapter, the solvent composition, employed to induce agglomeration, was fixed to a 1:1 mixture of heptane:1-propanol. Equal volumes of the dispersion (AuNPs dispersed in heptane) and 1-propanol were mixed to increase the solvent polarity and induce agglomeration (in analogy to the preceding project section 1.2.3.3).

In this section, the 1-propanol content is varied. The effect of different solvent polarities (and hence reduced solubility of the ligands in the continuous phase) on the agglomeration process of dodecanethiol-stabilised particles at 35 °C is studied. The difference between “Zheng” and “Wu” particles is introduced in section 3.2.1.

As an additional experiment, ethanol was tested for its applicability to superlattice assembly. The results of these experiments are presented in appendix B.1.

3.4.1. Results

To demonstrate the agglomeration behaviour of the unpolar AuNPs, “Wu C12” particles were precipitated by mixing equal volumes of the dispersion in n-heptane with 1-propanol at 35 °C. The total flow rate was set to $5\,\mu\mathrm{L\,s^{-1}}$, corresponding to approximated agglomerate ages of $3 \pm 2\,\mathrm{min}$ and $1.5 \pm 0.8\,\mathrm{min}$ for the SAXS and UV/Vis measurements respectively (see fig. 3.2). Typical measurements of stable dispersions of “Wu C12” particles are compared with destabilised samples in fig. 3.9 (a) and (b). The measurements presented in this section were performed above the expected transition temperature for ordered and disordered agglomeration based previous studies (see section 1.2.3.3).

The primary particle SAXS measurement was well-approximated by a polydisperse sphere fit (see section 3.2.4.2) and their LSPR peak was equivalent to most other primary particle measurements (section 3.3). Compared to the primary particles, the agglomerating sample exhibited distinct peaks in the SAXS pattern, which were caused by correlations in a superlattice structure with periodically recurring distances between supercrystal planes. The agglomerate UV/Vis spectra displayed a strong redshift of the absorbance. The lower energy portion in the

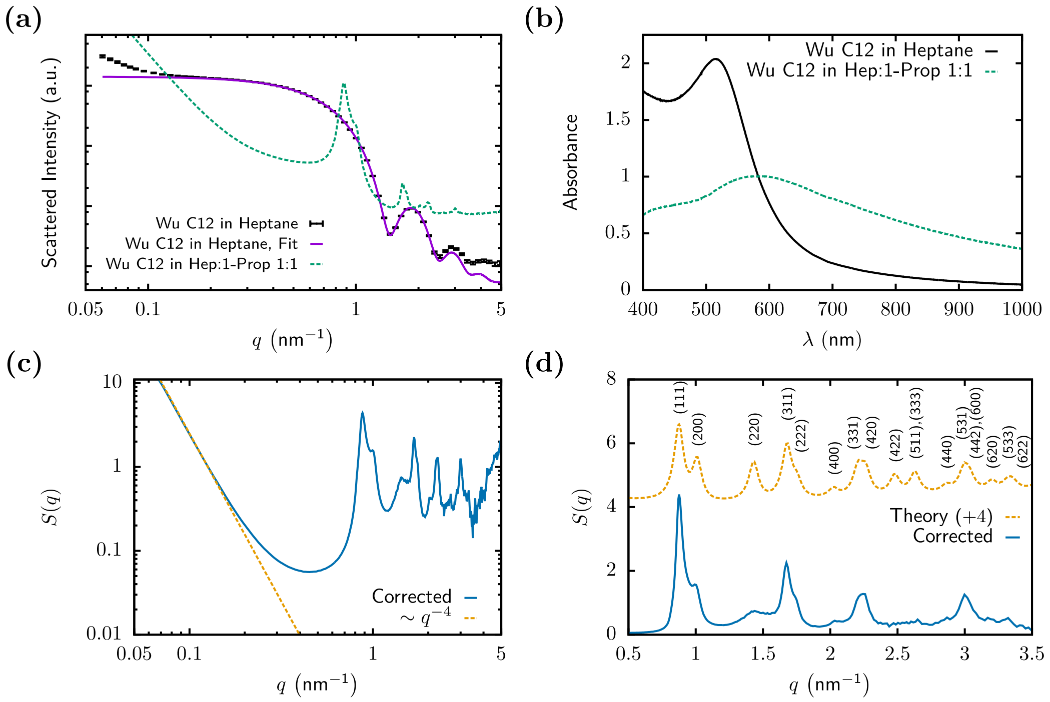

Figure 3.9.: (a) SAXS patterns and (b) UV/Vis spectra for “Wu C12” samples dispersed in pure heptane and agglomerated in a 1:1 mixture of heptane and 1-propanol. (c) Background corrected structure factor on a logarithmic scale. (d) Comparison of corrected structure factor with the calculated function from eq. (3.6).

UV/Vis patterns is readily explained by interparticle interaction effects, inducing additional electron states with lower energy (section 1.3.1).

The resulting structure factor, calculated with the effective form factor and a constant background term[4] as described in section 3.2.4.2, is plotted in fig. 3.9 (c). While the relatively rough estimation of the background might appear arbitrary, it resulted in physical behaviour of $S(q)$ at higher q and did not change the position or width of the structure peaks.

---

[4] The excess scattering responsible for the background is not solely attributable to the structural difference between dispersed and agglomerated particles, because the scattering invariant (eq. (1.20)) also differed. Parts of the excess are explained by detector noise, additional contributions could arise from adsorbed sample at the detector walls.

At low q, $S(q)$ asymptotically approached q^{-4}. This contribution can be attributed to scattering by the outer surface of the agglomerate and can be accounted for by adding the Debye-Büche function S_{DB} to the superlattice structure factor S_{SL}:

$$S(q) = S_{\mathrm{SL}} + S_{\mathrm{DB}} = S_{\mathrm{SL}} + \frac{S_{\mathrm{M}}}{(1+\xi^2 q^2)^2}. \tag{3.6}$$

S_{M} is proportional to the average agglomerate mass and ξ is a measure for the agglomerate size [126]. S_{SL} can be calculated according to the model described in section 3.2.4.2. The Porod oscillations due to the agglomerate size distribution were not resolved in the experiments presented here, due to the limited minimum q value.

At intermediate and higher q values, the corrected structure factor showed strong peaks. The relevant area is replotted on a linear scale in fig. 3.9 (d). The structure factor peak positions could be indexed to a fcc lattice with a cubic lattice constant $a = 12.44\,\mathrm{nm}$. The theoretical structure factor of a fcc superlattice with the same lattice parameter (fig. 3.9 (d), offset by 4) was calculated using the model described in section 3.2.4.2. The ratio of peak heights was different for the measured and calculated peak factor. The most striking difference is the enhanced intensity of the (111) and (200) peaks compared to the rest of the pattern. The (220) peak position is in close vicinity to the first minimum of the particle form factor. The shape of the deviant structure factor parts closely resemble the shape of the minimum. The deviations were likely caused by sensitivity variations of the detector due to the reduced intensity of the agglomerate scattering caused by the form factor minimum. In the following discussion, the peak heights thus have to be handled with care.

In the remaining part of this section, the effect of different solvent compositions on the agglomeration process of 1-dodecanethiol (C12)-stabilised particles (“Zheng” and “Wu”) at 35 °C is discussed.

The relative concentrations could be controlled by adjusting the corresponding flow velocities of the components at a fixed total flow rate. For the experiments with smaller 1-propanol content (7:5, 15:9, 2:1 and 3:1), the NP dispersion flow rate was kept at $2.5\,\mathrm{\mu L\,s^{-1}}$ while the 1-propanol velocity was reduced ($2.083\,\mathrm{\mu L\,s^{-1}}$, $1.875\,\mathrm{\mu L\,s^{-1}}$, $1.667\,\mathrm{\mu L\,s^{-1}}$ and $1.25\,\mathrm{\mu L\,s^{-1}}$). To make up for the reduced volume, additional heptane was mixed in with the difference between $2.5\,\mathrm{\mu L\,s^{-1}}$ and the 1-propanol flow rate as set point. To increase the 1-propanol content compared to the 1:1 case (1:2), the dispersion flow rate was reduced to $1.667\,\mathrm{\mu L\,s^{-1}}$ while the 1-propanol flow rate was set to $3.333\,\mathrm{\mu L\,s^{-1}}$.

The total flow rate of $5\,\mathrm{\mu L\,s^{-1}}$ corresponds to estimated observed agglomerate ages of 3 min and 1.5 min for the SAXS and UV/Vis measurements respectively (see fig. 3.2 for uncertainties). The results are summarised in fig. 3.10.

The SAXS patterns of the “Zheng C12b” particles showed that the 1-propanol concentration strongly influenced the structure of the agglomerates grown for 3 min

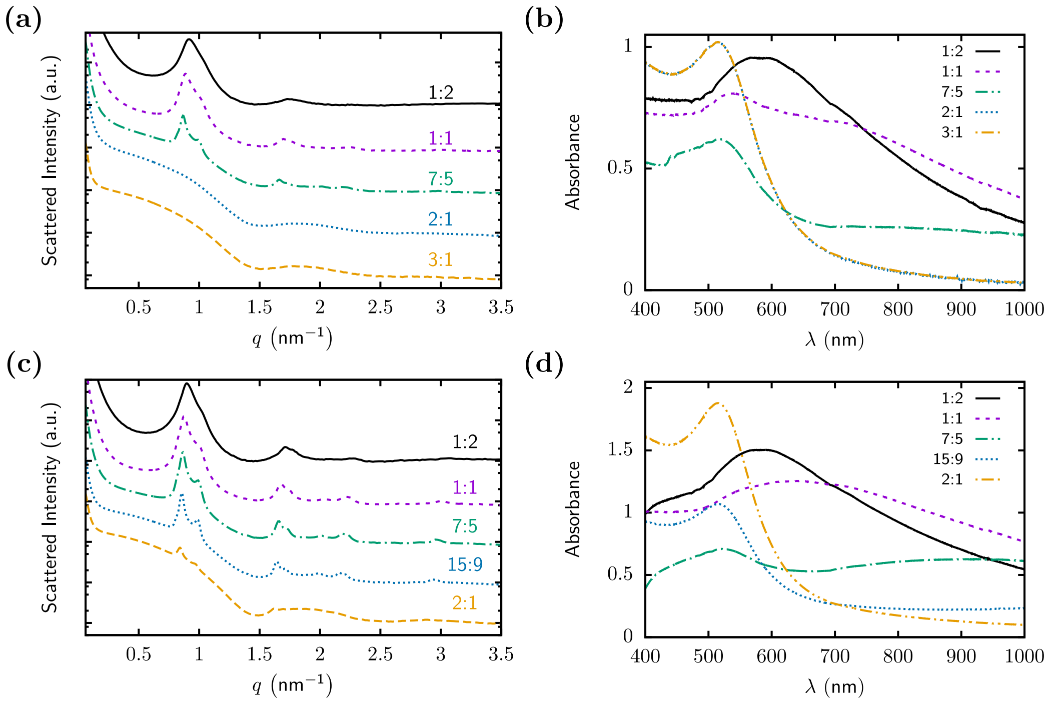

Figure 3.10.: Results of agglomeration experiments with “Zheng C12b” and “Wu C12” particles for different Heptane:1-Propanol volume ratios. (a) SAXS patterns and (b) UV/Vis spectra for “Zheng C12b” samples. (c) SAXS patterns and (d) UV/Vis spectra for “Wu C12” samples.

(fig. 3.10 (a)). While the superlattice peaks were washed out at higher 1-propanol concentrations (1:2 and 1:1), they were completely absent in the measurements at lower concentrations (2:1 and 3:1). At the intermediate concentration, 7:5, the peaks were most defined (see below for quantification). The UV/Vis absorbance spectra corroborated the scattering results. For the low concentrations, 2:1 and 3:1, the spectra were practically identical to the single particle measurements (fig. 3.6). The agglomerate spectra differed considerably. At high polarities (1:2, 1:1) a distinct, redshifted peak formed. For the intermediate polarity (7:5), which displayed the narrowest superlattice peaks, the spectrum can be decomposed to a weakened single particle peak and an additional, broad, redshifted peak.

The behaviour of the “Wu” particles resembled the results for the “Zheng” particles. The superlattice peaks in the SAXS patterns were most pronounced in the intermediate 1-propanol concentration regime (fig. 3.10 (c)). The UV/Vis spectra (fig. 3.10 (d)) displayed similar development to the “Zheng” measurements: For high polarities (1:2, 1:1), the absorbance displayed a single, redshifted peak.

At low polarities (2:1) the spectrum matched the single particle spectrum. At the polarity with the narrowest superlattice peak (15:9), the absorbance was composed of an attenuated single particle peak and a flat, low energy contribution.

To further investigate the agglomerate structure, structure factors were calculated from fig. 3.10 (a) and (b). They revealed that the agglomerate peaks are overall better defined for the “Wu” particles (fig. 3.11 (b)) compared to the “Zheng” particles (fig. 3.11 (a)). At a volume ratio of 2:1, the structure factor of the “Wu” particles still had small peaks where no superlattice peaks were visible for the “Zheng” particles. Apart from that the differences were small, so a structure factor model was used to extract more information from the measurements.

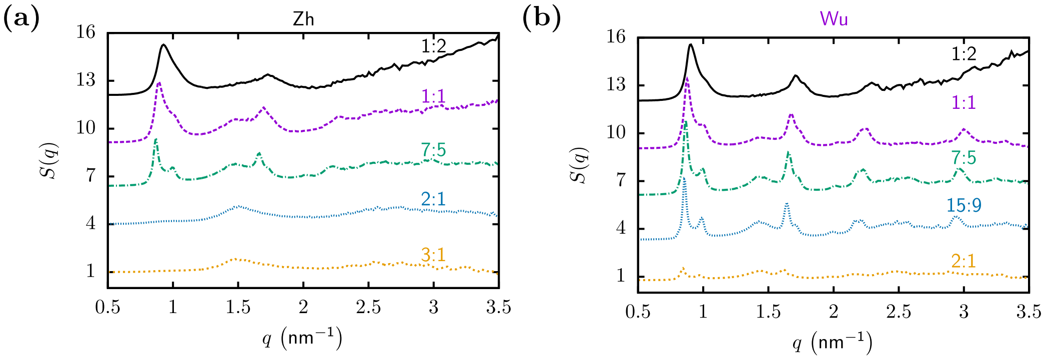

Figure 3.11.: SAXS structure factors for agglomerates composed of (a) “Zheng C12b” and (b) “Wu C12” particles for different heptane:1-propanol volume ratios. The structure factors are successively offset by +3 beginning from the lowest curve.

The structure factors were fit using the previously described model function (see fig. 3.12 (a) for two typical results). In principle, the relation between the peak heights is fixed for a given lattice type and lattice constant. Due to the uncertainty in measured peak heights discussed earlier, the peak height ratios were kept unrestrained for fitting. The width and position of the peaks was fit for the (111), (200), (311) and (222) peaks because their signal was strongest. Although parts of the curve were not approximated well by the model, the peaks themselves were modelled sufficiently. The peak width was used to estimate the size of ordered domains, a measure for the agglomerate size, with the Scherrer equation eq. (3.4). The general trend was that lower 1-propanol concentrations promoted the growth of larger ordered domains (fig. 3.12 (b)). For a 1-propanol volume fraction of $f = 0.33$, no agglomerates were observed for the “Zheng” particles, while the ordered domains for the “Wu” particles are smaller than for $f = 0.37$. The domain sizes of “Zheng” and “Wu” particle superlattices were relatively similar at equal solvent compositions.

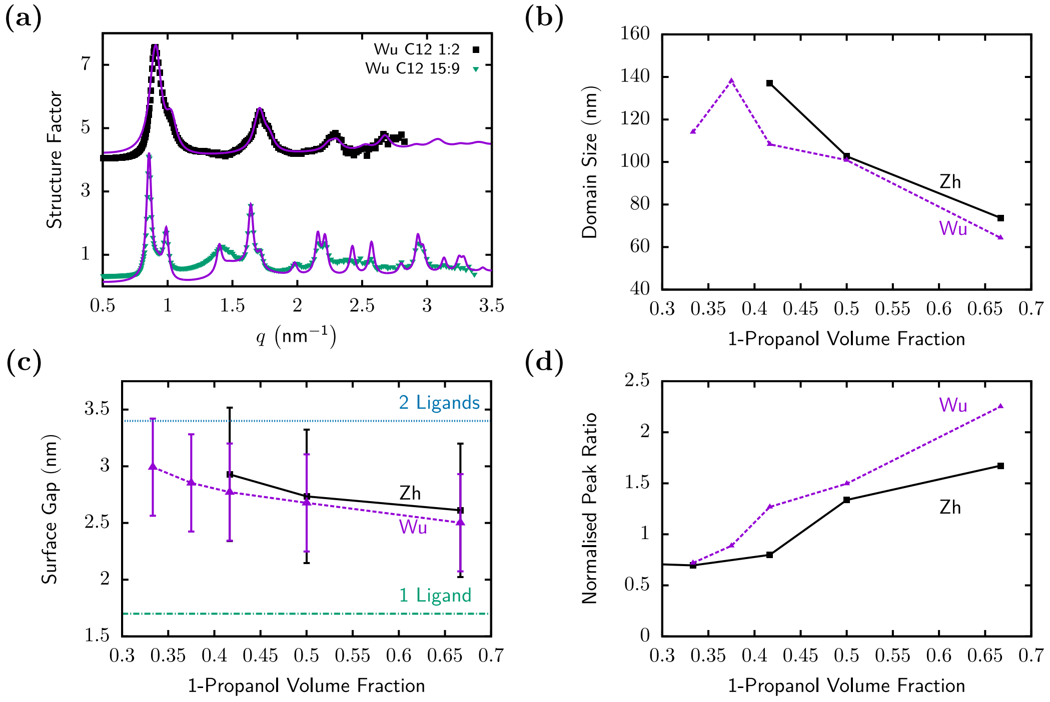

Figure 3.12.: (a) Examples for typical fit results. The upper curve is offset by 4. (b) Agglomerate domain sizes calculated from the fitted peak widths for different 1-propanol concentrations. (c) Smallest surface gap between particles, calculated from the centre-to-centre distance of next neighbours in the fcc lattice for different 1-propanol concentrations and the core radii (table 3.1). (d) Ratio of the measured intensity of the (111) and (311) peaks, normalised with the theoretical value.

From the position of the fitted structure factor peaks, the centre-to-centre distance d_s of neighbouring particles was calculated with eqs. (3.2) and (3.3). For all observed concentrations, the particle distance slightly decreased with increasing 1-propanol content. With the radius of the metal core (table 3.1) the surface gap at the closest approach between two particles d_s was calculated (fig. 3.12 (c)). The error bars were dominated by the particle size distribution width, which enters through the subtraction. The estimated length of dodecanethiol (1.7 nm) and two dodecanethiol molecules is plotted as horizontal lines for reference. For all measured concentrations, the closest surface separation was between one and two ligand lengths (see fig. 3.13 (b) for a sketch). The difference between the d_s for “Zheng” and “Wu” particles was negligible. For both particle types, the interparticle gap slightly decreased when increasing the 1-propanol content.

The height of the individual peaks was adjusted during fitting, although the theoretically expected height ratios are known for a given lattice constant. For fig. 3.12 (d) the ratio between the height of the measured (111) and (311) peak was normalised with the theoretical value for the particular lattice constant to yield the normalised ratio c_n. Values smaller than 1 indicate a reduced height of the (111) compared to an ideal fcc superlattice, whereas values larger than 1 imply excess scattering at lower q. The values for both particles increased with increasing 1-propanol concentration, i.e. for increasing solvent polarity, the (111) peak disproportionately grows compared to the rest of the pattern.

3.4.2. Discussion

The results presented in fig. 3.9 verify the findings from the previous project as presented in section 1.2.3.3. At 35 °C, AuNPs stabilised with dodecanethiol crystallised in a 3D superlattice upon addition of an equal volume of 1-propanol. The strong redshifted portion in the UV/Vis spectra represents further evidence that the particles form an agglomerate.

The structure factor peaks could be indexed as an fcc pattern. This proves two points that were left as open questions from the previous project (section 1.2.3.3).

Ordered nanoparticle supercrystals, prepared by precipitation with 1-propanol, adapt a fcc superlattice. The fcc lattice is a commonly found superstructure for hard sphere assemblies [127] and has been shown to minimise the free energy of the assemblies [128, 129]. While the fcc structure has therefore been the most probable candidate for the structure of ordered agglomerates grown by rapid destabilisation so far (also based on the TEM studies on the electron transparent supercrystal edges), this study gives the *first proof for a fcc superstructure produced by rapid destabilisation.*

Already after 5 min of growth, static fcc nanoparticle superlattices form in suspension. Based on the TEM results from the previous project, the presence of the superlattices could only be shown for precipitates with 2 h growth time that were dried and put under the high vacuum inside a TEM. Preliminary TEM experiments with aliquots taken earlier, e.g. after 10 min of agglomeration time, actually were not able to detect any ordered agglomerates. Conversely, the domain size (which represents a *lower* boundary for agglomerate size) was already in the range of 100 nm after 5 min, a size that is feasible to find in TEM images. *The presence of superlattices after 5 min could be shown for the first time.*

The structure peak positions accord well with the expected positions of a fcc lattice with a cubic lattice constant of $a = 12.44\,\mathrm{nm}$. The ratios between peak heights display non-negligible difference compared with theoretical values. Especially the (111), (200) and (220) peaks are obviously aberrant. The variation due to the form factor minimum does not explain the exaggerated height of the first two peaks compared to the rest of the pattern. *The increased height of the first two peaks could be explained by an additional contribution of an amorphous scattering peak, as explained in fig. 3.16.*

For otherwise identical process conditions, the 1-propanol volume fraction and hence the solvent quality for the ligands[5] determines the quality of the superlattices. The structure factor fits show that the ordered superlattice domains are largest[6] around 1-propanol volume fractions of $f = 0.4$ (15:9 and 7:5). Above and below this concentration range, the ordered domain size decreases and the structure peaks are less well-defined.

Below a threshold volume fraction $f \sim 0.3$ no agglomeration signal was detected (at least for “Zheng” particles). In this case the Flory parameter χ is likely smaller than $\frac{1}{2}$ and the interaction is too repulsive to allow agglomeration (see eq. (1.4)). A rough estimation based on the parameters from [23] suggests that the interaction turns attractive for a 1-propanol volume fraction between $f = 0.25$ and $f = 0.33$. This implies that due to the absence of agglomeration directly below the critical value (3:1), the van der Waals attraction does not significantly contribute to the interaction that is responsible for agglomeration. *The superlattices display the largest domain size at a 1-propanol volume fraction of* $f = 0.4$.

This behaviour is corroborated by the optical measurements. When the spectra are interpreted as the sum of a single particle and a redshifted agglomerate contribution, the contributions are most separated around $f = 0.4$ and show less pronounced superlattice contributions at the other volume fractions.

In fig. 3.9 especially the (111) and (200) peak height appeared too large compared to the rest of the structure factors. With the normalised $\frac{(111)}{(311)}$ peak ratio it could be shown that the first peaks disproportion grows with increasing solvent polarity. The q range of the first superlattice peaks ($q \sim 0.8\,\mathrm{nm}^{-1}$) coincides with the expected nearest neighbour peak of an amorphous agglomerate structure (see eq. (3.5)). The increasing relative intensity of the superlattice peaks in this range is likely induced by the nearest neighbour scattering of a growing portion of agglomerated sample that exhibits only close range order. This explanation also agrees with the decreasing size of the ordered domains. It would imply that a portion of the particles that are not incorporated in a regular superlattice form a glasslike agglomerate,

---

[5] In the probed range of volume fractions, the Hildebrand solubility parameter is proportional to the volume fraction and the 1-propanol fraction is a direct measure for solvent quality.

[6] Alternatively it would be possible to determine the agglomerate size from the Porod oscillations caused by the agglomerate shape. The minimum is expected around $q = \frac{4.493}{D}$ (see eq. (A.5), [45]) and was not resolved here due to the limited minimum $q \sim 0.06\,\mathrm{nm}^{-1}$.

giving rise to the additional amorphous part of the scattering pattern. Similar variations in superlattice peak heights have previously been attributed to disordered contributions and sensitivity variations due to the form factor oscillations [45]. The detailed partitioning of ordered and disordered portions, e.g. whether ordered and disordered agglomerates form as separated bodies, or whether ordered and disordered coexist as ordered crystallites joined by disordered grain boundaries, can not be resolved based on the results presented here. Additional studies with better low q resolution could resolve the size of the surface of the agglomerates and help to refine their structure.

For 1-propanol fractions below $\sim f = 0.4$, the peak ratio continuously decreases to a value below the theoretical value. This marks the transition from a situation where the pattern is dominated by the ordered superlattice to the case where single particles dominate the scattering and the peak ratio is not a good measure due to the small superlattice peak compared to the single particle bump (compare figs. 3.4 and 3.11).

The general trend in the experiments with ethanol as polar solvent was the same (see appendix B.1). For a reduced polarity, the superlattice appeared better defined. This indicates a reduced amorphous fraction, as it is exemplified by the decline of the normalised $\frac{(111)}{(311)}$ peak ratio from 1.2 to 1.0.

The results from the 1-propanol experiments are not directly transferable to the ethanol experiments. When comparing for instance the structure at $f = 0.5$ for ethanol and 1-propanol, the agglomerates produced by adding ethanol exhibit larger supercrystalline domain size, smaller normalised peak ratio and a stronger superlattice contribution in the absorbance spectra. So while all available measures indicate improved superlattice quality for the ethanol-treated agglomerates, the argument of increased attraction for lower solubility impeding ordered agglomeration would suggest otherwise. The Hildebrand solubility parameter of a 1:1 mixture of dispersion and polar solvent is $\sim 1\,\%$ higher for ethanol (at $25\,°\mathrm{C}$, $\delta_{\mathrm{EtOH}} = 2.62 \times 10^4\,\sqrt{\mathrm{Pa}}$ and $\delta_{1-\mathrm{prop}} = 2.44 \times 10^4\,\sqrt{\mathrm{Pa}}$ [24, 130]) and should therefore lead to less defined superlattices. *When comparing different polar solvents as agglomeration agent, there are important effects beyond the solubility expressed by Hildebrand solubility parameters.* A different microscopic interaction between the ligand and solvent molecule would be conceivable, e.g. differences in the intercalation behaviour. Further studies would be necessary to illuminate the solvent-specific effects.

The driving force for agglomeration is the decreasing solubility of the ligands in the increasingly polar solvent. There exists a threshold solvent polarity that has to be overcome to induce agglomeration (see previous paragraphs for an estimate). In the light of the previous results (section 1.2.3.3), it appears likely that the results presented here can be understood in the framework of mobility and interaction.

While the attractive interaction is increased due to the reduced solubility of the ligands, there has to be a change in mobility to explain the decreasing domain size for increasing solvent polarities:

- One possibility are interparticle jamming effects. If the agglomeration rate, which is controlled by the interaction strength, becomes too large, incoming particles could prevent structural rearrangements of the particles already attached to the agglomerate. This way, the resulting structure would be ordered less.
- Another source for mobility variations could be solubility-induced changes in the ligand layer structure, similar to the temperature-induced changes found in section 1.2.3.3. The solubility reduction of the ligands likely results in a contraction of the ligands (see also next paragraph). This could reduce the flexibility of the ligand layer, which is needed to allow the layer to act as a lubricant between particles.

The more polar the solvent, the denser the packing of particles in the superlattice becomes. While the error bars for the surface gaps appear large, this trend is robust. Two effects related to the ligand solubility contribute to this behaviour:

- Interdigitation of the ligand layers of neighbouring particles allows surface distances smaller than two ligand lengths, as described in the next paragraph. The reduced solubility of the ligands in the solvent induces a stronger attractive interaction that pulls the particles together and increases the degree of interdigitation.
- An increased polarity can induce an increasing collapse of the ligand layer (see previous paragraph), effectively reducing the particle dimensions and allowing closer approach of the particles. Collapsed layers allow less interdigitation, so the actual direction of this change is unclear.

The role of the ligand coverage on the particle surface can not be deduced from the results.

Ligand chain interdigitation accounts for the observed surface gap. The ligands are attached to the particle surface via their thiol end group. The remaining alkyl chain points in radial direction into the surrounding medium. Due to the curvature, the area fraction of ligands on a spherical shell around the surface is larger close to the surface, as illustrated in fig. 3.13 (a). If the area density at a radial distance R_i is ρ_i, the density at distance R_o is

$$\rho_\mathrm{o} = \frac{R_\mathrm{i}^2}{R_\mathrm{o}^2}\rho_\mathrm{i}. \tag{3.7}$$

For the C12-stabilised “Wu” particles, this results in a density reduction of more than 40 % from the surface to the sketched spherical shell that is 1.3 nm above the surface and corresponds to the smallest gap observed in the measurements (see fig. 3.12 (c)). In fig. 3.13 (b), two C12-stabilised “Wu” particles in closest approach are sketched. The figure illustrates that even at this closest approach, the cone enveloping the overlapping parts of the monolayers is relatively small.

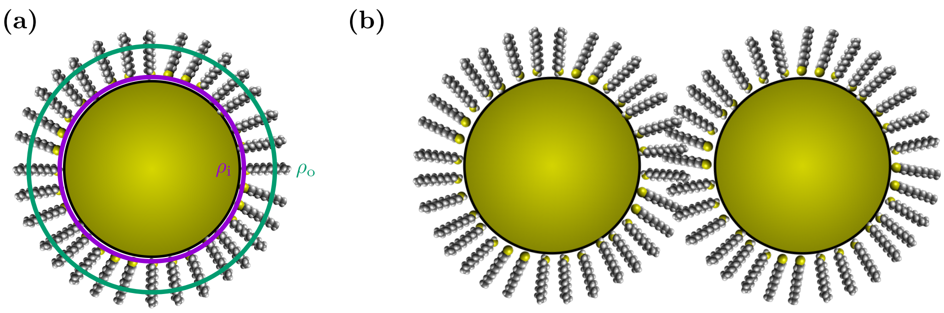

Figure 3.13.: (a) The ligand density in spherical shells around the core (ρ) depends on the shell radius. (b) Ligand layer interdigitation flattens the density profile along the centre-to-centre axis.

The differences between “Wu” and “Zheng” particles with equal ligands are relatively small. The “Wu” particles displayed slightly better defined superlattice peaks in the scattering patterns and a larger redshifted part in their absorbance spectra compared to the “Zheng” particles. The effect is small, especially when comparing the processed results. It could be explained by the smaller polydispersity of the “Wu” particles compared to the “Zheng” particles ($\sim 7\,\%$ versus $\sim 10\,\%$), since polydispersity above 8 % is known to impede the formation of ordered superlattices [131–133]. The polydispersity could be related to the rivalling formation of amorphous agglomerate fractions. Whether the ligand layer structure is different due to the different synthesis protocols can not be assessed from the results.

In summary, two simple statements can be made:

- If the solubility of the ligands in the solvent is decreased, the superlattices grow less ordered.
- The gap between particles decreases when increasing the solubility mismatch.

Both findings are readily explained by the solubility of the ligands. At higher polarities, the ligand chains are less soluble in the continuous phase. The chains in a poor solvent collapse to a more compact conformation, whereas they increasingly extend in solvents with increased solubility [40, p. 164]. A more compact layer allows closer approach, explaining the smaller gap. On the other hand, more compact monolayers are expected to be more rigid. Therefore the compact layers could induce jamming and impede reorganisation of the particles attached to a random site of the agglomerate. Conversely, the layers in the low polarity solvent are more flexible and could actually lubricate the interface between attached particle and agglomerate, promoting reorganisation in an ordered superlattice. Solubility alone does not explain the difference between 1-propanol and ethanol precipitation, the key difference could not be clarified here.

It has to be noted that a certain degree of polarity and the associated solubility reduction (the solubility parameter of the solvent should be larger than the value of the ligand) is necessary to induce agglomeration. Without polar solvent the dispersions are stable and do not agglomerate.

3.5. Temperature Variation

The presented data so far was taken at temperatures above the expected minimum temperature for the formation of ordered agglomerates T_C (based on section 1.2.3.3). In this section, the boundary between the ordered and disordered region of the pseudo phase diagram in fig. 1.4 is crossed by variations of the experimental temperature and the stabilising ligand length. Agglomeration was induced by mixing equal volumes of 1-propanol and the respective particle dispersion. To emphasise the structural information, the SAXS data is presented as structure factors here. The flow rate of 1-propanol and the dispersion were set to $2.5\,\mu\mathrm{L\,s^{-1}}$, resulting in a total flow rate of $5\,\mu\mathrm{L\,s^{-1}}$ and the corresponding agglomerate growth times of approximately 180 s for the SAXS and 90 s for the UV/Vis measurements.

3.5.1. Results

The experiments presented here are classified according to the stabilising ligand. The difference between “Zheng” and “Wu” particles is introduced in section 3.2.1. Additional results on the temperature-dependant agglomeration of “Wu 2” particles are described in appendix B.2.

3.5.1.1. Dodecanethiol

The crystallisation temperature for C12-stabilised particles is expected to be below 0 °C and was thus not achievable with the water based temperature control employed here. Hence all C12 measurements were performed at temperatures where the formation of ordered agglomerates is expected (see fig. 1.4).

The structure factors and the respective model functions of all three C12-stabilised batches agreed reasonably well (fig. 3.14 (a)). The shape of all curves were very similar. The most noticeable difference was the increasing height of the structure peaks from bottom to top. Furthermore the peak position was slightly different, consistent with the small variation in core size of the particular batches (table 3.1). The difference in peak widths was difficult to assess visually due to the difference in heights.

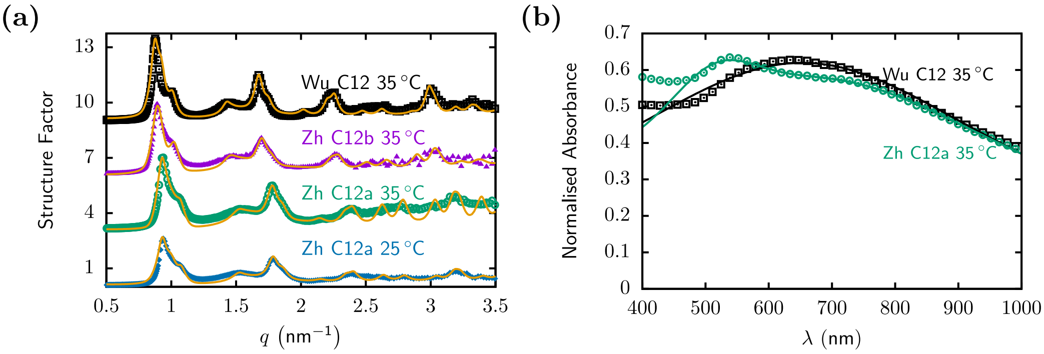

Figure 3.14.: (a) Structure factors of "Wu C12" and "Zheng C12a" and "C12b" particles and their model functions, each with an offset of +3 beginning from the bottom curve. (b) Available UV/Vis corresponding to the measurements in (a). The spectra are normalised with the single particle plasmon peak height.

Technical issues impeded the acquisition of absorbance spectra for "Zheng C12b" particles at 35 °C and the "Zheng C12a" particles at 25 °C. Only the absorbance for "Wu C12" and "Zheng C12a" at 35 °C, normalised by the absorbance maximum of the primary particles, are therefore presented in fig. 3.14 (b). While the shape of the spectrum resembled a single broad peak for the "Wu" particles, a single particle peak and a second, redshifted contribution could be distinguished in the spectra of the "Zheng" particles. At higher wavelengths, both curves converged. The single particle contribution was more dominant for the "Zheng" particles, the reasons remain to be discussed.

To illustrate the differences, the key parameters of the fits are compared in table 3.2. In the probed temperature range, the superlattice structural parameters did not change significantly, except a slight increase in the size of ordered domains L of the "Zheng C12a" particles at higher temperatures. Although the changes are insignificant, the weak trend in the surface gap d_s correlates to the core size. The normalised ratio of the (111) and (311) structure peaks c_n differed slightly for the particular batches. The similar-sized batches also showed a similar c_n value.

Table 3.2.: Fit results for different batches of C12-stabilised particles.

Sample	d_s (nm)	L (nm)	c_n
Wu C12 35 °C	2.8 ± 0.2	101	1.43 ± 0.02
Zh C12b 35 °C	2.7 ± 0.3	103	1.44 ± 0.02
Zh C12a 35 °C	2.6 ± 0.3	97	1.53 ± 0.02
Zh C12a 25 °C	2.6 ± 0.3	83	1.50 ± 0.02

3.5.1.2. Hexadecanethiol

The agglomeration of hexadecanethiol-stabilised "Zheng" and "Wu" particles was observed (see fig. 3.15) at different temperatures above and below $T_\mathrm{C} = 43 \pm 3\,°\mathrm{C}$, the crystallisation temperature taken from fig. 1.4. At lower temperatures, the superlattice peaks were increasingly broadened; they gradually disappeared. At 25 °C, a single broad peak below $1\,\mathrm{nm}^{-1}$ was the main feature of the structure factors. The structure factors at 25 °C were fit with a modification of the superlattice structure factor described in section 3.2.4.2 (see fig. 3.16 (a)). The fcc peaks were largely damped by setting the FWHM to 10 and a Pseudo-Voigt peak (see eq. (2.3)) was added to account for the amorphous peak (see eq. (3.5)).

With the resulting amorphous peak positions, centre-to-centre distances of $d_\mathrm{ctc} = 8.7\,\mathrm{nm}$ for the "Zheng C16" particles and $d_\mathrm{ctc} = 9.2\,\mathrm{nm}$ for the "Wu C16" particles were found. Taking into account the average core size (table 3.1), this corresponds to surface separations of 2.3 nm and 3.2 nm respectively.

For increasing temperatures, the fcc superlattice peaks gradually arose for both particle types. At equal temperatures, the superlattice peaks of the "Wu" particles were better defined compared to the "Zheng" particles. At 45 °C, the superlattice peaks for the "Wu" particles were 50 % higher compared to the "Zheng" peaks. To further quantify the agglomerate morphology, the structure factors were fitted with an extension of the aforementioned model function. As discussed in section 3.4, the height ratios between the peaks are influenced by several factors which are difficult to quantify. The height of the individual peaks can therefore be adjusted independently, but their positions are still determined by the known fcc lattice and they still share a common FWHM. To account for the error caused by the sensitivity changes at the minima of the form factor, a peak with adjustable height with the position and inverted shape of the minimum is added. Possible amorphous structure factor contributions are modelled by adding another adjustable peak in the vicinity of the (111) and (200) peaks. With these additions, the model function typically fitted the structure factors reasonably well (fig. 3.16 (a)). The cubic lattice constant a of the fcc superlattice was determined from the superlattice peak positions. With a and the particle radii (table 3.1) the average surface separation d_s of the particles

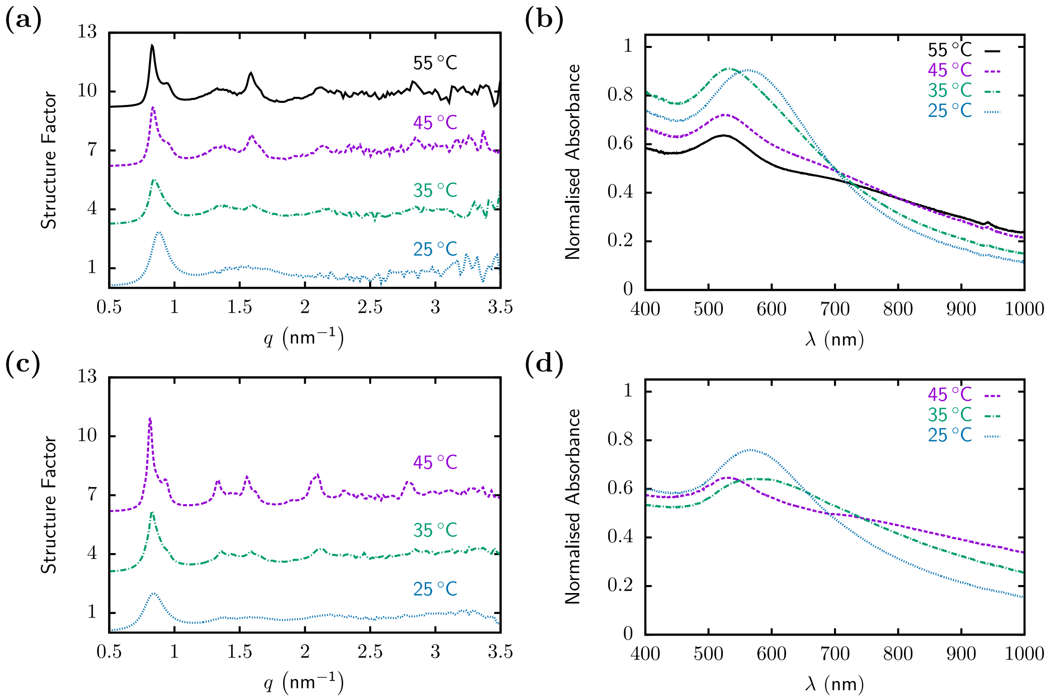

Figure 3.15.: Results for agglomeration on AuNPs stabilised with hexadecanethiol at different temperatures. (a) SAXS structure factors and (b) UV/Vis absorbance spectra for “Zheng C16” agglomerates at different temperatures. (c) SAXS structure factors and (d) UV/Vis absorbance spectra for “Wu C16” agglomerates at different temperatures. To enhance visibility the structure factors are plotted with a constant offset of 3 between them, beginning from the lowermost curve. The absorbance values were divided by the maximum absorbance of a stable dispersion with equal concentration for better comparability.

in the lattice was calculated and compared to the ligand length in fig. 3.16 (b). For both particle types, the surface gap lay between the length of one and two ligand molecules. The error bars were dominated by the uncertainty in particle core size.

Overall, d_s of the “Zheng” particles was 10 % smaller than for the “Wu” particles. In the superlattices, the interparticle distance slightly increased with temperature. The variation between the distance in ordered and disordered agglomerates was insignificantly small for the “Wu” particles. The interparticle gap in the glass-like agglomerates sharply dropped for the “Zheng” particles. A simplified, but scaled sketch of neighbouring particles in a close packed plane for both particle types

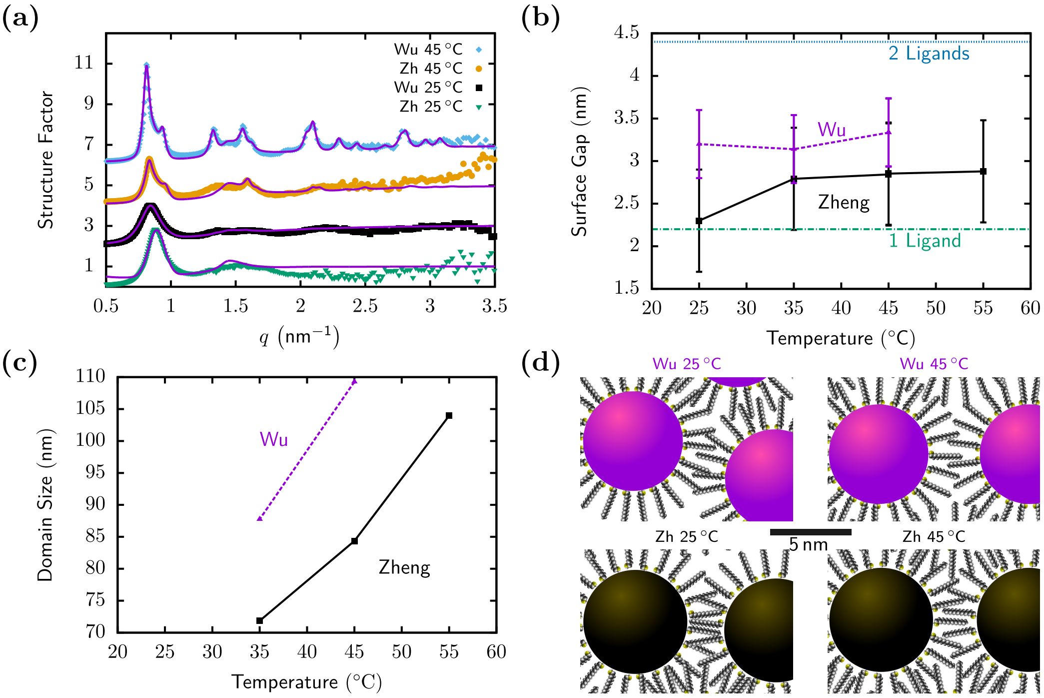

Figure 3.16.: (a) Typical fits of the structure factors with the modified structure factor model (purple lines) and the measured structure factors. The curves are offset by 2 beginning from the lowermost curve. (b) Smallest surface gap d_s between next neighbours in the fcc lattice for different temperatures. (c) Ordered domain sizes for different temperatures, calculated from the peak width obtained by fitting. (d) 2D sketch of next neighbours in the different superstructures.

at different temperatures (fig. 3.16 (d)) reveals the different volume between the particle cores available for the ligand layers.

From the width of the peaks of the model function, the size of the ordered domains was calculated (fig. 3.16 (c)). At higher temperatures, the ordered domains were larger. The “Wu” particles exhibited larger supercrystalline domains at lower temperatures compared to the “Zheng” particles, which confirms the visual impression that the superlattice peaks were better defined.

The absorbance spectra (fig. 3.15 (b) for “Zheng” and (d) for “Wu” particles) drastically changed upon temperature changes. At lower temperatures, the spectra could be described by a single, broad peak that is redshifted compared to the single particle peak. The spectra at higher temperatures were composed of two contributions. They exhibited a peak similar to the single particle peak (but weaker) and a second, broad contribution at lower energies. The absorbance values at high wavelengths distinctly increased with increasing temperature. Modelling the spectra with two peaks, as in fig. 2.2, did not reveal a clear trend here when fitting the data. The normalised flocculation parameter decreased with increasing temperature, likely because the superlattice-related redshifted part of the adsorption increasingly lay above the maximum accessible wavelength.

3.5.1.3. Octadecanethiol

Octadecanethiol is the longest ligand employed here. This shifts the relevant transition temperatures to relatively high values (see fig. 1.4). The particles were handled only above 30 °C and the T_c line was crossed by measuring at 45 °C and 60 °C (fig. 3.17). The measurements were complicated by leaking fittings at higher temperatures. Even after careful tightening of all connectors, air leaks occurred at temperatures above 50 °C. The presented data were carefully selected and averaged from raw data that contained no bubbles. The main feature of the structure factors (fig. 3.17 (a)) was a single amorphous peak. Superlattice peaks were not observed for both temperatures. The surface gap d_s between next neighbours, calculated from the amorphous peak position with eq. (3.5) and table 3.1, was 3.3 ± 0.6 nm. It fell again between the length of one (2.45 nm) and two (4.9 nm) ligands.

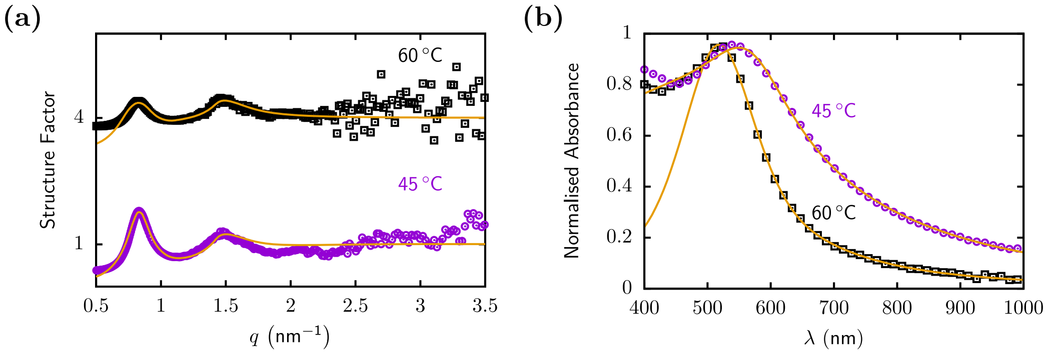

Figure 3.17.: (a) Fits of the structure factors of agglomerating “Zheng C18” particles at different temperatures with the modified structure factor model (yellow lines) and the measured structure factors. The curves are offset by 3 beginning from the lowermost curve. (b) UV/Vis spectra with fits of the samples from (a). The spectra are normalised by the peak height of the corresponding single particle measurements.

The UV/Vis spectra (fig. 3.17 (a)) resembled the spectra of amorphous agglomerates from the previous part. A broad, redshifted peak was found for the measurement at 45 °C, while the high temperature measurement only developed a small redshift compared to the single particle measurement. This was also reflected in the normalised flocculation parameters $P_\mathrm{n} = 1.2$ for 60 °C and $P_\mathrm{n} = 2.5$ for 45 °C.

3.5.2. Discussion

The agglomerates from the different C12-stabilised particles are structurally very similar. All particle batches formed superlattices upon destabilisation at the observed temperatures. The increase in domain size upon heating for the "Zheng C12a" particles suggests that higher temperatures facilitate the formation of superlattices. This agrees with the solubility argument from section 3.4.2: *Better solubility (as it is caused by higher temperatures) leads to better defined superlattices.*

The fraction of amorphous agglomerates, estimated by c_n, is only weakly influenced by temperature. When neglecting other effects, the slightly larger cores of the "Zheng C12b" and "Wu C12" particles appear to reduce the formation of amorphous agglomerates. While the differences in surface gap d_s are insignificant, the trend could be explained by the different sizes as well. The smaller curvature of the larger cores of the "Wu" particles increases the effective ligand density at the outer border of the ligand layer and therefore would allow less interdigitation compared to the "Zheng C12a" particles.

The different morphology of the UV/Vis spectra of "Wu" and "Zheng" particle agglomerates could result from the larger amorphous agglomerate fraction of the "Zheng" particles (as indicated by the larger peak ratio). The superlattice resonances are less pronounced and the single particle signal is therefore better visible for the "Zheng" particles.

The structure of the agglomerates for C12-stabilised particles could be tuned by changing temperatures. The findings of the previous project (section 1.2.3.3) are confirmed: At high temperatures, the particles form regular superstructures with superlattices ordered on long ranges above 100 nm. At lower temperatures only close range order can be found. Ordered superstructures represent a free energy minimum [128, 129]. Disordered structures form when superlattice growth is suppressed by kinetic effects, often due to strong short-ranged attraction [134] as explained in section 1.2.3.3.

Surprisingly, ordered superlattices appear gradually with rising temperatures. This gradual emergence gives new insights in the basic principles of superlattice formation. The current understanding of the structure formation process during rapid precipitation (as outlined in section 1.2.3.3) is that liquid ligand monolayers promote the formation of ordered superlattices above a well-defined melting temperature. The gradual manner in which the peaks appeared here suggests that the monolayer melting appears gradually likewise.

At least a portion of molten ligands are present over a large temperature range. Simulations on CdS nanorods passivated with alkyl chains showed a similar broadening of the ligand layer melting on curved surfaces [135]. The transition was smeared to a temperature range of up to 20 K.

An additional factor contributing to the range of the transition temperature could be the finite width of the particle size distribution. In other simulation studies, a dependence of the melting temperature on the core size was found [136]: Compared to planar layers, the melting temperature of monolayers on a particle is reduced up to 60 K. For decreasing particles sizes the melting temperature decreases. The relatively narrow size distribution of the particles used suggests that the polydispersity effect can not be the only contributing factor. *The gradual appearance of ordered superlattices with rising temperatures results from the smeared phase transition due to curvature and the particle size distribution.*

The size of the ordered domains increased with temperature. The effect of temperature is very similar to the effect of changing the solvent polarity (see section 3.4.2). Increasing the temperature increases the solubility of the ligand backbones, and therefore leads to larger ordered domains.

The surface gap between neighbouring particles appears to vary systematically with temperature, even though the statistical uncertainty due to the particle polydispersity is relatively high. This behaviour again resembles the solvent-induced changes in the interspace between the gold cores in a superlattice. Higher temperatures, similar to lower polarities, lead to a better solubility and result in a smaller interspace volume.

These relatively small differences of the interspace volume of “Zheng” and “Wu” particles appear much more pronounced when visualised with a simple sketch as in fig. 3.16 (d). Especially for disordered agglomerates, at 25 °C, the ligands of neighbouring “Zheng” particles appear to almost contact both particle surfaces, when sketched as perpendicular to the surfaces. The interspace for the “Wu” particle appears more commodious in the sketch. The direct effect of different polydispersities (10 % vs. 8 %) on the packing efficiency (due to favourable combinations of differently sized neighbours), and therefore on the apparent surface gap, is probably negligible.

The difference in surface gaps for “Wu” and “Zheng” particles could be related to the ligand layer structure. In fig. 1.1 it was already shown that AuNPs are not perfectly spherical on the microscopic scale. Faceted particles would allow tilted ligand bundles on each facet, a phenomenon not represented in the simplified sketch[7]. Tilted layers would allow for closer approaches [137]. Due to the different syntheses, differences in faceting of “Zheng” and “Wu” particles are possible.

Another possibility would be changes in ligand density. Low density ligand layers allow for higher degrees of interdigitation and enable smaller surface gaps likewise. Lower density layers will surely permit stronger tilting

Both assertions, different faceting or different ligand densities across different syntheses, could not be backed by further data in the frame of this study but are possible explanations for different surface gaps. The surface gap was not the only structural feature differing between the “Zheng” and “Wu” particles.

Overall the “Wu” particle superstructure appears better defined compared to the “Zheng” particles at equal temperatures. This is obvious from the sharper peaks in fig. 3.16 (a) or the consistently larger superlattice domain sizes in (c). At equal conditions, the “Wu” particles display a larger tendency to form ordered structures.

Polydispersity impedes superlattice formation, a result already known from early theoretical studies [131]. Above a polydispersity threshold of $\sim 8\,\%$, the particles tend to segregate in different fractions before crystallising [31, 133]. This segregation might however be suppressed by a glass transition [132, 138].

A larger amount of amorphous agglomerate formation for the “Zheng” particles due to the polydispersity could compete with superlattice formation and lead to reduced ordering compared to the more monodisperse “Wu” particles.

Polydispersity is an additional explanation for differences in order formation across the synthesis methods. Whether the microscopic surface structure or polydispersity is the dominant reason for differences between the agglomeration of “Zheng” and “Wu” particles can not be decided based on the results presented here.

Increasing the core size increases the critical temperature of agglomeration. The “Wu 2” particles stabilised with hexadecanethiol still lacked superlattice peaks at 35 °C, a temperature at which “Zheng” and “Wu” particles, stabilised with C16, already exhibit distinct higher order peaks as it is highlighted in (fig. B.3 (a)). Similarly, the redshifted superlattice contribution in the UV/Vis spectra increased for smaller radii.

When comparing the patterns of “Wu” and “Zheng” particles at equal temperatures (fig. 3.16 (a)), the superlattice peaks of the smaller “Wu” particles are better defined, as the domain size illustrates (fig. 3.16 (c)).

The size dependency of the formation of ordered superlattices could be related to the already mentioned dependency of the ligand layer melting temperature on the core size: For larger particles with smaller curvature, the ligand layer melting

---

[7] Tilted bundles are presumably concomitants of freezing ligand layers.

temperature is larger [136]. Likewise, the ligand layer is less effective at lubricating contacts between particles and the resulting superlattices are less ordered for larger particles when compared to smaller particles at equal temperatures.

Alternatively, the van der Waals attraction also increases for larger cores. Since both effects affect the attractive force in the same direction, it is difficult to assess their relative importance, but safe to assume that both effects play a role.

The structure peaks can be attributed to static structures. The main feature of the amorphous structure factors is a single peak at q values smaller than the position of the first form factor minimum. In contrast to the fcc pattern of the ordered superlattices, a single peak does not necessarily imply that the sample is an arrested state and formed a static agglomerate. Already for the most simple interaction potential, the hard sphere potential, the structure factor of the interacting, unagglomerated dispersion exhibits a peak [139, 140].

A classical criterion to distinguish frozen, agglomerated states from interacting liquid like states is the Hansen-Verlet freezing rule [141, 142]. According to the Hansen-Verlet criterion, the first structure factor peak amplitude should exceed 2.85 for a solid structure.

The amorphous agglomerate structure factors observed at 25 °C for the “Zheng” and “Wu” particles are too small to satisfy the Hansen-Verlet condition. Conversely, the UV/Vis spectra exhibit a distinct redshift, a feature generally attributed to the formation of agglomerates. Additionally, most (111) peaks observed so far do not exceed the threshold amplitude either, although the mere presence of the fcc patterns clearly proves that static agglomerates have formed.

The resolution is probably a persisting fraction of dispersed particles still present in the agglomerating sample. By calculating the agglomerate structure factors through division of the scattered intensity with the measured effective form factor, it is implicitly assumed that the particle amount in the agglomerate is equal to the bulk concentration in the stable dispersion. As long as there is a finite fraction of dispersed particles not attached to agglomerates, the divisor will be too large and the calculated structure factor has a smaller magnitude than the actual structure factor of the agglomerates.

Since it has to be assumed that during all the measurements presented here, a certain fraction of particles remains dispersed, the amplitude of the structure factors is underestimated to a certain extent in all cases. The actual fraction of dispersed particles is not directly accessible from the measured data.

Evidence for superlattice formation of octadecanethiol-stabilised particles could not be found in this study. No superlattice peaks could be distinguished in the measurements presented here. The structure peak and the flocculation parameters were much smaller in magnitude for the high temperature measurement compared to the lower temperature measurement, indicating a significantly reduced degree of agglomeration in the observed sample. The reduced degree of agglomeration could be induced by the increased ligand solubility due to the higher temperature. Early studies on the ligand layer structure of smaller monolayer protected nanoparticles found a strong intercalation of solvent molecules between C18 ligands that could block the formation of agglomerates at higher temperature [50]. However, due to the air leaks at 60 °C, reliable conclusions on the high temperature measurements are impossible.

Ligand solubility alone does not explain all results. When considering only results for a single ligand length, the solubility of the ligands could explain the temperature and polarity dependence of the agglomerate structure, since better solubility in the polar solvent leads to better defined superlattices. When comparing different ligands it becomes clear that longer ligands require higher temperatures to form ordered agglomerates. The solubility argument would actually suggest the opposite behaviour, since longer ligands have larger solubility parameters, the solubility difference to the polar solvent and therefore the ligand-mediated attraction is actually smaller. A ligand-specific effect, likely the phase transition described in section 1.2.3.3, would fill the obvious gap in the model.

3.6. Early Stages of Agglomeration

The majority of the experiments presented so far were performed at a constant total flow rate of $5\,\mu\mathrm{L\,s^{-1}}$, corresponding to delay times of 3 min and 1.5 min for the SAXS and UV/Vis measurements (see fig. 3.2). In this section, higher flow rates are applied to observe younger agglomeration states, with reaction times as small as 1 s.

To asses the earlier stages of agglomeration, the total flow rate of the agglomerating sample was varied from $5\,\mu\mathrm{L\,s^{-1}}$ to $150\,\mu\mathrm{L\,s^{-1}}$. Based on the resulting mean flow velocities and the flow path length, the "average" agglomeration times at the SAXS detector ranged from 1 s to 55 s. The average agglomeration time (corresponding to twice the lower boundary in fig. 3.2) is used in the following to describe the different observed agglomerate stages.

The solvent composition was fixed to a volume ratio of 1:1 between 1-propanol and *n*-heptane for the measurements presented in this section. "Zheng C12a" and "Wu C16" particles were used to observe different particle types. The difference between "Zheng" and "Wu" particles is introduced in section 3.2.1. The temperature was varied to observe the agglomeration process above and below the crystallisation temperature.

3.6.1. Results

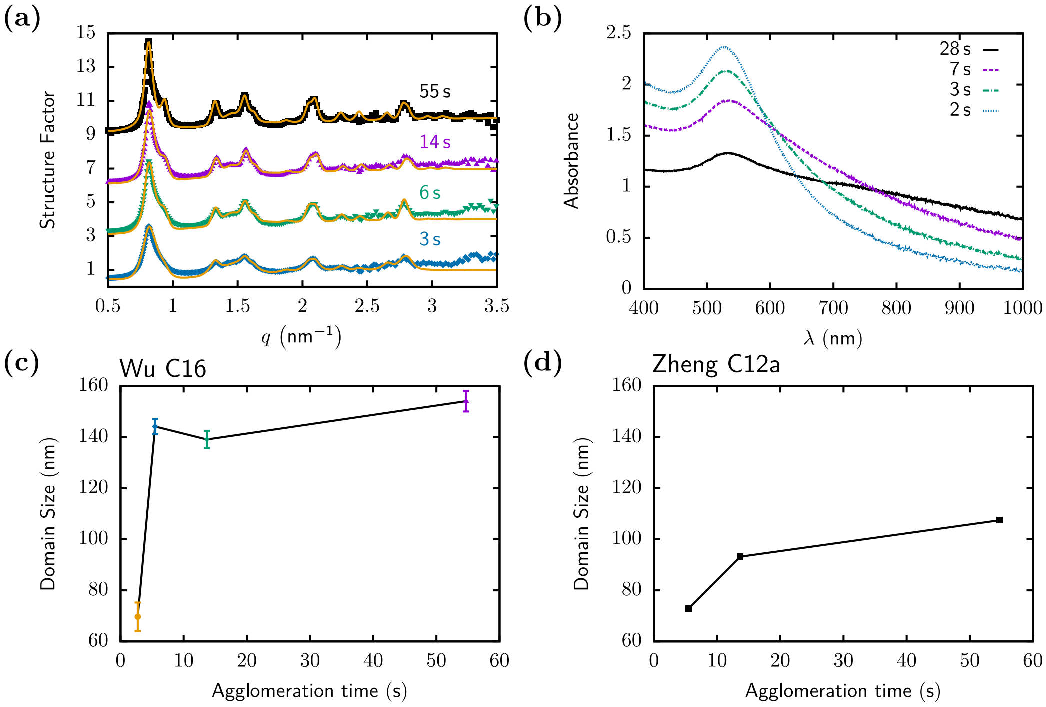

Figure 3.18.: (a) Structure factors of "Wu C16" agglomerates at 45 °C after various growth times, with an offset of 3 between the curves. The fit functions are plotted as yellow lines.(b) UV/Vis absorbance spectra of "Wu C16" agglomerates at 45 °C after various growth times. (c) Supercrystal domain sizes of the "Wu C16" particles, calculated from the fitted FWHM from (a). (d) Supercrystal domain size for equivalent measurements with "Zheng C12a" particles.

The agglomeration of "Wu C16" particles was observed at 45 °C, thereby above the critical temperature for the formation of ordered agglomerates fig. 3.18. The superlattice structure factor peaks, introduced in the previous sections, were visible for all agglomerate ages (fig. 3.18 (a)). Older agglomerates exhibited more pronounced peaks, indicating the progression of agglomeration in the observed time frame.

This was further corroborated by the UV/Vis measurements (fig. 3.18 (b)). As the age of the observed agglomerates progressed, the spectra displayed an increasing redshifted portion, while a small peak in the range of the single particle peak (table 3.1) was retained[8].

A relatively large increase in the superlattice domain size L was observed between 3 s and 6 s (fig. 3.18 (c)). After 55 s the domain size significantly increased, but at a smaller rate compared to the initial step.

The surface gap d_s did not change significantly on the observed time scale. The average gap, $\overline{d}_\mathrm{s} = 3.3 \pm 0.2\,\mathrm{nm}$, was found to lie between the length of one and two ligand molecules.

The normalised peak ratios of the structure factor peaks fluctuated between 1 and 2 without any clear trend in agglomeration time dependence.

The results for “Zheng C12a” particles at 35 °C were analogous. Their superlattice domain size increased likewise with agglomeration time (fig. 3.18 (d)).

The structure factor peaks arose gradually over time. The calculated surface gap in the superlattice, $2.6 \pm 0.3\,\mathrm{nm}$, was again between one and two ligand lengths.

As an example for amorphous superstructures, the agglomeration process of “Wu C16” particles was studied. The structure factors (fig. 3.19 (a)) lacked the superlattice peaks observed at 45 °C. The main feature was a broad peak, characteristic for amorphous agglomeration. The difference between the curves is difficult to discern visually.

The UV/Vis spectra (fig. 3.19 (b)) exhibited a growing redshifted portion. In contrast to the otherwise identical measurements at 45 °C, the shape resembled a single, shifted peak for all times.

The FWHM of the amorphous peak was determined from the peak fits in (fig. 3.19 (a)). The Scherrer equation eq. (3.4), although actually derived for periodic superstructures, was used to estimate an effective size of the agglomerates. The effective size of the amorphous agglomerates (fig. 3.19 (c)) and the domain size of the ordered superlattices (fig. 3.18 (c)) followed a similar curve. After increasing steeply at early stages ($t < 10\,\mathrm{s}$), the growth slowed down.

The average surface gap of next neighbours did not change with time (fig. 3.18 (d)). The average value $d\mathrm{s} = 3.0 \pm 0.2\,\mathrm{nm}$ was found to lie between one and two ligand lengths, but was slightly smaller compared to the value at 45 °C.

---

[8] After increasing continuously with age, the normalised flocculation parameter dropped sharply for the oldest agglomerates. The absorbance due to the superlattice likely extended to wavelengths larger than the measurement range, the values were therefore only partially useful.

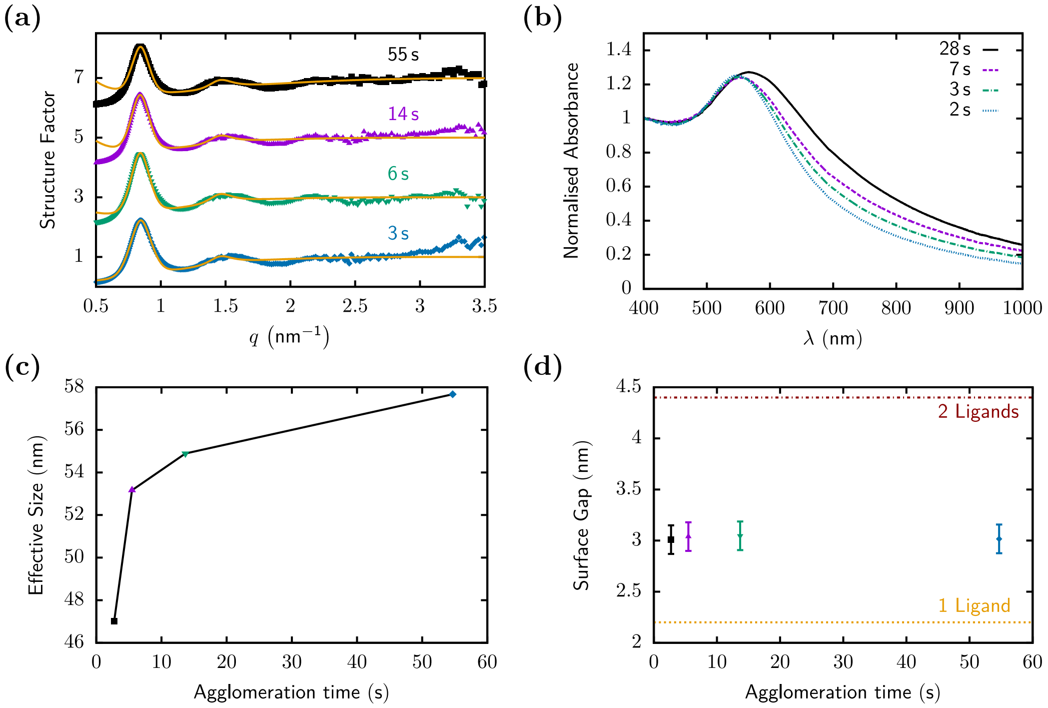

Figure 3.19.: (a) Structure factors of “Wu C16” agglomerates at 25 °C after various growth times, with an offset of 3 between the curves. The fit functions are plotted as yellow lines.(b) UV/Vis absorbance spectra of “Wu C16” agglomerates at 25 °C after various growth times. The spectra were normalised with the absorbance at 400 nm to emphasise the changes in shape. (c) Effective agglomerate sizes, calculated from the fitted FWHM from (a). (d) Surface gap between next neighbours in an agglomerate. Calculated with the Ehrenfest relation and the known core size.

3.6.2. Discussion

The agglomeration progress could be traced by adjusting the flow rate. The domain size of ordered agglomerates grew over time. Under the assumption of single domain agglomerates, which is justified by the TEM appearance of crystallites (see section 1.2.3.3), the domain size directly measures the agglomerate size. For polycrystalline superlattices it should at least be a proxy for the true size.

The decrease in peak width of the amorphous peak can be understood as a measure of agglomerate size too. While a glass-like agglomerate structure does not possess long range translational order, the close-packed nature and the monodisperse particle size entails a certain short range order, leading to a correlation peak in the interparticle distance distribution. The range of this spatial ordering can be expressed as the size L from the Scherrer equation eq. (3.4) [116].

For both types, ordered and disordered agglomerates, the initial growth is fast and slows down at later stages. The curvature suggests diffusion-limited agglomeration (see eq. (1.8)) for all growth curves. Fitting the curves with eq. (1.8), however, yields unrealistically large fractal dimensions $d_\mathrm{f} > 4.0$ for all cases. This corresponds to a slowed down process compared to truly diffusion-limited agglomeration. It is likely a result of the steric stabilisation acting as a barrier (see section 1.2.3.1). *The barrier effect of the steric stabilisation is not strong enough to result in truly reaction-limited agglomeration in the experiments discussed here, possibly as a result of the additional attractive forces mediated by the ligand layer interaction.*

The superlattice structure has formed already after a mean agglomeration time of 3 s. The upper boundary for the agglomerate age corresponding to that flow velocity was 5 s. Consequently, the superlattices observed in this chapter formed after less than 5 s. The domain size for the youngest agglomerates from “Wu C16” particles (∼ 2.7 s agglomeration time) was around 70 nm, corresponding to approximately 300 particles in the average agglomerate (assuming spherical shape and close packing). The youngest agglomerates (∼ 5.5 s agglomeration time) of “Zheng C12a” particles are sized similarly (72 nm). Due to the smaller contour of the particles, this corresponds to approximately 640 particles per agglomerate.

3.7. Summary and Conclusions

The structure of agglomerates prepared by in-flow addition of polar solvents to the originally unpolar dispersion of gold nanoparticles stabilised with a particular alkylthiol, could be controlled by tuning the process parameters

- solvent composition (smaller incompatible solvent fraction increases ordering) and
- temperature (higher temperature increases ordering).

In previous studies, the temperature influence on the agglomeration of particles from a common synthesis method with different ligands was examined. New research objectives here were the influence of the solvent composition, early stages of the agglomeration process and a broader range of particle types.

Adjusting the *solvent polarity* and therefore the solubility of the ligand layer allowed to

- tune the degree of ordering (a smaller incompatible solvent fraction increased ordering due to smaller short-ranged attraction) and
- change the lattice spacing of the particles in the superlattice (increased polarity reduced the lattice parameter by shrinking the layers and increasing the attraction).

Both effects have not been observed before. However they are readily explained by the previously devised solubility-based model.

Temperature could also tune the structure of agglomerates. Increased temperatures improved the size of ordered domains and slightly increased the lattice constant, similar to the solvent-induced solubility changes and could be explained by a temperature-induced change of the ligand solubility.

The improved superlattice quality for increased ligand solubility is related to the short-ranged attraction induced by insoluble ligand layers. Increased short-ranged attraction is known to impede the formation of ordered superstructures [134].

The basic solubility argument however does not explain the variation between different ligand lengths. *The decrease of the ability to form ordered structures for increasing ligand lengths at otherwise identical conditions exposes the ligand layer melting as an additional contribution to the structure formation mechanism.* The ligand-specific temperature dependence is caused by the reduced contact lubrication of frozen layers compared to molten ligands [48] (see also section 1.2.3.3).

The trends in structural changes for agglomerates of particles synthesised by the “Zheng” and “Wu” method were similar for both solvent and temperature variation. While the magnitude of superlattice size and lattice parameter differed slightly, the clear trends indicate the importance of the ligand layer for the agglomeration process.

The monolayer melting transition during temperature variation experiments was partially masked by the convolution of size distribution and agglomerate age distribution effects. *The hydrodynamic dispersion and the fouling effects are the main drawbacks of the flow-based method surfacing in this chapter.*

On the other hand, the stable process parameter control and coupling of different detectors proved effective. The most significant virtue of the flow system is the possibility to observe early stages of agglomeration with virtually unlimited integration times. This allowed to demonstrate for the first time that the superstructure previously found after 2 h is an *fcc structure that already forms after* 5 s and grows continuously. The superlattices displayed a more strongly redshifted contribution in their absorbance spectra compared to the disordered agglomerates, i.e. *the optical properties can be tuned by changing the degree of ordering and optical characterisations could be used to evaluate the degree of ordering.*

The analysis methods developed in this research, namely fitting the effective structures with variable height to determine the degree of ordering in agglomerates, is applicable for many other systems with competing ordered and disordered structure formation.

Also considering the findings from chapter 2, it could be demonstrated that the agglomeration process of isotropic nanoparticles under varying solvent conditions can be studied in steady state using the flow-based approach constituting this research. In chapter 4 the research topic is extended to structure formation techniques for anisotropic nanowires.

4. Agglomeration and Alignment of Unpolar Gold Nanowires

4.1. Introduction

Nanostructures with controlled anisotropy are a promising material for nanotechnology. When anisotropic colloids are used as building blocks, they can be aligned during processing to achieve an anisotropic material. Nano-textured surfaces provide controllable wetting [143], tunable optical properties [144, 145], and can serve different purposes in novel electronic devices, e.g. conductors in future self-assembled molecular scale circuits [146] or as transparent conductive films [147, 148].

Colloidal Gold Nanowires (AuNWs) are particularly useful for transparent conductive coatings due to their good specific conductivity and their thinness [149]. The coating can be applied in a cost- and material-efficient wet coating process directly from solution [150–152] and could become a cheaper and more flexible than the traditional indium, tin oxide process [153]. Aligned AuNW films would allow lower concentrations and therefore better transparency while retaining identical conductivity in one direction compared to an isotropic layer.

When a constant flow field is used for feeding a wet coating system, it could, additionally to the transport, be used to align anisotropic coating particles and produce an aligned film on the surface. Anisotropic particles align in a shear field, a result from seminal studies on complex fluids [154]. When a pressure-driven Poiseuille flow enters a constriction, velocity and shear increase, which increases the alignment of the long axis in flow direction [54].

One topic of this chapter is to find the process parameters and the related microscopic mechanisms that allow alignment of anisotropic AuNWs in a flow field. A laminar flow in a simple cylindrical tube is shown to induce a shear field, sufficient to induce significant alignment in highly anisotropic AuNWs.

While spherical particles are known to readily assemble to ordered superlattices (see section 1.2), building superstructures from anisotropic particles requires more acumen [155]. Ordered [156] and aligned [157] superstructures of shorter semiconductor nanorods have been demonstrated. In this chapter, methods to create and align ordered superstructures of longer AuNWs stabilised with oleylamine (OAm) are discussed. Their structure and alignment is assessed by analysing two dimensional SAXS patterns.

One finding in this chapter concerns the stabilisation of the AuNWs. By changing the concentration of the stabilising surfactant, the double role of the molecules in the self-assembly of the ordered superstructures is proved. It serves to passivate the surface and as a dissolved molecule mediating a depletion interaction.

The depletion interaction (section 1.2) has been shown to induce 2D crystallisation in simulations of anisotropic particles when adding nonadsorbing polymer [158]. Recent publications suggest that it tips the scales for the self-assembly of isotropic [159] and anisotropic colloids [156] when depletants are present. The interacting surfactant molecules employed in this study are shown to have a similar effect.

Overall a process to create a hierarchically assembled and aligned material is explored both on the level of the relevant macroscopic and microscopic parameters. How the process can be integrated in a coating process remains to be examined in further studies.

4.2. Methods

The (super)structure of gold nanowires and their behaviour in a flow field were studied using SAXS. The data analysis methods as well as the wire synthesis are briefly introduced in this section.

4.2.1. SAXS

The SAXS data presented in this chapter was acquired with a laboratory scale SAXS-machine, the XEUSS 2.0 from XENOCS, using a PILATUS3 R 1M X-ray area detector[1], the principle setup is sketched in fig. 1.8. The single image acquisition time was 60 s. 6–50 images were summed up and divided by the total acquisition time for every measurement. To facilitate correct background subtraction, the same flow-through capillary was used for background and sample measurements and the transmission was corrected using transmitted intensity data from a PIN-diode in the beam stop. The sample to detector distance was determined by calibration with silver behenate after every change of the setup.

The flow rates were controlled with a gas tight glass syringe in a cetoni "NEMESYS" syringe pump. FEP tubing with 762 µm inner diameter was used to connect the syringe to the glass capillary with 0.9 mm inner diameter.

For aggregates of (approximately) identical subunits, a peak in $I(q)$ corresponds to a recurrent distance between single scattering units [124, p. 72]. In the case of regular packings, the distance corresponds to the distance between planes of

---

[1] The detector has pixels with 172 µm × 172 µm and was placed at distances from 0.4 m to 1.2 m to the sample position.

the (super)lattice. The centre-to-centre distances d_{ctc} in fig. 4.3 and fig. 4.4 were derived from the first peak ($h = 1$, $k = 0$) according to the equation for the maxima in scattering patterns of two dimensional hexagonal lattices [119]:

$$q_{\max}\left(h, k\right) = \frac{4\pi}{\sqrt{3}d_{\mathrm{ctc}}}\sqrt{h^2 + k^2}, \tag{4.1}$$

here h and k are the Miller indices of the peaks.

A typical 2D pattern of as-synthesised nanowires is drawn in fig. 4.1 (a). For display purposes, masked detector areas, e.g. in fig. 4.5, were filled with the centrosymmetrically reprojected intensity value when available, minimising the dead area to three smaller fields (fig. 4.1 (b)).

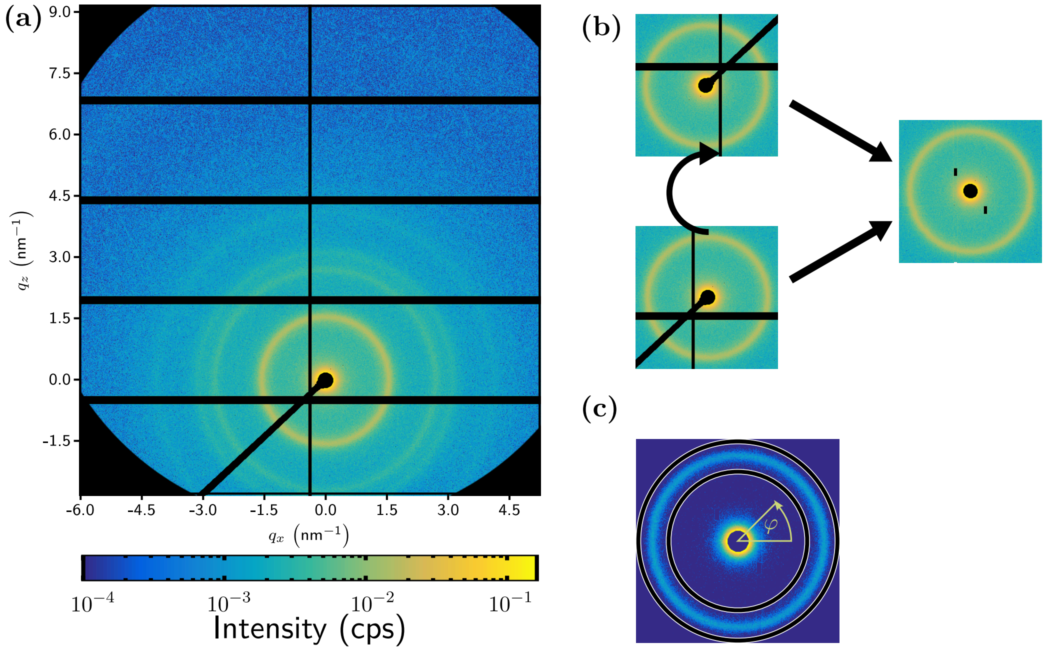

Figure 4.1.: (a) SAXS Detector image of as-synthesised AuNWs. The rings indicate bundling. (b) For display purposes, masked detector areas were filled with the centrosymmetrically reprojected value when available. (c) To characterise anisotropy, the dependency of the integrated intensity of the first peak (i.e. in the area enveloped by the lines in the pattern) on the azimuthal angle φ is analysed. The nematic order parameter is calculated according to eqs. (4.2) and (4.5).

To quantify the anisotropy of the 2D SAXS patterns, the intensity of the first peak was integrated according to the scheme in fig. 4.1 (c): The radial range of the peak was defined as $0.6\,\mathrm{nm}^{-1} \leq q \leq 0.9\,\mathrm{nm}^{-1}$. The dependency of the intensity in this area on the azimuthal angle φ, $I(\varphi)$ was calculated and the symmetry of the patterns was used to transform the angular range of $\varphi \in [0°, 360°]$ to the range of $\vartheta \in [0°, 90°]$. In this form it is related to the orientational distribution $f(\vartheta)$ of anisotropic scatterers. If there is a preferential orientation, the average direction of the long axis of the scatterers is often referred to as director. $f(\vartheta)$ describes the distribution of the angles between the long axis of the scatterers and the director. Since the intensity pattern $I(\varphi)$ represents a projection of the 3D orientational distribution, the possible orientations out of the plane parallel to the detector area have to be accounted for and the scattered intensity is proportional to the integral

$$I(\varphi) \sim \int f(\vartheta)\mathrm{d}\omega, \tag{4.2}$$

where ω is the angle between the scatterer's long axis and the X-ray beam, and

$$\cos\vartheta = \cos\varphi \sin\omega. \tag{4.3}$$

A numerical routine was realised in Python using the NumPy and lmfit packages to allow fitting of a numerical representation of the integral in eq. (4.2) to the data. A Pseudo-Voigt peak function was chosen to represent a generic orientational distribution, since a parametrisation of the shape was needed to perform a fit.

To obtain a representative number for the anisotropy of the scattering patterns, i.e. the scatterers themselves, the nematic order parameter [160, p. 24]

$$S = \left\langle \frac{3\cos^2\vartheta - 1}{2} \right\rangle \tag{4.4}$$

was calculated. The brackets indicate an ensemble average and ϑ is defined as above. The nematic order parameter is 0 for an isotropic orientational distribution and takes typical values from 0.4 to 0.8 for nematic liquid crystal phases [160, p.]. It can be calculated from the orientational distribution function $f(\vartheta)$ [161] as

$$S = \int_0^{\frac{\pi}{2}} f(\vartheta)\frac{3\cos^2\vartheta - 1}{2}\sin\vartheta\mathrm{d}\vartheta, . \tag{4.5}$$

The orientational distribution is normalised, such that

$$\int_0^{\frac{\pi}{2}} f(\vartheta)\sin\vartheta\mathrm{d}\vartheta = 1. \tag{4.6}$$

4.2.2. Gold Nanowires

The wires were synthesised following a protocol adapted from [162]. In a typical synthesis of 10 mL AuNW dispersion, 34 mg of chloroauric acid were dissolved in a mixture of 1.9 mL OAm and 6.44 mL *n*-hexane to form a yellow solution. 1.66 mL triisopropylsilane were added as a reducing agent and the solution was stirred vigorously for 30 s. The reaction solution was then flushed with argon and left undisturbed at room temperature over night. The wires slowly formed, indicated by a gradual colour change to dark red.

To remove residues from synthesis, aliquots were precipitated by adding the approximately threefold amount of ethanol and centrifugation. After removing the supernatant, the precipitate was redispersed in *n*-hexane and precipitated again following the same protocol. The resulting precipitate of the aliquots was redispersed in different solvents, while keeping the initial volume fractions, to find the most suitable solvent. The solvents used here were hexane and cyclohexane. The wires are dispersed after gentle shaking, as indicated by the disappearance of the precipitate. To exclude kinetic effects on bundling, the solutions were left undisturbed over night before measurement unless stated differently.

4.3. Nanowire Bundling

In this section the influence of different solvent conditions on a stagnant nanowire dispersion is examined.

4.3.1. Results

The experimental results for separated wires are presented separately from the results fur bundled wires.

4.3.1.1. Primary Nanowires

The characterisation results for isolated AuNWs are shown in fig. 4.2. The TEM image illustrates the high aspect ratio and the small diameter ($\lesssim 2\,\mathrm{nm}$) of the AuNWs. The minimum in the SAXS pattern of AuNWs dispersed in cyclohexane was fit with the form factor of a cylinder [84, 163] using the *SASfit* software package [164].

The AuNW radius determined from the fit was $0.85 \pm 0.08\,\mathrm{nm}$, in good agreement with the TEM results. The length of the wires is larger than the TEM image section and beyond the resolution of the SAXS machine. Based on literature reports [165], we estimate the length of the wires to be on the order of 1 µm. The wires can be visualised as long, straight cylinders. Their persistence length [166] at room temperature can be estimated as $L_\mathrm{P} = 15\,\mathrm{\mu m}$, based on their radius and the elastic modulus of bulk gold [91, pp. 624 ff.]. Since the estimated wire length is much

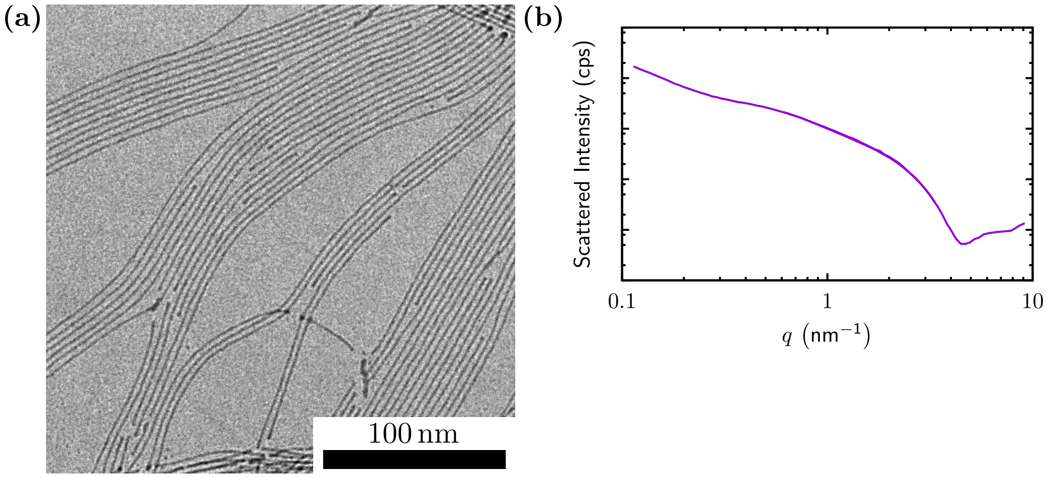

Figure 4.2.: (a) TEM image of AuNWs. (b) SAXS pattern of well-dispersed, isolated AuNWs in cyclohexane.

smaller, it is safe to assume that the wires are not bent or coiled while in dispersion, because thermal energy is not sufficient to overcome the bending rigidity[2].

---

[2] The bent appearance in the TEM image in fig. 4.2 is likely an artefact of the drying process prior to imaging.

4.3.1.2. Bundled Nanowires

To clean colloidal dispersions from synthesis residues, it is common practice to precipitate the product, remove the supernatant and redisperse the precipitate in pure solvent (“washing”). Results on the effect of the washing are presented in the following.

In fig. 4.3 (a) the scattering patterns of as-synthesised AuNWs and the dispersion in hexane after washing are plotted (the curves have a constant offset for better visibility). Both patterns matched the pattern of a two dimensional hexagonal lattice, the indices of the peaks are shown for the as-synthesised wires. Their occurrence proves the formation of AuNW superstructures with hexagonal symmetry (in the plane perpendicular to the long axis) as it has been reported before for as-synthesised AuNWs prepared by an almost identical route [165]. The bundles can be imagined as bundles of wires, structurally similar the strands of a steel rope. As an alternate model, they are structurally very similar to an ordered smectic phase of a liquid crystal. The magnitude and shape of the background suggest that a fraction of unbundled wires was still dispersed. The position of the peaks

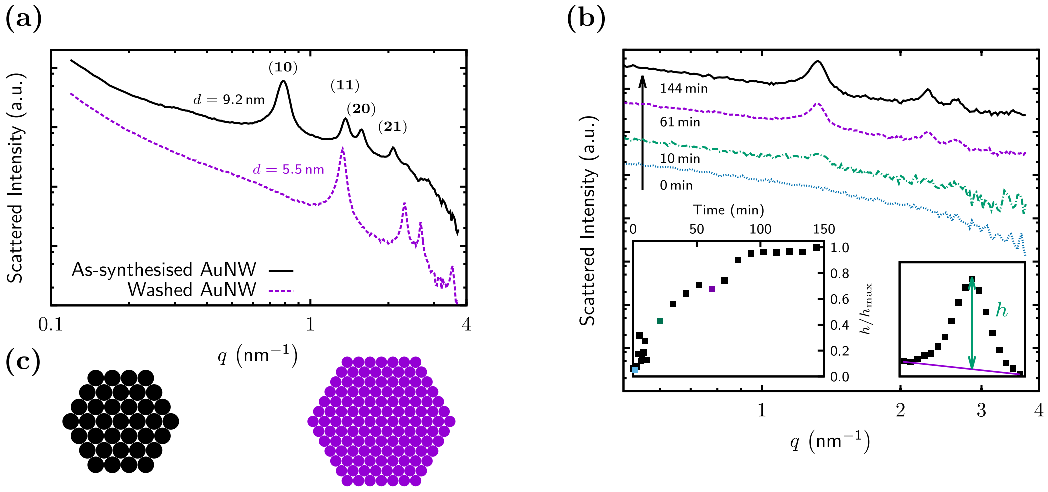

Figure 4.3.: (a) Scattering patterns of AuNWs as-synthesised (solid black) and after washing and leaving undisturbed for 1 d (dashed purple), offset by factor 10. (b) Evolution of the structure peak for washed AuNWs. Scattering curves are offset by a factor $10^{0.9}$. The inset shows the relative height of the first peak for different waiting times. (c) Sketch of the bundle structure, similar to strands of steel rope. The as-synthesised wires (left) were further separated than the washed wires (right).

was different, which reflects a different wire-to-wire distance in the bundles of the as-synthesised and washed wires, as it is indicated in the graph.

The domain size determined from the peak width by the Scherrer equation (eq. (3.4)) gives a lower boundary for the average bundle thickness. If the bundles consist of a single domain, the bundle thickness and domain size are identical. The average domain size of the as-synthesised AuNW bundles was $L_\mathrm{u} = 63 \pm 8\,\mathrm{nm}$. For the wires after washing the bundles were slightly larger $L_\mathrm{w} = 77 \pm 4\,\mathrm{nm}$. The values were averaged over the first three peaks. Assuming perfect hexagonal symmetry, the structure of a domain can be sketched as in fig. 4.3 (c). Note that the metal core of the AuNW had the same diameter in both cases, the different diameters in the sketch represent the different centre-to-centre distances.

Immediately after redispersing the precipitated wires, the structure correlation peak was absent (bottom curve, $t = 0\,\mathrm{min}$ in fig. 4.3 (b)). It slowly emerged over the course of several hours, as it is noticeable in the other scattering patterns in the graph (the curves are plotted with a constant offset to the previous for better visibility). This can be traced by plotting the height of the peak above the background (h in the enhanced area on the bottom right of fig. 4.3 (b)) versus time, as in the inset on the bottom left. The growth of the peak was fast in the beginning and reached a plateau after approximately 100 min.

Excess oleylamine present in the as-synthesised dispersion is supposed to be removed during the washing. To study the effect of removing the OAm, its volume fraction ϕ_OAm in the as-synthesised dispersion was varied by either adding pure hexane or pure OAm in different amounts. The SAXS patterns in fig. 4.4 (a) indicate a clear dependency of the distance between the AuNWs inside the bundle d_ctc on the OAm volume fraction ϕ_OAm, highlighted in fig. 4.4 (b). *The more free OAm was present in the solution, the closer together the single wires were in a bundle.* Although the plotted graphs were corrected for the reduction of gold concentration by adding more solvent to the solution, the peak height for the reduced OAm volume fractions is considerably smaller than for the as-synthesised concentration, indicating a lower fraction of bundles

The oleylamine was not the only factor contributing to wire formation. From fig. 4.3 it is already clear that the AuNWs bundles in the washed dispersion, where the free OAm concentration should be close to zero, were packed closer together than the wires in the bundles in the as-synthesised state, where free OAm has a volume fraction of 0.2. This OAm concentration was added again to the washed dispersion and the bundling peak disappeared after less than 5 min and no peak emerged until the following day.

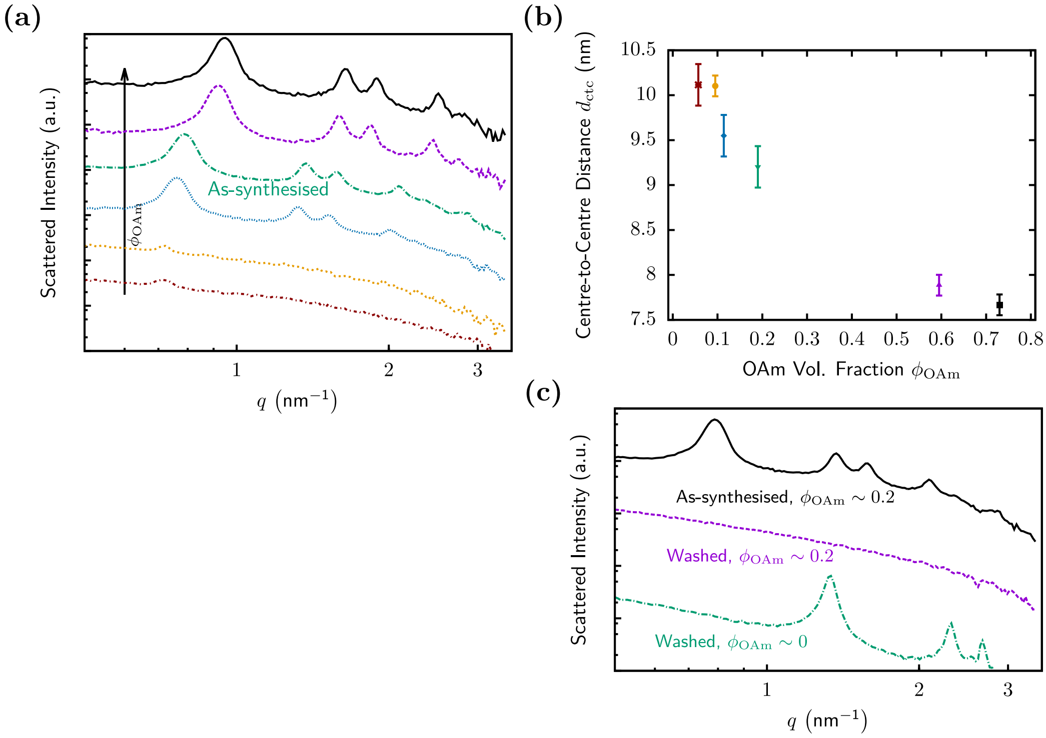

Figure 4.4.: (a) SAXS patterns (offset by a factor of 10) of AuNW bundles as-synthesised and with adjusted OAm volume fractions and (b) the resulting centre-to-centre distances. (c) Comparison of washed AuNW dispersions, with added OAm and the as-synthesised dispersion (offset by a factor of $10^{1.4}$).

4.3.2. Discussion

The in situ SAXS patterns presented here allow insights on the dispersion state of the AuNWs not achievable with straightforward TEM studies, because the drying process masks the true solvated structure. The solvent quality played a role in the bundle formation process. The SAXS patterns of wires dispersed in cyclohexane (fig. 4.2) clearly did not show bundling peaks, as opposed to the patterns in hexane (fig. 4.3). *From a colloidal stability point of view, cyclohexane is a better solvent than its linear counterpart*[3]. The relatively high background around the peaks for

---

[3] The same behaviour was observed for octane and its cyclic counterpart. While there were no structure peaks for the AuNWs dispersed in cyclooctane (separate wires), there was a hexagonal pattern with identical peak positions to the ones presented here for AuNWs dispersed in *n*-octane.

all cases suggests, that only a fraction of the AuNWs was bound to bundles, there was a significant amount of distinct wires in dispersion.

The van der Waals interaction between the gold cores strives to associate the surfaces of distinct nanowires. Entropic forces can be both attractive and repulsive. Oleylamine adsorbed on the AuNW surface provides steric stabilisation of the dispersed AuNWs by counteracting the attraction with an repulsive entropic force and hindering direct, irreversible contact of the gold surfaces [22, p. 387], see also section 1.2.

While the steric stabilisation was sufficient to prevent precipitation, the attraction was strong enough to induce bundling for the wires dispersed in linear alkanes. The reduced OAm content of the washed AuNW dispersion explains the difference in interwire separation for the as-synthesised and the washed dispersion (fig. 4.3). The centre-to-centre distance of the wires in the as-synthesised dispersion was $d_{\mathrm{ctc}} = 9.2\,\mathrm{nm}$; the radius of the wires was determined as $0.85\,\mathrm{nm}$. This results in an interwire gap of approximately $7.5\,\mathrm{nm}$. With the length of a single OAm molecule, $\sim 2.1\,\mathrm{nm}$ [167], it can be estimated that 4 OAm molecules filled the gap between the gold cores of the AuNWs. This corresponds to an OAm double layer surrounding every wire. Double layer protected wires were also found in literature [165], which makes it a likely candidate for the true sample structure. The ligand monolayer is likely in a crystallised state (similar to the situation of an alkylthiol layer at low temperatures described in section 1.2.3.3), because the formation of a second ligand layer in a liquid monolayer appears counterintuitive.

The gap between the washed wires in hexane measured $\sim 3.8\,\mathrm{nm}$, corresponding to a monolayer of OAm surrounding the wires[4]. *The as-synthesised wires were stabilised by a bilayer of OAm. Washing the dispersion removed the second layer leaving only a monolayer.*

The parallel orientation of the wires, necessary to form a bundle, was a direct consequence of the highly anisotropic shape. For two interacting wires, a net torque towards the parallel orientation exists for all configurations except parallel or perpendicular orientation. The perpendicular configuration is an unstable equilibrium; the system is driven to the stable parallel orientation.

On the time scale of the measurements (several hours), the dispersions were stable. No considerable sedimentation was observed. The growth of the bundles is substantially slowed after a certain time (see the inset of fig. 4.3 (b)) and a large fraction of free wires remained. The steric stabilisation by the OAm was sufficient to prevent unlimited bundle growth. The wires attached in a bundle are likely

---

[4] Additional measurements were performed for AuNWs resuspended in other linear alkanes and yielded similar distances. Aromatic carbohydrates changed the interwire distance, while cyclic alkanes impeded bundle formation. These results emphasise the impact of solvent ligand interactions and will be published elsewhere.

trapped in a secondary minimum of the energy landscape (see section 1.2.2.4). The bundles themselves are small enough to remain dispersed, therefore the dispersion remains stable.

The OAm volume fraction dependence of the interwire distance reveals the different mechanisms responsible for bundle formation. The as-synthesised wires were surrounded by a tightly bound double layer of OAm. The amine groups of the second layer were more likely directed in the solution than to the inside of the layer for surface energetic reasons. The wires can be envisioned as a composite material with a small gold core surrounded by a permanently adsorbed OAm bilayer, with amine groups on the surface of the composite.

The interaction potential contributions that can be influenced by the free OAm volume fraction are discussed in the following. The solvent quality for an adsorbed surface layer changes the average height of the layer, similar to polymers dissolved in solvents of different quality [22, p. 382]. When the outermost group is the amine group, the effect should act in the other way around though (see also section 1.2.2.3) and can be ruled out as an explanation here. The more free OAm is in solution, the more expanded the bilayer should be, contrary to the observed trend.

A conceivable alternative explanation would be a change in the van der Waals interaction due to the changed effective Hamaker coefficient, caused by the different chemical composition of the medium between the wires. The relatively small chemical difference of hexane and OAm makes a large variation appear unlikely. Values for the Hamaker coefficient of OAm were not available to the author, it can be estimated from the refractive indices based on the Lifshitz theory [22, p. 261]. The estimated Hamaker constant for OAm interacting through a hexane medium is then $A_{\mathrm{OHO}} \sim 4 \times 10^{-21}$ J. While the effect can not be ruled out, the expected small change in surface coverage appears as an unlikely explanation for the drastic changes in distance observed here.

The huge excess of free OAm ($\phi \sim 20\,\%$, $\sim 10^6$ OAm molecules per gold nanowire (AuNW)) from the synthesis could induce a depletion interaction force between these composite wires. For higher depletant volume fractions, the attraction due to the depletion interaction is increased likewise due to the increased osmotic pressure. An increased depletion interaction due to higher OAm concentrations would push the composite wires in a bundle closer together, in accordance with the observed inverse correlation between distance and concentration. The depletion interaction is often discussed qualitatively as an important force for self-assembly [156]. The magnitude of the interaction energy U_{depl} per unit length L between parallel cylinders with radius R can be estimated as

$$\frac{U_{\mathrm{depl}}(d)}{L} = -\frac{4}{3}\sqrt{R}\,(\sigma - d)^{\frac{3}{2}}\,\Pi, \tag{4.7}$$

where d is the distance between the cylinder surfaces, σ is the diameter of the depletant and Π is the osmotic pressure (using the number density of depletants ρ, $\Pi \sim \rho k_\mathrm{B} T$ for dilute solutions) [168]. The interaction energy at $\phi = 0.2$ (where the compression is already pronounced) can be estimated by assuming a rigid nanowire with a diameter identical to the next neighbour distance in the bundle and a linear relation for the osmotic pressure. With an estimated radius of gyration of $\sigma/2 = 0.9\,\mathrm{nm}$, the interaction energy per unit length of wire of the depletion interaction at $20\,°\mathrm{C}$ is $\frac{U_\mathrm{depl}(d)}{L} \sim 0.4 k_\mathrm{B} T \cdot 1\,\mathrm{nm}^{-1}$. With a wire length above $1\,\mu\mathrm{m}$, this results in a considerable contribution to the interaction potential. *The depletion interaction explains the OAm concentration-dependant interwire distance in the as-synthesised dispersion.* The reduced peak height for the lowest OAm concentrations results from a smaller fraction of bundled AuNWs, due to the reduced attraction.

The free OAm concentration in the washed dispersion was negligible compared to the as-synthesised solution. Correspondingly the depletion interaction did not play a role and the van der Waals attraction between the wires remains a likely candidate for the attractive force generating the bundles. The smaller interwire distance suggests that the second OAm layer around the wires is removed during washing. The AuNWs can approach closer before the steric repulsion occurs and the so-called secondary minimum, where the attractive and repulsive potentials form a minimum, can be reached (see section 1.2.2.4). In this situation the AuNWs were attached reversibly.

When additional free OAm was added to the washed solution, it was able to break the attachment of wires, evident from the absence of the bundle peak in fig. 4.4 (b), possibly by reforming a second OAm layer. The as-synthesised AuNWs displayed bundling at the same OAm concentration. This suggests that the other solutes present in the as-synthesised dispersion and removed during washing, e.g. the triisopropylsilane, enhanced the depletion interaction of the AuNWs. The hypothesis of different driving forces in the as-synthesised and washed case is further corroborated by the temporal evolution after washing (fig. 4.3 (b)). Directly after washing the wires were separated, it takes time for the bundles to form again.

Earlier speculations in literature that the dispersion interaction is the dominating attractive force for the as-synthesised wires [165] are challenged by these results. If the van der Waals attraction would be strong enough to stabilise bundles of AuNWs surrounded by an OAm bilayer, monolayer protected AuNWs should not disassemble upon addition of OAm. The understanding of the bundling process is crucial to the preparation of materials, equally whether bundles or separated wires are desired.

4.4. Flow Influence

The nanowire bundles observed in the previous section represent one level of a nanoscale superstructure constituted by AuNWs. Aligning anisotropic nanowires to a second level of superstructure is favourable for many applications. In this section, the adoption of the shear, originating from the pressure-induced flow field inside the flow-through capillary, to create aligned nanowire superstructures is explored.

4.4.1. Results

The 2D scattering patterns of as-synthesised AuNWs were recorded in the flow-through capillary for different flow velocities (fig. 4.5). The images were cropped here to display only the first ring (induced by the bundling). Compared with the stationary sample, the patterns displayed increasing anisotropy for increasing flow velocities. For anisotropic scatterers, the anisotropy in the scattering pattern is correlated to the anisotropy in the orientation distribution of the scatterers [161]. The scattered intensity around the horizontal axis (polar angle $\varphi = 0°$ and $\varphi = 180°$) increased, while the intensity at the perpendicular direction ($\varphi = 90°$ and $\varphi = 270°$) decreased with increasing flow velocity, corresponding to increased shear rates.

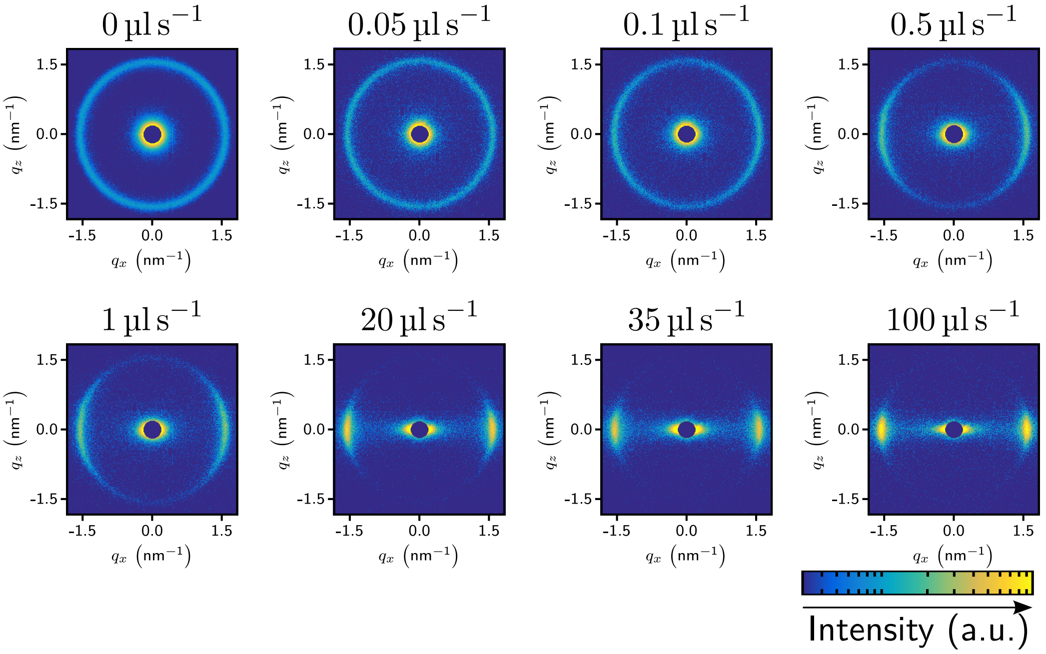

Figure 4.5.: 2D SAXS patterns of as-synthesised AuNWs at different flow velocities.

To compare the amount of anisotropy at the different velocities, the nematic order parameter according to eq. (4.5) was calculated (fig. 4.6). The coloured triangles were calculated for measurements conducted one day after the others. While the absolute value of the S values was offset for the second set of measurements, the trend stayed the same: The nematic order parameter clearly increased with increasing flow velocity (fig. 4.6), which correlates to the visual impression of fig. 4.5. *For increasing flow velocity, the orientation of the sample increased.*

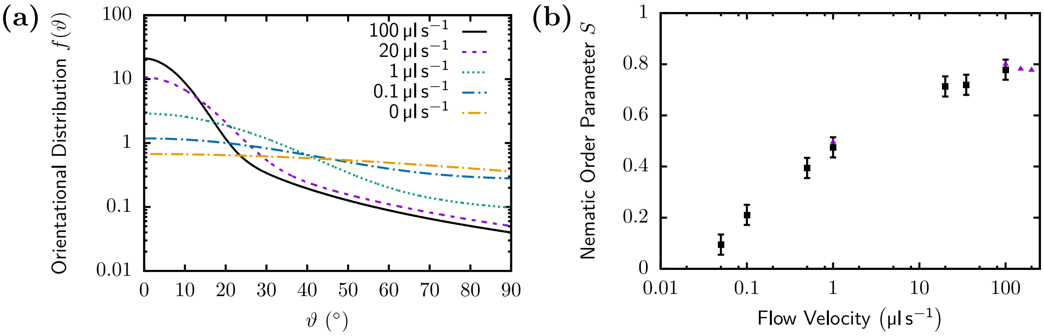

Figure 4.6.: (a) The orientational distribution fitted to the azimuthal distribution of scattered intensity according to eq. (4.2) for different flow velocities. (b) The resulting nematic order parameter as a function of flow velocity.

Kinetics

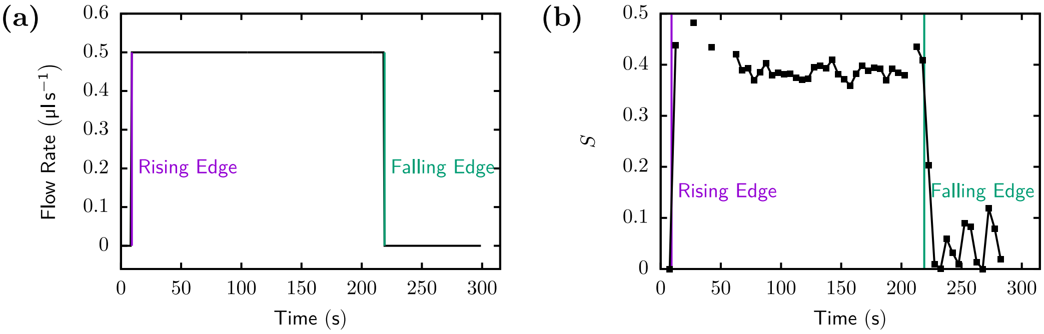

Figure 4.7.: (a) The flow profile imposed on the system by the syringe pump. (b) The alignment response of the wires to the imposed flow profile. The fast dynamics prove that the alignment is induced directly in the capillary.

The temporal evolution of the anisotropy was investigated to illuminate the mechanism responsible for its formation. Image series with 5 s integration time were acquired, while the syringe pump created a flow rate step profile with $0.5\,\mu\mathrm{L\,s^{-1}}$ (fig. 4.7 (a)). During the rising and falling edge, special care on synchronisation was taken. The edges were triggered after 4 s of the current image acquisition. This way, a change in the signal of this image indicates changes in the sample during the first second, and the subsequent image contains information on the sample behaviour in the following 5 s.

The evolution of the nematic order parameter (eq. (4.5)) during the experiment is plotted in fig. 4.7 (b). The vertical lines mark the rising and falling edge of the flow rate profile. It is clear from the data that even during the first second of the onset/switch-off of the flow the anisotropy of the pattern increased/decreased. After less than 30 s, a steady state was reached.

4.4.2. Discussion

The results in fig. 4.5 and fig. 4.6 clearly show that the sample structure became increasingly anisotropic with increasing flow velocity. It should be noted that the aligned entity was here bundles of AuNWs, as indicated by the pronounced hexagonal peak.

The bundles were well-oriented. The nematic order parameter continuously increased with, attaining values characteristic of nematic liquid crystal phases at higher velocities [169]. *Even with the moderate flow rates applied here, it was possible to achieve good orientation of the AuNW bundles.*

The driving force for the orientation of the AuNW bundles was the flow-induced shear inside the system, evidenced by the flow rate dependency[5]. Often anisotropic particles are aligned when the inner diameter is reduced along the flow direction[6]. The strongest reduction of diameter (by 97 %) was present at the syringe. The alignment of anisotropic macromolecules or colloids at constrictions is a current topic of research [54, 171] and a possible candidate for the origin of the behaviour observed here.

Another ubiquitous shear field stemmed from the flow velocity gradient along the radial profile of the parabolic velocity field (see eq. (1.27)). The shear rate $\dot{\gamma}$ has its maximum at the boundary with the inner wall of the system due to the steep decay of the velocity profile and linearly decays to $\dot{\gamma} = 0$ at the centre $r = 0$.

The upper boundary for the time until the observed sample is fully orientated for a mean flow velocity of $0.5\,\mu\mathrm{L\,s^{-1}}$ can be estimated as $\tau \lesssim 30\,\mathrm{s}$ from fig. 4.7

---

[5] The shear rate is discussed at the end of this discussion section.

[6] If the constriction is tighter than the long axis, alignment happens due to the geometric confinement [170].

(the relaxation time at the end of the profile was on the same order). The time it took to convect a AuNW at the centre of the flow field (where the fastest stream line is found) from the syringe to the detector can be estimated as $\tau' \gtrsim 480\,\mathrm{s}$ from measurements during replacement of pure solvent by AuNW dispersion. This clearly excludes the constriction at the syringe exit as a source for the AuNW bundle orientation.

While the steady-state took $\sim 30\,\mathrm{s}$ to develop (and also to relax), the onset time for the process was on the order of $1\,\mathrm{s}$. This restricts the possible location for the source of orientation to $1\,\mathrm{mm}$ upstream of the detection position. Considering these boundaries and the clear correlation with flow velocity, *the shear induced by the parabolic flow field remains the most likely origin for the orientation of AuNWs in the flow system.*

The orientation of the AuNWs likely follows the shear profile and the degree of orientation is expected to decay from the walls toward the centre. The spatial distribution of orientation could not be resolved in this research due to the restricted minimum beam size available. The kinetics of the orientation was faster than the time resolution. Both, the spatial and temporal resolution issues, could be overcome by repeating similar experiments at a microbeam synchrotron source.

The dynamics of anisotropic particles subject to Brownian motion and an external flow field are poorly understood [172]. To get an estimation of the balance between diffusive and convective behaviour, it is useful to define a rotational Péclet number

$$\mathrm{Pe_r} = \frac{\dot{\gamma}}{D_\mathrm{r}}, \tag{4.8}$$

where $\dot{\gamma}$ is the shear rate and

$$D_\mathrm{r} = \frac{3k_\mathrm{B}T\ln\left(\frac{L}{D}\right)}{\pi\eta L^3} \tag{4.9}$$

the rotational diffusion coefficient [173]. L denotes the length of the anisotropic particle and D the diameter. η is the dynamic viscosity of the solvent.

$D_\mathrm{r} \sim 36\,\mathrm{s^{-1}}$ is an approximate value for the rotational diffusion coefficient. The input parameters were estimated as $T = 298.15\,\mathrm{K}$ (room temperature), $D = 63\,\mathrm{nm}$ (average domain size of bundles), $L = 1\,\mathrm{\mu m}$ (expected length of a single wire[7]) and $\eta = 0.3\,\mathrm{mPa\,s}$ (viscosity of hexane as a lower boundary [174]). The shear rate depends on the radial distance from the centre of the capillary. For the sake of this estimation, the area average of the shear (see eq. (1.28)) is calculated. The area average shear assumes values from $\bar{\dot{\gamma}} = 0.77\,\mathrm{s^{-1}}$ for $0.05\,\mathrm{\mu L\,s^{-1}}$ to $\bar{\dot{\gamma}} = 1531\,\mathrm{s^{-1}}$ for $100\,\mathrm{\mu L\,s^{-1}}$.

---

[7] The bundles could be longer than the single wires. Greater lengths would lead to even larger $\mathrm{Pe_r}$ and support the following argument.

Consequently, the rotational Péclet number assumes values from $\mathrm{Pe_r} = 0.02$ for $0.05\,\mu\mathrm{L\,s^{-1}}$ $\mathrm{Pe_r} = 42$ for $100\,\mu\mathrm{L\,s^{-1}}$. For flow velocities larger than $2.5\,\mu\mathrm{L\,s^{-1}}$ the Péclet number is larger than 1 and the flow field dominates rotational diffusion. This explains the relatively small changes in orientation at higher flow rates. *Although some approximations had to be made, the large values clearly corroborate that the shear field indeed dominates the orientational dynamics of the wires.*

4.5. Conclusions

The dual role of oleylamine for the stability of ultrathin gold nanowires was demonstrated in this chapter. The tunable process parameter for this case is the *oleylamine concentration* in the continuous phase. By tuning the concentration, the formation and structure of nanowire bundles can be controlled due to the *microscopic depletion interaction effect.* This is a significant result that reveals how rules of thumb about the function of different components in a colloidal sample should be taken with a pinch of salt. A “stabiliser” molecule (like oleylamine) can actually act as a destabiliser under different conditions in the same sample.

The self-assembly of AuNWs into bundles could be a method to create novel nanomaterials. Similar to a steel rope, the bundles could be a mechanically more stable alternative to separated wires in the application as a transparent conductive material.

To reduce the amount of material required for sufficient conductivity in one direction, it is favourable to align the long axis in the conduction direction. Here it is demonstrated that the rather simple shear field in the laminar, pressure driven pipe flow (*accessible in the flow setup established in this research*) is sufficient to align the nanowires. By tuning the process parameter *flow rate*, the degree of alignment could be controlled due the *shear induced torque that easily dominates the rotational diffusion.* Further research could show methods to transfer the alignment to a surface film.

To exploit the flow orientation of the wires in a surface deposition setup, the evaporation should be faster than the reorientation to transfer the structure to the surface. Simply increasing the vapour pressure by substrate heating is problematic. Due to the Rayleigh instability, AuNWs are known to decompose to spheres at temperatures well below the melting temperature [175]. Further research will be necessary to exploit the effect observed here.

5. Conclusion

5.1. Conclusion

To draw conclusions on the research presented, it is useful to separately consider the main objectives defined in the introduction.

A modular, flow-based system to prepare and detect steady states of agglomeration of nanoparticles was established for the first time in this research. The setup succeeded in providing temperature control as well as fast control over concentrations and the age of the observed steady states. The integration times unlocked by the methodology are not achievable with other *in situ* methods in a single experiment. The components are flexibly interchangeable. This allowed the adaptation of the system to the different requirements at various synchrotron beamlines and the laboratory scale SAXS machine at the INM. Several analysis programs were developed, only partially specific to the research topics of the respective chapters.

While the wall-induced velocity gradient served the purpose of aligning anisotropic colloids in chapter 4, it also imposes a distribution of residence times on the detected sample. This further impedes the deconvolution of the effect caused by inherent distributions like particle size and the agglomerate size distribution already present exclusively due to statistical growth.

Process parameters determining the agglomeration process were identified for all three classes of colloids. It was shown that the agglomerates produced by adding hydrochloric acid to an *aqueous dispersion of spherical gold nanoparticles* did not exhibit long-range supercrystalline order. While their internal structure could not be further resolved, it was demonstrated that the acid concentration controls the growth rate of the agglomerates even at concentrations above the threshold for purely diffusion limited agglomeration expected from DLVO theory. The surface modification of the particles was found to influence the predisposition of the particles to agglomerate.

The structure of agglomerates produced by adding polar solvent to *sterically stabilised, spherical gold nanoparticles in heptane* was found to contain signatures of both ordered and disordered superstructures. The balance between the two elements could be changed in favour of ordered superlattices by increasing temperature (as it was shown before) or decreasing the solvent polarity (previously not observed). Longer ligands impeded superlattice formation at otherwise equal conditions. Ordered fcc nuclei that form not later than 5 s after initiation of the process were observed for the first time. The strong influence of agglomerate structure on the absorbance spectra for otherwise identical conditions that was revealed here could be exploited for future designs of novel plasmonic materials.

Sterically stabilised, ultrathin gold nanowires were characterised during all processing stages; in the as-synthesised dispersion, after washing and during advective transport. Their bundle formation was governed by the excess concentration of the stabilising molecule, an effect that has not been observed before. The bundles were readily aligned along the flow direction in a plain pressure-driven flow.

The important microscopic mechanism strongly differed depending on the colloid. The basic interactions for all three different colloids examined in this dissertation are the same. However, depending on the details of the present colloidal system, their relative importance for structure formation changed.

The interaction of the *aqueous dispersion of spherical gold nanoparticles* was governed by the balance between electrostatic repulsion and van der Waals attraction. Only for completely sterically stabilised particles (MUTEG) the electrostatic repulsion was insignificant; for partial sterical stabilisation (PEG) the electrostatic repulsion played the major role. The agglomeration of citrate-stabilised particles was accelerated by increasing acid concentrations far above the expected critical coagulation concentration. The microscopic origin of this behaviour could not be explained in this work.

The ligand shell of *sterically stabilised, spherical gold nanoparticles in heptane* turned out to govern the interparticle interaction, by determining repulsion, contributing to attraction and determining the mobility of particles attached to agglomerates. A hidden monolayer phase transition, as it was found in earlier studies, had to be assumed to account for the different behaviour of various ligand lengths.

The following aspects of the interaction during rapid agglomeration are described *for the first time* in this dissertation.

- The influence of solvent polarity on the ligand layer interactions could be qualitatively described by the Flory-Huggins theory. Increasing the solvent polarity increased the short-ranged attraction, leading to a noticeable lattice contraction and reduction in size of ordered domains.
- The agglomeration kinetics are faster than reaction-limited agglomeration, likely due to strong short-ranged attraction. Already after less than 5 s ordered fcc domains had formed.
- The increased van der Waals attraction for larger gold cores with identical ligands shifted the temperature scale of the ligand-mediated processes upward.

The ligands of *sterically stabilised, ultrathin gold nanowires* also dominated the interaction between the colloids for the results presented in this work. In contrast to the spherical particles it was not the details of the adsorbed layer that dominated the agglomeration process. An increased amount of unadsorbed, free excess ligand molecules was found to induce a superlattice contraction, likely due to an increased depletion interaction.

5.2. Outlook

Additional studies could aim to solve some of the remaining questions regarding agglomeration from this research. Open questions remain for example on how to integrate the setup as a feed for a deposition system or the influence of shear on the agglomeration of spherical particles. Other influences not considered so far include light, which has been reported to affect the agglomeration process [176].

In principle, the methods employed in this research can be directly applied to many other destabilised colloidal samples, e.g. silica particles or quantum dots. However, to avoid irreversible fouling of the system, a method to reliable remove all sample residues, also eligible for the materials used in the setup (mainly borosilicate glass and FEP), should be available.

A number of technical improvements would be proposed. For future agglomeration SAXS experiments, it would be beneficial to reduce the minimum q value to directly determine the agglomerate size from the Porod oscillations.

Implementing a coaxial (“sheathing”) solvent flow around the sample flow is a conceivable addition to the system. It would alleviate the particle adsorption on the walls (by separating the sample from the boundary) as well as the hydrodynamic dispersion and the involved spread of agglomerate ages (by flattening the effective velocity profile for the sample). A simple approach was evaluated in the scope of this project, but did not produce reliable results. A more integrated system, with a minimum number of interconnected components, would facilitate the formation of an isolating solvent layer around the sample flow. Using droplets of agglomerating samples surrounded by an immiscible solvent would be an approach more demanding for the measurement techniques, because the measurements would have to be synchronised to the droplet formation rate.

Another shortcoming of the current method is that the sample populations constituting the observed scattering and absorbance signals could not be separated. It is not clear whether the observed scattering and absorbance changes are caused by a few large agglomerates balanced by many single particles or a broad distribution of changes. Additional methods have to be implemented to distinguish these cases.

Bibliography

[1] K. E. Drexler. ‘Molecular engineering: An approach to the development of general capabilities for molecular manipulation’. In: *Proceedings of the National Academy of Sciences* 78.9 (1981), pp. 5275–5278.

[2] C. O. Hendren, X. Mesnard, J. Dröge and M. R. Wiesner. ‘Estimating Production Data for Five Engineered Nanomaterials As a Basis for Exposure Assessment’. In: *Environmental Science and Technology* 45.7 (2011), pp. 2562–2569.

[3] R. Sainidou and F. J. G. de Abajo. ‘Plasmon guided modes in nanoparticle metamaterials’. In: *Optics Express* 16.7 (Mar. 2008), pp. 4499–4506.

[4] M. Draper, I. M. Saez, S. J. Cowling, P. Gai, B. Heinrich, B. Donnio, D. Guillon and J. W. Goodby. ‘Self-Assembly and Shape Morphology of Liquid Crystalline Gold Metamaterials’. In: *Advanced Functional Materials* 21.7 (2011), pp. 1260–1278.

[5] M. V. Kovalenko et al. ‘Prospects of Nanoscience with Nanocrystals’. In: *ACS Nano* 9.2 (2015), pp. 1012–1057.

[6] S. Guldin, S. Hüttner, M. Kolle, M. E. Welland, P. Müller-Buschbaum, R. H. Friend, U. Steiner and N. Tetreault. ‘Dye-Sensitized Solar Cell Based on a Three-Dimensional Photonic Crystal’. In: *Nano Letters* 10.7 (July 2010), pp. 2303–2309.

[7] U. W. Paetzold, M. Meier, E. Moulin, V. Smirnov, B. E. Pieters, U. Rau and R. Carius. ‘Plasmonic back contacts with non-ordered Ag nanostructures for light trapping in thin-film silicon solar cells’. In: *Materials Science and Engineering: B* 178.9 (2013). Advanced materials and characterization techniques for solar cells, pp. 630–634.

[8] S. C. on Emerging & Newly Identified Health Risks. ‘Modified Opinion (after public consultation) On The Appropriateness Of Existing Methodologies To Assess The Potential Risks Associated With Engineered And Adventitious Products Of Nanotechnologies’. In: *Health and Consumer Protection* (2006).

[9] R. F. T. Stepto. ‘DISPERSITY IN POLYMER SCIENCE’. In: *PURE AND APPLIED CHEMISTRY* 81.2 (Feb. 2009), 351–353.

[10] I. Freestone, N. Meeks, M. Sax and C. Higgitt. 'The Lycurgus Cup – A Roman nanotechnology'. English. In: *Gold Bulletin* 40.4 (2007), pp. 270–277.

[11] M. Faraday. 'The Bakerian lecture: experimental relations of gold (and other metals) to light'. In: *Philosophical Transactions of the Royal Society of London* 147 (1857), pp. 145–181.

[12] J. Turkevich, P. Stevenson and J. Hillier. 'A Study of the Nucleation and growth Processes in the Synthesis of Colloidal Gold'. In: *Discussions of the Faraday Society* 11 (1951), p. 55.

[13] B. V. Enustun and J. Turkevich. 'Coagulation of Colloidal Gold'. In: *Journal of the American Chemical Society* 85.21 (1963), pp. 3317–3328.

[14] G. Frens. 'Particle size and sol stability in metal colloids'. English. In: *Kolloid-Zeitschrift und Zeitschrift für Polymere* 250.7 (1972), pp. 736–741.

[15] G. Frens. 'Controlled Nucleation for the Regulation of the Particle Size in Monodisperse Gold Suspensions'. In: *Nature Physical Science* 241 (1973), pp. 20–22.

[16] M. Brust, M. Walker, D. Bethell, D. J. Schiffrin and R. Whyman. 'Synthesis of thiol-derivatised gold nanoparticles in a two-phase Liquid–Liquid system'. In: *Journal of the Chemical Society, Chemical Communications* (7 1994), pp. 801–802.

[17] N. Zheng, J. Fan and G. D. Stucky. 'One-Step One-Phase Synthesis of Monodisperse Noble-Metallic Nanoparticles and Their Colloidal Crystals'. In: *Journal of the American Chemical Society* 128.20 (2006), pp. 6550–6551.

[18] B.-H. Wu, H.-Y. Yang, H.-Q. Huang, G.-X. Chen and N.-F. Zheng. 'Solvent effect on the synthesis of monodisperse amine-capped Au nanoparticles'. In: *Chinese Chemical Letters* 24.6 (2013), pp. 457–462.

[19] B. Derjaguin and L. Landau. 'Theory of the stability of strongly charged lyophobic sols and of the adhesion of strongly charged particles in solutions of electrolytes'. In: *Acta Physicochimica USSR* 14.1–4 (1941), pp. 633–662.

[20] E. J. W. Verwey and J. T. G. Overbeek. *Theory of the stability of lyophobic colloids. the interaction of sol particles having an electric double layer*. New York: Elsevier, 1948.

[21] B. Ninham. 'On progress in forces since the {DLVO} theory'. In: *Advances in Colloid and Interface Science* 83.1–3 (1999), pp. 1–17.

[22] J. N. Israelachvili. *Intermolecular and Surface Forces, Third Edition: Revised Third Edition*. 3rd ed. Academic Press, June 2011.

[23] S. J. Khan, F. Pierce, C. M. Sorensen and A. Chakrabarti. ‘Self-Assembly of Ligated Gold Nanoparticles: Phenomenological Modeling and Computer Simulations’. In: *Langmuir* 25.24 (2009), pp. 13861–13868.

[24] J.-L. M. Abboud and R. Notari. ‘Critical compilation of scales of solvent parameters. Part I. Pure, non-hydrogen bond donor solvents’. In: *Pure and Applied Chemistry* 71.4 (1999).

[25] C. L. Yaws. *Chemical properties handbook*. McGraw-Hill, 1999.

[26] S. Asakura and F. Oosawa. ‘On Interaction between Two Bodies Immersed in a Solution of Macromolecules’. In: *The Journal of Chemical Physics* 22.7 (1954), pp. 1255–1256.

[27] S. Asakura and F. Oosawa. ‘Interaction between particles suspended in solutions of macromolecules’. In: *Journal of Polymer Science* 33.126 (1958), pp. 183–192.

[28] K. J. M. Bishop, C. E. Wilmer, S. Soh and B. A. Grzybowski. ‘Nanoscale Forces and Their Uses in Self-Assembly’. In: *Small* 5.14 (2009), pp. 1600–1630.

[29] H. N. Lekkerkerker and R. Tuinier. ‘Depletion Interaction’. English. In: *Colloids and the Depletion Interaction*. Vol. 833. Lecture Notes in Physics. Springer Netherlands, 2011, pp. 57–108.

[30] N. D. Denkov, O. D. Velev, P. A. Kralchevsky, I. B. Ivanov, H. Yoshimura and K. Nagayama. ‘Two-dimensional crystallization’. In: *Nature* 361.6407 (Jan. 1993), pp. 26–26.

[31] P. C. Ohara, D. V. Leff, J. R. Heath and W. M. Gelbart. ‘Crystallization of Opals from Polydisperse Nanoparticles’. In: *Physical Review Letters* 75 (19 Nov. 1995), pp. 3466–3469.

[32] R. L. Whetten, J. T. Khoury, M. M. Alvarez, S. Murthy, I. Vezmar, Z. L. Wang, P. W. Stephens, C. L. Cleveland, W. D. Luedtke and U. Landman. ‘Nanocrystal gold molecules’. In: *Advanced Materials* 8.5 (1996), pp. 428–433.

[33] R. L. Whetten, M. N. Shafigullin, J. T. Khoury, T. G. Schaaff, I. Vezmar, M. M. Alvarez and A. Wilkinson. ‘Crystal Structures of Molecular Gold Nanocrystal Arrays’. In: *Accounts of Chemical Research* 32.5 (1999), pp. 397–406.

[34] C. B. Murray, C. R. Kagan and M. G. Bawendi. ‘Self-Organization of CdSe Nanocrystallites into Three-Dimensional Quantum Dot Superlattices’. In: *Science* 270.5240 (1995), pp. 1335–1338.

[35] A. M. Kalsin and B. A. Grzybowski. ‘Controlling the Growth of “Ionic” Nanoparticle Supracrystals’. In: *Nano Letters* 7.4 (2007), pp. 1018–1021.

[36] D. A. Weitz and M. Oliveria. ‘Fractal Structures Formed by Kinetic Aggregation of Aqueous Gold Colloids’. In: *Physical Review Letters* 52 (1984), pp. 1433–1436.

[37] M. V. Smoluchowski. ‘Drei Vorträge uber Diffusion, Brownsche Bewegung und Koagulation von Kolloidteilchen’. In: *Zeitschrift für Physik* 17 (1916), pp. 557–585.

[38] M. Elimelech. *Particle deposition and aggregation.* Butterworth-Heinemann, 1998.

[39] M. Y. Lin, H. M. Lindsay, D. A. Weitz, R. C. Ball, R. Klein and P. Meakin. ‘Universality in colloid aggregation’. In: *Nature* 339.6223 (June 1989), pp. 360–362.

[40] W. B. Russel, D. A. Saville and W. R. Schowalter. *Colloidal dispersions.* Cambridge University Press, 1989.

[41] D. A. Weitz, J. S. Huang, M. Y. Lin and J. Sung. ‘Dynamics of Diffusion-Limited Kinetic Aggregation’. In: *Physical Review Letters* 53 (1984), pp. 1657–1660.

[42] M. Y. Lin, H. M. Lindsay, D. A. Weitz, R. C. Ball, R. Klein and P. Meakin. ‘Universal reaction-limited colloid aggregation’. In: *Physical Review A* 41 (4 Feb. 1990), pp. 2005–2020.

[43] E. Shevchenko, D. Talapin, A. Kornowski, F. Wiekhorst, J. Kötzler, M. Haase, A. Rogach and H. Weller. ‘Colloidal Crystals of Monodisperse FePt Nanoparticles Grown by a Three-Layer Technique of Controlled Oversaturation’. In: *Advanced Materials* 14.4 (2002), pp. 287–290.

[44] A. Rogach, D. Talapin, E. Shevchenko, A. Kornowski, M. Haase and H. Weller. ‘Organization of Matter on Different Size Scales: Monodisperse Nanocrystals and Their Superstructures’. In: *Advanced Functional Materials* 12.10 (2002), pp. 653–664.

[45] B. Abécassis, F. Testard and O. Spalla. ‘Gold Nanoparticle Superlattice Crystallization Probed *In Situ*’. In: *Physical Review Letters* 100 (11 Mar. 2008), p. 115504.

[46] N. Goubet, J. Richardi, P.-A. Albouy and M.-P. Pileni. ‘Which Forces Control Supracrystal Nucleation in Organic Media?’ In: *Advanced Functional Materials* 21.14 (June 2011), pp. 2693–2704.

[47] E. V. Shevchenko, D. V. Talapin, N. A. Kotov, S. O'Brien and C. B. Murray. 'Structural diversity in binary nanoparticle superlattices'. In: *Nature* 439.7072 (2006), pp. 55–59.

[48] T. Geyer, P. Born and T. Kraus. 'Switching Between Crystallization and Amorphous Agglomeration of Alkyl Thiol-Coated Gold Nanoparticles'. In: *Physical Review Letters* 109 (12 Sept. 2012), p. 128302.

[49] P. Born and T. Kraus. 'Ligand-dominated temperature dependence of agglomeration kinetics and morphology in alkyl-thiol-coated gold nanoparticles'. In: *Physical Review E* 87 (6 June 2013), p. 062313.

[50] A. Badia, S. Singh, L. Demers, L. Cuccia, G. R. Brown and R. B. Lennox. 'Self-Assembled Monolayers on Gold Nanoparticles'. In: *Chemistry – A European Journal* 2.3 (1996), pp. 359–363.

[51] J. B. Edel, R. Fortt, J. C. deMello and A. J. deMello. 'Microfluidic routes to the controlled production of nanoparticles'. In: *Chemical Communications* (10 2002), pp. 1136–1137.

[52] A. M. Nightingale and J. C. deMello. 'Segmented Flow Reactors for Nanocrystal Synthesis'. In: *Advanced Materials* (2012), n/a–n/a.

[53] A. Schwamberger, B. D. Roo, D. Jacob, L. Dillemans, L. Bruegemann, J. Seo and J. Locquet. 'Combining SAXS and DLS for simultaneous measurements and time-resolved monitoring of nanoparticle synthesis'. In: *Nuclear Instruments and Methods in Physics Research Section B: Beam Interactions with Materials and Atoms* 343 (2015), pp. 116–122.

[54] M. Trebbin, D. Steinhauser, J. Perlich, A. Buffet, S. V. Roth, W. Zimmermann, J. Thiele and S. Förster. 'Anisotropic particles align perpendicular to the flow direction in narrow microchannels'. In: *Proceedings of the National Academy of Sciences* 110.17 (2013), pp. 6706–6711.

[55] S. With, M. Trebbin, C. B. A. Bartz, C. Neuber, M. Dulle, S. Yu, S. V. Roth, H.-W. Schmidt and S. Förster. 'Fast Diffusion-Limited Lyotropic Phase Transitions Studied in Situ Using Continuous Flow Microfluidics/Microfocus-SAXS'. In: *Langmuir* 30.42 (2014), pp. 12494–12502.

[56] G. Mie. 'Beiträge zur Optik trüber Medien, speziell kolloidaler Metallösungen'. In: *Annalen der Physik* 330.3 (1908), pp. 377–445.

[57] U. Kreibig and M. Vollmer. *Optical Properties of Metal Clusters (Springer Series in Materials Science).* 1995th ed. Springer, July 1995.

[58] A. Moores and F. Goettmann. 'The plasmon band in noble metal nanoparticles: an introduction to theory and applications'. In: *New Journal of Chemistry* 30 (8 2006), pp. 1121–1132.

[59] E. B. Guidez and C. M. Aikens. ‘Quantum mechanical origin of the plasmon: from molecular systems to nanoparticles’. In: *Nanoscale* 6 (20 2014), pp. 11512–11527.

[60] C. Kittel. *Introduction to Solid State Physics*. 8th ed. Wiley, Nov. 2004.

[61] K. L. Kelly, E. Coronado, L. L. Zhao and G. C. Schatz. ‘The Optical Properties of Metal Nanoparticles: The Influence of Size, Shape, and Dielectric Environment’. In: *The Journal of Physical Chemistry B* 107.3 (2003), pp. 668–677.

[62] M. Quinten and U. Kreibig. ‘Optical properties of aggregates of small metal particles’. In: *Surface Science* 172.3 (1986), pp. 557–577.

[63] M. M. Alvarez, J. T. Khoury, T. G. Schaaff, M. N. Shafigullin, I. Vezmar and R. L. Whetten. ‘Optical Absorption Spectra of Nanocrystal Gold Molecules’. In: *The Journal of Physical Chemistry B* 101.19 (1997), pp. 3706–3712.

[64] E. Hutter and J. H. Fendler. ‘Exploitation of Localized Surface Plasmon Resonance’. In: *Advanced Materials* 16.19 (2004), pp. 1685–1706.

[65] S. Link and M. A. El-Sayed. ‘Size and Temperature Dependence of the Plasmon Absorption of Colloidal Gold Nanoparticles’. In: *The Journal of Physical Chemistry B* 103.21 (1999), pp. 4212–4217.

[66] U. Kreibig and C. v. Fragstein. ‘The Limitation of Electron Mean Free Path in Small Silver Particles’. In: *Zeitschrift für Physik* 224 (1969), pp. 307–323.

[67] K. Siriwardana, M. Gadogbe, S. M. Ansar, E. S. Vasquez, W. E. Collier, S. Zou, K. B. Walters and D. Zhang. ‘Ligand Adsorption and Exchange on Pegylated Gold Nanoparticles’. In: *The Journal of Physical Chemistry C* 118.20 (2014), pp. 11111–11119.

[68] T. Ung, L. M. Liz-Marzan and P. Mulvaney. ‘Optical properties of thin films of Au@ SiO2 particles’. In: *The Journal of Physical Chemistry B* 105.17 (2001), pp. 3441–3452.

[69] X. Ben and H. S. Park. ‘Size Dependence of the Plasmon Ruler Equation for Two-Dimensional Metal Nanosphere Arrays’. In: *The Journal of Physical Chemistry C* 115.32 (2011), pp. 15915–15926.

[70] A. Beer. ‘Bestimmung der Absorption des rothen Lichts in farbigen Flüssigkeiten’. In: *Annalen der Physik* 162.5 (1852), pp. 78–88.

[71] D. of Chemical Nomenclature, S. R. I. U. of Pure & Applied Chemistry, M. Nic, J. Jirat and B. Kosata. *IUPAC goldbook*. IUPAC, 2006.

[72] O. Glatter. *Small Angle X-Ray Scattering*. Academic Pr, Dec. 1982.

[73] L. Feigin and D. Svergun. *Structure Analysis by Small-Angle X-Ray and Neutron Scattering*. Plenum Press, 1987.

[74] B. R. Pauw. ‘Everything SAXS: small-angle scattering pattern collection and correction’. In: *Journal of Physics: Condensed Matter* 25.38 (2013), p. 383201.

[75] A. Guinier and G. Fournet. *Small-angle scattering of X-rays*. Structure of matter series. Wiley, 1955.

[76] L. D. Landau and L. M. Lifshitz. *Quantum Mechanics, Third Edition: Non-Relativistic Theory (Volume 3)*. 3rd ed. Butterworth-Heinemann, Jan. 1981.

[77] M. Born and E. Wolf. *Principles of Optics: Electromagnetic Theory of Propagation, Interference and Diffraction of Light*. 7th. Cambridge University Press, Oct. 1999.

[78] T. C. Huang, H. Toraya, T. N. Blanton and Y. Wu. ‘X-ray powder diffraction analysis of silver behenate, a possible low-angle diffraction standard’. In: *Journal of Applied Crystallography* 26.2 (1993), pp. 180–184.

[79] G. Ashiotis, A. Deschildre, Z. Nawaz, J. P. Wright, D. Karkoulis, F. E. Picca and J. Kieffer. ‘The fast azimuthal integration Python library: *pyFAI*’. In: *Journal of Applied Crystallography* 48.2 (2015), pp. 510–519.

[80] J. S. Pedersen and C. Riekel. ‘Resolution function and flux at the sample for small-angle X-ray scattering calculated in position–angle–wavelength space’. In: *Journal of Applied Crystallography* 24.5 (Oct. 1991), pp. 893–909.

[81] A. Guinier. ‘X-ray diffraction at small angles’. In: *Annales de Physique* 12 (1939), pp. 161–237.

[82] O. Glatter. ‘A new method for the evaluation of small-angle scattering data’. In: *Journal of Applied Crystallography* 10.5 (Oct. 1977), pp. 415–421.

[83] D. I. Svergun. ‘Determination of the regularization parameter in indirect-transform methods using perceptual criteria’. In: *Journal of Applied Crystallography* 25.4 (Aug. 1992), pp. 495–503.

[84] J. S. Pedersen. ‘Analysis of small-angle scattering data from colloids and polymer solutions: modeling and least-squares fitting’. In: *Advances in Colloid and Interface Science* 70 (1997), pp. 171–210.

[85] L. Rayleigh. ‘The Incidence of Light upon a Transparent Sphere of Dimensions Comparable with the Wave-Length’. In: *Proceedings of the Royal Society of London. Series A* 84.567 (June 1911), pp. 25–46.

[86] G. V. Schulz. ‘The kinetics of chain polymerisation V. The influence of various types of reactions on the poly-molecularity’. In: *Zeitschrift für physikalische Chemie - Abteilung B - Chemie der Elementarprozesse Aufbau der Materie* 43.1 (1939), pp. 25–46.

[87] B. H. Zimm. 'Apparatus and Methods for Measurement and Interpretation of the Angular Variation of Light Scattering; Preliminary Results on Polystyrene Solutions'. In: *The Journal of Chemical Physics* 16.12 (1948), pp. 1099–1116.

[88] M. Kotlarchyk and S. Chen. 'Analysis of small angle neutron scattering spectra from polydisperse interacting colloids'. In: *The Journal of Chemical Physics* 79.5 (1983), pp. 2461–2469.

[89] J. S. Pedersen. 'Determination of size distributions from small-angle scattering data for systems with effective hard-sphere interactions'. In: *Journal of Applied Crystallography* 27 (1994), pp. 595–608.

[90] D. Gazzillo, A. Giacometti, R. G. D. Valle, E. Venuti and F. Carsughi. 'A scaling approximation for structure factors in the integral equation theory of polydisperse nonionic colloidal fluids'. In: *The Journal of Chemical Physics* 111.16 (1999), pp. 7636–7645.

[91] H. Kuchling. *Taschenbuch der Physik*. Fachbuchverlag Leipzig im Carl Hanser Verlag, 2011.

[92] G. K. Batchelor. *An Introduction to Fluid Dynamics (Cambridge Mathematical Library)*. Cambridge University Press, Feb. 2000.

[93] W. M. Deen. *Analysis of transport phenomena*. Oxford University Press, 2012.

[94] A. Paster, T. Aquino and D. Bolster. 'Incomplete mixing and reactions in laminar shear flow'. In: *Physical Review E* 92 (1 July 2015), p. 012922.

[95] J. Li and C. Kleinstreuer. 'Microfluidics analysis of nanoparticle mixing in a microchannel system'. English. In: *Microfluidics and Nanofluidics* 6.5 (2009), pp. 661–668.

[96] N.-T. Nguyen and Z. Wu. 'Micromixers—a review'. In: *Journal of Micromechanics and Microengineering* 15.2 (2005), R1.

[97] D. Dutta, A. Ramachandran and J. Leighton DavidT. 'Effect of channel geometry on solute dispersion in pressure-driven microfluidic systems'. English. In: *Microfluidics and Nanofluidics* 2.4 (2006), pp. 275–290.

[98] G. Taylor. 'Dispersion of Soluble Matter in Solvent Flowing Slowly through a Tube'. In: *Proceedings of the Royal Society of London. Serias A, Mathematical and Physical Sciences* 219.1137 (Aug. 1953), pp. 186–203.

[99] J. Liu and Y. Lu. 'Preparation of aptamer-linked gold nanoparticle purple aggregates for colorimetric sensing of analytes'. In: *Nature Protocols* 1.1 (June 2006), pp. 246–252.

[100] T. Green. ‘Gold etching for microfabrication’. English. In: *Gold Bulletin* 47.3 (2014), pp. 205–216.

[101] J. J. Storhoff, R. Elghanian, R. C. Mucic, C. A. Mirkin and R. L. Letsinger. ‘One-Pot Colorimetric Differentiation of Polynucleotides with Single Base Imperfections Using Gold Nanoparticle Probes’. In: *Journal of the American Chemical Society* 120.9 (1998), pp. 1959–1964.

[102] F. Xia et al. ‘Colorimetric detection of DNA, small molecules, proteins, and ions using unmodified gold nanoparticles and conjugated polyelectrolytes’. In: *Proceedings of the National Academy of Sciences* 107.24 (2010), pp. 10837–10841.

[103] M. Li, C. An, W. Pisula and K. Müllen. ‘Alignment of Organic Semiconductor Microstripes by Two-Phase Dip-Coating’. In: *Small* 10.10 (2014), pp. 1926–1931.

[104] S. Agarwal, P. Mishra, G. Shivange, N. Kodipelli, M. Moros, J. M. de la Fuente and R. Anindya. ‘Citrate-capped gold nanoparticles for the label-free detection of ubiquitin C-terminal hydrolase-1’. In: *Analyst* 140 (4 2015), pp. 1166–1173.

[105] B. J. Olivier and C. M. Sorensen. ‘Variable aggregation rates in colloidal gold: Kernel homogeneity dependence on aggregant concentration’. In: *Physical Review A* 41 (4 Feb. 1990), pp. 2093–2100.

[106] A. Buffet et al. ‘P03, the microfocus and nanofocus X-ray scattering (MiNaXS) beamline of the PETRA III storage ring: the microfocus endstation’. In: *Journal of Synchrotron Radiation* 19.4 (July 2012), pp. 647–653.

[107] Merck. *Labor-Tools*. Tech. rep. Merck KGaA.

[108] S. D. Perrault and W. C. W. Chan. ‘Synthesis and Surface Modification of Highly Monodispersed, Spherical Gold Nanoparticles of 50–200 nm’. In: *Journal of the American Chemical Society* 131.47 (2009), pp. 17042–17043.

[109] M. V. Petoukhov, D. Franke, A. V. Shkumatov, G. Tria, A. G. Kikhney, M. Gajda, C. Gorba, H. D. T. Mertens, P. V. Konarev and D. I. Svergun. ‘New developments in the *ATSAS* program package for small-angle scattering data analysis’. In: *Journal of Applied Crystallography* 45.2 (Apr. 2012), pp. 342–350.

[110] J. M. Zook, V. Rastogi, R. I. MacCuspie, A. M. Keene and J. Fagan. ‘Measuring Agglomerate Size Distribution and Dependence of Localized Surface Plasmon Resonance Absorbance on Gold Nanoparticle Agglomerate Size Using Analytical Ultracentrifugation’. In: *ACS Nano* 5.10 (2011), pp. 8070–8079.

[111] V. Amendola and M. Meneghetti. 'Size Evaluation of Gold Nanoparticles by UV–vis Spectroscopy'. In: *The Journal of Physical Chemistry C* 113.11 (2009), pp. 4277–4285.

[112] C. S. Weisbecker, M. V. Merritt and G. M. Whitesides. 'Molecular Self-Assembly of Aliphatic Thiols on Gold Colloids'. In: *Langmuir* 12.16 (1996), pp. 3763–3772.

[113] R. Homick and H. Sloan. *Gold reclamation process.* US Patent 3,957,505. May 1976.

[114] L. Sun, Z. Zhang, S. Wang, J. Zhang, H. Li, L. Ren, J. Weng and Q. Zhang. 'Effect of pH on the Interaction of Gold Nanoparticles with DNA and Application in the Detection of Human p53 Gene Mutation'. In: *Nanoscale Research Letters* 4.3 (Nov. 2008), pp. 216–220.

[115] S. Nishimura, N. Abrams, B. A. Lewis, L. I. Halaoui, T. E. Mallouk, K. D. Benkstein, J. van de Lagemaat and A. J. Frank. 'Standing Wave Enhancement of Red Absorbance and Photocurrent in Dye-Sensitized Titanium Dioxide Photoelectrodes Coupled to Photonic Crystals'. In: *Journal of the American Chemical Society* 125.20 (2003), pp. 6306–6310.

[116] H. Noh, S. F. Liew, V. Saranathan, S. G. J. Mochrie, R. O. Prum, E. R. Dufresne and H. Cao. 'How Noniridescent Colors Are Generated by Quasi-ordered Structures of Bird Feathers'. In: *Advanced Materials* 22.26-27 (2010), pp. 2871–2880.

[117] C. H. Lim, H. Kang and S.-H. Kim. 'Colloidal Assembly in Leidenfrost Drops for Noniridescent Structural Color Pigments'. In: *Langmuir* 30.28 (2014), pp. 8350–8356.

[118] H. Hiramatsu and F. E. Osterloh. 'A Simple Large-Scale Synthesis of Nearly Monodisperse Gold and Silver Nanoparticles with Adjustable Sizes and with Exchangeable Surfactants'. In: *Chemistry of Materials* 16.13 (2004), pp. 2509–2511.

[119] S. Förster, A. Timmann, M. Konrad, C. Schellbach, A. Meyer, S. S. Funari, P. Mulvaney and R. Knott. 'Scattering Curves of Ordered Mesoscopic Materials'. In: *The Journal of Physical Chemistry B* 109.4 (2005), pp. 1347–1360.

[120] P. Debye. 'Interferenz von Röntgenstrahlen und Wärmebewegung'. In: *Annalen der Physik* 348.1 (1913), pp. 49–92.

[121] I. Waller. 'Zur Frage der Einwirkung der Wärmebewegung auf die Interferenz von Röntgenstrahlen'. German. In: *Zeitschrift für Physik* 17.1 (1923), pp. 398–408.

[122] P. Scherrer. ‘Bestimmung der Größe und der inneren Struktur von Kolloidteilchen mittels Röntgenstrahlen’. In: *Göttinger Nachrichten* 2 (1918), p. 98.

[123] A. L. Patterson. ‘The Scherrer Formula for X-Ray Particle Size Determination’. In: *Physical Review* 56 (10 Nov. 1939), pp. 978–982.

[124] A. Guinier. *X-ray diffraction in crystals, imperfect crystals, and amorphous bodies*. W.H. Freeman, 1963.

[125] P. Ehrenfest. ‘On interference phenomena to be expected whem Röntgen rays pass through a di-atomic gas.’ In: *PROCEEDINGS OF THE KONINKLIJKE AKADEMIE VAN WETENSCHAPPEN TE AMSTERDAM* (1915).

[126] D. Pontoni, T. Narayanan, J.-M. Petit, G. Grübel and D. Beysens. ‘Microstructure and Dynamics near an Attractive Colloidal Glass Transition’. In: *Physical Review Letters* 90 (18 May 2003), p. 188301.

[127] P. N. Pusey, W. van Megen, P. Bartlett, B. J. Ackerson, J. G. Rarity and S. M. Underwood. ‘Structure of crystals of hard colloidal spheres’. In: *Physical Review Letters* 63 (25 Dec. 1989), pp. 2753–2756.

[128] K. W. Kratky. ‘Stability of fcc and hcp hard-sphere crystals’. In: *Chemical Physics* 57.1–2 (1981), pp. 167–174.

[129] P. G. Bolhuis, D. Frenkel, S.-C. Mau and D. A. Huse. ‘Entropy difference between crystal phases’. In: *Nature* 388.6639 (July 1997), pp. 235–236.

[130] H.-M. Lin and R. A. Nash. ‘An experimental method for determining the hildebrand solubility parameter of organic nonelectrolytes’. In: *Journal of Pharmaceutical Sciences* 82.10 (1993), pp. 1018–1026.

[131] P. Pusey. ‘The effect of polydispersity on the crystallization of hard spherical colloids’. In: *Journal de Physique* 48.5 (1987), pp. 709–712.

[132] R. P. Sear. ‘Phase separation and crystallisation of polydisperse hard spheres’. In: *Europhysics Letters* 44.4 (1998), p. 531.

[133] P. Sollich and N. B. Wilding. ‘Crystalline Phases of Polydisperse Spheres’. In: *Physical Review Letters* 104 (11 Mar. 2010), p. 118302.

[134] N. M. Dixit and C. F. Zukoski. ‘Competition between crystallization and gelation: A local description’. In: *Physical Review E* 67 (6 June 2003), p. 061501.

[135] A. Widmer-Cooper and P. Geissler. ‘Orientational Ordering of Passivating Ligands on CdS Nanorods in Solution Generates Strong Rod–Rod Interactions’. In: *Nano Letters* 14.1 (2014), pp. 57–65.

[136] W. D. Luedtke and U. Landman. ‘Structure and Thermodynamics of Self-Assembled Monolayers on Gold Nanocrystallites’. In: *The Journal of Physical Chemistry B* 102.34 (1998), pp. 6566–6572.

[137] X. Lin, C. Sorensen and K. Klabunde. ‘Digestive Ripening, Nanophase Segregation and Superlattice Formation in Gold Nanocrystal Colloids’. English. In: *Journal of Nanoparticle Research* 2.2 (2000), pp. 157–164.

[138] W. van Megen and P. N. Pusey. ‘Dynamic light-scattering study of the glass transition in a colloidal suspension’. In: *Physical Review A* 43 (10 May 1991), pp. 5429–5441.

[139] J. K. Percus and G. J. Yevick. ‘Analysis of Classical Statistical Mechanics by Means of Collective Coordinates’. In: *Physical Review* 110 (1 Apr. 1958), pp. 1–13.

[140] A. Vrij. ‘Mixtures of hard spheres in the Percus–Yevick approximation. Light scattering at finite angles’. In: *The Journal of Chemical Physics* 71.8 (1979), pp. 3267–3270.

[141] J.-P. Hansen and L. Verlet. ‘Phase Transitions of the Lennard-Jones System’. In: *Physical Review* 184 (1 Aug. 1969), pp. 151–161.

[142] G. P. Hoffmann and H. Löwen. ‘Freezing and melting criteria in non-equilibrium’. In: *Journal of Physics: Condensed Matter* 13.41 (2001), p. 9197.

[143] A. Checco, B. M. Ocko, A. Rahman, C. T. Black, M. Tasinkevych, A. Giacomello and S. Dietrich. ‘Collapse and Reversibility of the Superhydrophobic State on Nanotextured Surfaces’. In: *Physical Review Letters* 112 (21 May 2014), p. 216101.

[144] Y. Nakayama, P. J. Pauzauskie, A. Radenovic, R. M. Onorato, R. J. Saykally, J. Liphardt and P. Yang. ‘Tunable nanowire nonlinear optical probe’. In: *Nature* 447.7148 (June 2007), pp. 1098–1101.

[145] E. Theocharous et al. ‘The partial space qualification of a vertically aligned carbon nanotube coating on aluminium substrates for EO applications’. In: *Optics Express* 22.6 (Mar. 2014), pp. 7290–7307.

[146] W. Lu and C. M. Lieber. ‘Nanoelectronics from the bottom up’. In: *Nature Materials* 6.11 (Nov. 2007), pp. 841–850.

[147] C. W. Sele et al. ‘Controlled Deposition of Highly Ordered Soluble Acene Thin Films: Effect of Morphology and Crystal Orientation on Transistor Performance’. In: *Advanced Materials* 21.48 (2009), pp. 4926–4931.

[148] Y. Li, Y. Zhou, X. Meng, Y. Zhang, F. Song, S. Lu, H. Ren, P. Hu, Z. Liu and J. Zhang. ‘Gold nanoparticle aggregation-based colorimetric assay for β-casein detection in bovine milk samples’. In: *Food Chemistry* 162 (2014), pp. 22–26.

[149] S. Ye, A. R. Rathmell, Z. Chen, I. E. Stewart and B. J. Wiley. ‘Metal Nanowire Networks: The Next Generation of Transparent Conductors’. In: *Advanced Materials* 26.39 (2014), pp. 6670–6687.

[150] J.-Y. Lee, S. T. Connor, Y. Cui and P. Peumans. ‘Solution-Processed Metal Nanowire Mesh Transparent Electrodes’. In: *Nano Letters* 8.2 (2008), pp. 689–692.

[151] T. Minari, Y. Kanehara, C. Liu, K. Sakamoto, T. Yasuda, A. Yaguchi, S. Tsukada, K. Kashizaki and M. Kanehara. ‘Room-Temperature Printing of Organic Thin-Film Transistors with π-Junction Gold Nanoparticles’. In: *Advanced Functional Materials* 24.31 (2014), pp. 4886–4892.

[152] T. Ackermann, S. Sahakalkan, I. Kolaric, E. Westkämper and S. Roth. ‘Co-percolation of carbon nanotubes and silver nanowires at low area densities: Tuning the optoelectrical performance of transparent electrodes’. In: *physica status solidi (RRL) – Rapid Research Letters* 9.2 (2015), pp. 141–144.

[153] K. Ellmer. ‘Past achievements and future challenges in the development of optically transparent electrodes’. In: *Nature Photonics* 6.12 (Dec. 2012), pp. 809–817.

[154] P. Butler. ‘Shear induced structures and transformations in complex fluids’. In: *Current Opinion in Colloid & Interface Science* 4.3 (1999), pp. 214–221.

[155] S. C. Glotzer and M. J. Solomon. ‘Anisotropy of building blocks and their assembly into complex structures’. In: *Nature Materials* 6.7 (Aug. 2007), pp. 557–562.

[156] D. Baranov, A. Fiore, M. van Huis, C. Giannini, A. Falqui, U. Lafont, H. Zandbergen, M. Zanella, R. Cingolani and L. Manna. ‘Assembly of Colloidal Semiconductor Nanorods in Solution by Depletion Attraction’. In: *Nano Letters* 10.2 (2010), pp. 743–749.

[157] J. L. Baker, A. Widmer-Cooper, M. F. Toney, P. L. Geissler and A. P. Alivisatos. ‘Device-Scale Perpendicular Alignment of Colloidal Nanorods’. In: *Nano Letters* 10.1 (2010), pp. 195–201.

[158] A. Patti and M. Dijkstra. ‘Do Multilayer Crystals Nucleate in Suspensions of Colloidal Rods?’ In: *Physical Review Letters* 102 (12 Mar. 2009), p. 128301.

[159] D. K. Smith, B. Goodfellow, D.-M. Smilgies and B. A. Korgel. 'Self-Assembled Simple Hexagonal AB2 Binary Nanocrystal Superlattices: SEM, GISAXS, and Defects'. In: *Journal of the American Chemical Society* 131.9 (2009), pp. 3281–3290.

[160] P. G. de Gennes. *The Physics of Liquid Crystals.* Oxford University Press, 1974.

[161] R. Oldenbourg, X. Wen, R. B. Meyer and D. L. D. Caspar. 'Orientational Distribution Function in Nematic Tobacco-Mosaic-Virus Liquid Crystals Measured by X-Ray Diffraction'. In: *Physical Review Letters* 61 (16 Oct. 1988), p. 1851.

[162] H. Feng, Y. Yang, Y. You, G. Li, J. Guo, T. Yu, Z. Shen, T. Wu and B. Xing. 'Simple and rapid synthesis of ultrathin gold nanowires, their self-assembly and application in surface-enhanced Raman scattering'. In: *Chemical Communications* (15 2009), pp. 1984–1986.

[163] G. Fournet. 'Fonctions de Diffusion pour des Formes Geometriques'. In: *Bulletin de la Société Française de Minéralogie et de Crystallographie* 74 (1951), p. 39.

[164] I. Breßler, J. Kohlbrecher and A. F. Thünemann. *SASfit: A comprehensive tool for small-angle scattering data analysis.* arXiv:1506.02958 [physics.data-an]. June 2015.

[165] A. Loubat, M. Imperor-Clerc, B. Pansu, F. Meneau, B. Raquet, G. Viau and L.-M. Lacroix. 'Growth and Self-Assembly of Ultrathin Au Nanowires into Expanded Hexagonal Superlattice Studied by in Situ SAXS'. In: *Langmuir* 30.14 (2014), pp. 4005–4012.

[166] S. Ota, T. Li, Y. Li, Z. Ye, A. Labno, X. Yin, M.-R. Alam and X. Zhang. 'Brownian motion of tethered nanowires'. In: *Physical Review E* 89 (5 May 2014), p. 053010.

[167] S. Mourdikoudis and L. M. Liz-Marzán. 'Oleylamine in Nanoparticle Synthesis'. In: *Chemistry of Materials* 25.9 (2013), pp. 1465–1476.

[168] S. Krüger, H.-J. Mögel, M. Wahab and P. Schiller. 'Depletion Force between Anisometric Colloidal Particles'. In: *Langmuir* 27.2 (2011), pp. 646–650.

[169] L. Onsager. 'THE EFFECTS OF SHAPE ON THE INTERACTION OF COLLOIDAL PARTICLES'. In: *Annals of the New York Academy of Sciences* 51.4 (1949), pp. 627–659.

[170] N. F. Bouxsein, L. S. Hirst, Y. Li, C. R. Safinya, Z. Abu Samah, N. C. MacDonald and R. Pynn. 'Alignment of filamentous proteins and associated molecules through confinement in microchannels'. In: *Applied Physics Letters* 85.23 (2004), pp. 5775–5777.

[171] C. G. Lopez, T. Watanabe, A. Martel, L. Porcar and J. T. Cabral. ‘Microfluidic-SANS: flow processing of complex fluids’. In: *Scientific Reports* 5 (Jan. 2015).

[172] B. D. Leahy, D. L. Koch and I. Cohen. ‘The effect of shear flow on the rotational diffusion of a single axisymmetric particle’. In: *Journal of Fluid Mechanics* 772 (June 2015), pp. 42–79.

[173] J. K. G. Dhont and W. J. Briels. ‘Rod-Like Brownian Particles in Shear Flow: Sections 3.1 – 3.9’. In: *Soft Matter*. Wiley-VCH Verlag GmbH & Co. KGaA, 2007, pp. 147–216.

[174] A. Aucejo, M. C. Burguet, R. Munoz and J. L. Marques. ‘Densities, Viscosities, and Refractive Indices of Some n-Alkane Binary Liquid Systems at 298.15 K’. In: *Journal of Chemical & Engineering Data* 40.1 (1995), pp. 141–147.

[175] S. Karim, M. E. Toimil-Molares, A. G. Balogh, W. Ensinger, T. W. Cornelius, E. U. Khan and R. Neumann. ‘Morphological evolution of Au nanowires controlled by Rayleigh instability’. In: *Nanotechnology* 17.24 (2006), p. 5954.

[176] S. Bhattacharya, S. Narasimha, A. Roy and S. Banerjee. ‘Does Shining Light on Gold Colloids Influence Aggregation?’ In: *Scientific Reports* 4 (June 2014), pp. 5213–.

[177] M. Newville, T. Stensitzki, D. B. Allen and A. Ingargiola. *LMFIT: Non-Linear Least-Square Minimization and Curve-Fitting for Python*. Sept. 2014.

A. Determination of Particle Size

The radius r of the gold core of the spherical nanoparticles used in this research were determined by a Python script that implements a fully automatic fit to the form factor of polydisperse spheres with a Schulz-Zimm size distribution. For the Schulz-Zimm distribution $f_{\mathrm{SZ}}(r)$ with mean radius R and relative width σ, the integral for the scattering of polydisperse spherical particles with form factor $P(q)$ (see eq. (1.21))

$$I(q) = \int f_{\mathrm{SZ}}(r) P(q, r) \mathrm{d}r \tag{A.1}$$

has an analytical solution, available from [88]:

$$I(q) = N \cdot (R^6 \cdot \sigma^{12} \cdot G(q)), \tag{A.2}$$

where N is used as a scaling factor, R the mean of the radius distribution with relative width σ. With

$$\alpha = \frac{1}{\sigma^2 q R}, \tag{A.3}$$

$G(q)$ can be written as

$$\begin{aligned} G(q) =& \alpha^6 - \left(1 + \frac{4}{\alpha^2}\right)^{-\frac{1}{2\sigma^2}} \cdot \alpha^6 \cdot \cos\left(\frac{1}{\sigma^2} \arctan\left(\frac{2}{\alpha}\right)\right) \\ & + \frac{1+\sigma^2}{\sigma^4} \cdot \left[\alpha^4 + \left(1 + \frac{4}{\alpha^2}\right)^{-\frac{1+2\sigma^2}{2\sigma^2}} \cdot \alpha^4 \cdot \cos\left(\frac{1+2\sigma^2}{\sigma^2} \cdot \arctan\left(\frac{2}{\alpha}\right)\right)\right] \\ & - \frac{2}{\sigma^2} \cdot \left(\frac{\alpha^2+4}{\alpha^2}\right)^{-\frac{1+\sigma^2}{2\sigma^2}} \cdot \alpha^5 \cdot \sin\left(\frac{1+\sigma^2}{\sigma^2} \cdot \arctan\left(\frac{2}{\alpha}\right)\right). \end{aligned} \tag{A.4}$$

To determine the size distribution of dilute, well-dispersed spherical particles, their background-corrected SAXS patterns (see fig. A.1 for illustration) were fit with eq. (A.2) by an automatised script. A starting value R_{i} for the particle radius is guessed based on the q value at the first local minimum in the data,

$$R_{\mathrm{i}} = \frac{4.493}{q_{\mathrm{min}}}. \tag{A.5}$$

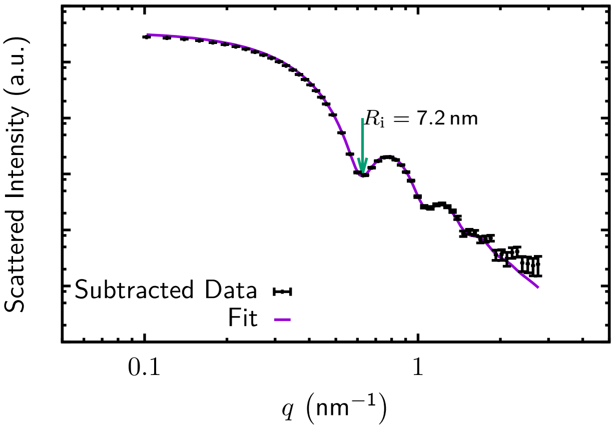

Figure A.1.: Illustration for the fitting algorithm.

With a guessed value of $\sigma_\mathrm{i} = 0.01$, the 6th data point (of a dataset ordered by ascending q-values) is taken as a reference to calculate the initial scaling factor N_i.

With fixed σ, optimum values for R and N were determined by least squares fitting of eq. (A.2) with the lmfit package [177] for Python. To finally refine the values for σ and R, the intensity between the first and third minimum was fitted with fixed N.

B. Additional Results for Unpolar Agglomeration

Additional results of the experiments presented in chapter 3 are presented in this chapter.

B.1. Agglomeration Induced by Ethanol

During two additional experiments, ethanol in different concentrations was used to destabilise Wu C12 particles. The temperature was set to 35 °C and the total flow rate to 5 µL s^{-1} (corresponding to approximated agglomerate ages of 3 min and 1.5 min for the SAXS and UV/Vis measurements respectively, according to fig. 3.2). The effective structure factors, including their fitted model functions, and the UV/Vis spectra of the agglomeration experiments (fig. B.1) confirmed the polarity-dependant agglomeration behaviour found for 1-propanol as agglomeration agent. The structure peaks at a smaller ethanol volume fraction of $\phi_{\mathrm{EtOH}} = 33\,\%$ were better defined compared to the peaks of the agglomerates grown with $\phi_{\mathrm{EtOH}} = 50\,\%$ (fig. B.1 (a)). The visual impression was confirmed by the fitted model function results. The domain size for smaller ethanol contents $D_{33} = 135\,\mathrm{nm}$ was found to be

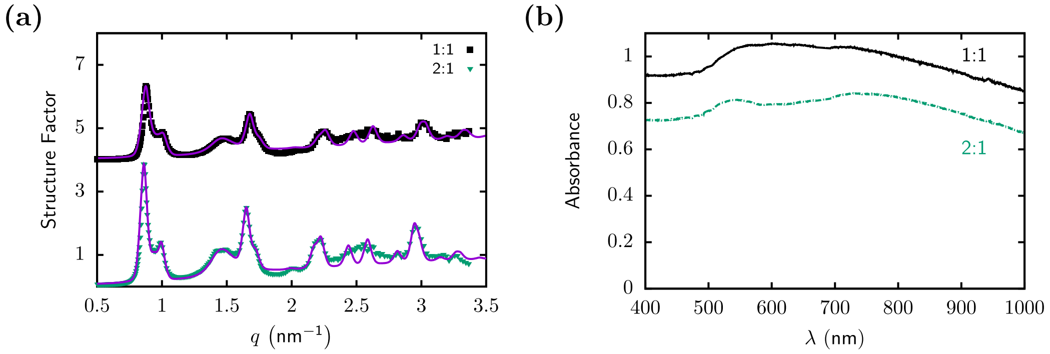

Figure B.1.: (a) Structure factors (black curve shifted up by +3) and (b) UV/Vis spectra for agglomerates grown at different solvent compositions (volume fractions of *n*-heptane:ethanol).

larger than for the higher ethanol content $D_{50} = 119\,\mathrm{nm}$. The normalised (111) to (311) peak height ratio points in the same direction: The value for 50 % ethanol, 1.2, was larger than the value for 33 %, 1.0. The surface gap of neighbouring particles in agglomerates at 33 % ethanol $d_\mathrm{s}^{33} = 2.8 \pm 0.4\,\mathrm{nm}$ was slightly larger compared to the value for 50 %, $d_\mathrm{s}^{50} = 2.6 \pm 0.4\,\mathrm{nm}$.

The UV/Vis spectra for both ethanol contents (fig. B.1 (b)) displayed a large redshifted portion compared to the primary particle spectra (fig. 3.6 (b)). The overall absorbance appeared larger for 50 % ethanol. The spectra for 33 % manifested a clear peak at the single particle peak position, whereas this peak appeared broadened for 50 %.

B.2. Agglomeration of Wu 2 Particles

A second batch of hexadecanethiol stabilised Wu particles, Wu 2, was prepared. The particles significantly differed in their average radius, $3.6 \pm 0.3\,\mathrm{nm}$, compared to the other Wu particles ($r = 3.0 \pm 0.2\,\mathrm{nm}$), and are therefore discussed in this separate section. Equal volumes of the dispersion and 1-propanol were mixed at a total flow speed of $5\,\mathrm{\mu L\,s^{-1}}$ at temperatures of 35 °C and 45 °C.

The structure factors at 45 °C (fig. B.2) displayed the structure peaks of a fcc superlattice. The cubic lattice parameter $a = 14.96\,\mathrm{nm}$, determined from the fit peak positions, was larger compared to the values of the smaller particles. Using the core size determined from the single particle measurements, the surface gap amounts to $d_\mathrm{s} = 2.5 \pm 0.6\,\mathrm{nm}$. The superlattice domain size $L = 107\,\mathrm{nm}$ was determined from the peak width of the fit.

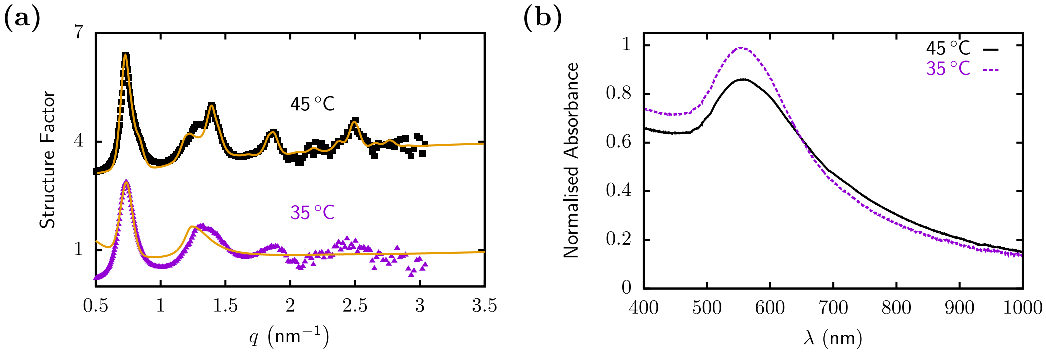

Figure B.2.: (a) Fits of the structure factors of agglomerating Wu 2 particles at 45 °C and 35 °C with the modified structure factor model (yellow lines) and the measured structure factors. The upper curve is offset by 3. (b) UV/Vis spectra corresponding to (a).

At 35 °C the structure factor mainly exhibited a single amorphous peak. Additional superlattice peaks can not be distinguished. The average surface gap between next neighbours, calculated via the Ehrenfest relation and subtraction of the core sizes, is 3.6 ± 0.6 nm.

The absorbance in the UV/Vis spectra at different temperatures is differently distributed. The spectrum of agglomerates at 45 °C shows a larger redshifted portion compared to the 35 °C measurement.

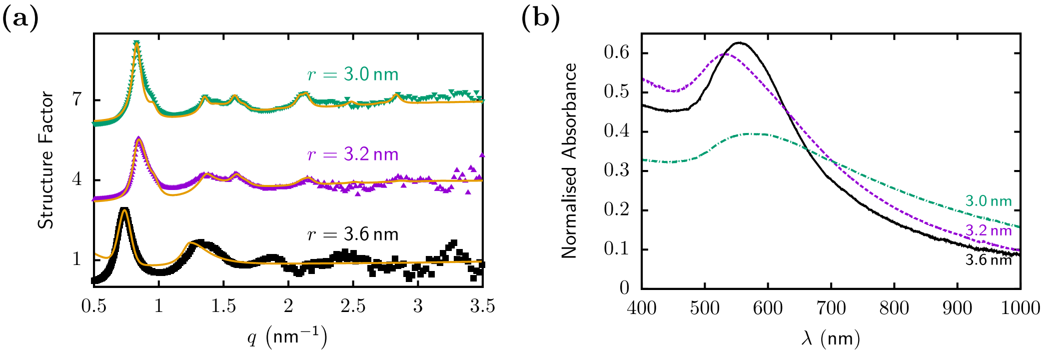

Figure B.3.: (a) SAXS (offset by 3) and (b) UV/Vis (normalised by the particle concentration of the dispersion) results for C16 stabilised Wu (3.0 nm), Zheng (3.2 nm) and Wu 2 (3.6 nm) agglomerates at 35 °C.

At otherwise equal conditions, the results for agglomerates of the different C16 stabilised particle batches clearly differed. The structure peaks were shifted to lower q values for increasing core sizes and appeared overall more pronounced for the smaller particles (fig. B.3 (a)). The redshifted part of the UV/Vis spectra increased with decreasing core radius (fig. B.3 (b)).